MOLECULAR SIMULATIONS OF BIOFUEL AND WATER PURIFICATION IN METAL–ORGANIC FRAMEWORKS

NALAPARAJU ANJAIAH

NATIONAL UNIVERSITY OF SINGAPORE

2012

MOLECULAR SIMULATIONS OF BIOFUEL AND WATER PURIFICATION IN METAL–ORGANIC FRAMEWORKS

NALAPARAJU ANJAIAH

(M.Tech., IIT Kanpur)

A THESIS SUBMITTED

FOR THE DEGREE OF DOCTOR OF PHILOSOPHY

DEPARTMENT OF CHEMICAL AND BIOMOLECULAR ENGINEERING

NATIONAL UNIVERSITY OF SINGAPORE

2012

Acknowledgements

This thesis would have not been possible without the steady support, impeccable guidance and encouragement from my supervisor, Prof. Jiang Jianwen. I have been fortunate to pursue my PhD under such splendid supervision. I owe my deepest gratitude to him for the patience and understanding showed to me throughout my PhD program. Under his supervision, I have learnt the true essence of being *"creative, proactive, persistent and skillful"* to tackle research problems. Undoubtedly, I treasure this experience in all my future endeavors.

I owe a significant debt to all present and former members of Prof. Jiang's research group for being there as a precious source to discuss technical aspects and also to have refreshing chitchats. I cherish all the priceless moments in the group meetings and activities. I wish to make special thanks to Dr. Hu Zhongqiao, Dr. Babarao Ravichandar and Ms. Chen Yifei for sharing their invaluable knowledge and also for providing timely helps on several occasions.

I am grateful to National University of Singapore for providing me the research scholarship to pursue doctoral study. I also express special thanks to all faculty and staff in the department (ChBE) for offering an enriching academic and social environment. I am thankful to the reviewers for spending time on evaluating my thesis.

I would like to express my deepest gratitude to many people who all together created a homely environment and made my stay in Singapore pleasant and memorable. I would like to particularly express my heartfelt gratitude to Sint for looking after me more than like a family member. I am very much indebted to her continuous support and encouragement. Without her help, it would have been difficult to overcome the tough

phases of my study and research. I would like to specially thank my flatmates for their help and understanding, particularly during difficult times.

I am deeply indebted to my parents and family members for their endless love and support. Their well wishes have always been a great strength to me at all stages of my life. To them I dedicate this thesis. Acknowledgements are also due to my friends and teachers in all stages of my academic life. In addition to those already mentioned, I am grateful to each and everyone who directly or indirectly helped me to complete this thesis.

Finally, I thank almighty God for giving me this opportunity and offering me enough strength to finish my PhD program.

Anjaiah Nalaparaju

Table of Contents

Acknowledgements i

Table of Contents iii

Summary vi

List of Tables ix

List of Figures x

Abbreviations xv

Chapter 1. Introduction 1

1.1 Metal–Organic Frameworks 1

1.1.1 Diversity in Design of MOFs 5

1.2 Multifunctional Properties of MOFs 9

1.2.1 Gas Storage 10

1.2.2 Gas/Vapor Separation 11

1.2.3 Liquid Separation 13

1.2.4 Ion Exchange 16

1.2.5 Catalysis 17

1.2.6 Water-Containing Systems 18

1.3 Literature Review 20

1.3.1 Studies beyond Gas Storage and Separation 21

1.3.2 Studies on Water-Containing Systems 22

1.4 Simulation Methodology 25

1.4.2 Monte Carlo 27

1.4.2 Molecular Dynamics 29

1.5 Scope of the Thesis 30

1.6 Organization of the Thesis 31

Chapter 2. Water in Ion-Exchanged Zeolite-like MOFs 32

2.1 Introduction 32
2.2 Models and Methods 35
2.3 Results and Discussion 40
2.3.1 Locations and Dynamics of Na^+ Ions 41
2.3.2 Adsorption of Water 42
2.3.3 Mobility of Water 49
2.3.4 Vibration of Water 51
2.4 Conclusions 53

Chapter 3. Water and Alcohols in Hydrophilic and Hydrophobic Zeolitic MOFs 55

3.1 Introduction 55
3.2 Models and Methods 58
3.3 Results and Discussion 62
3.3.1 Pure components in Na-*rho*-ZMOF 62
3.3.2 Binary mixtures in Na-*rho*-ZMOF 66
3.3.3 Pure components in ZIF-71 68
3.3.4 Binary mixtures in ZIF-71 71
3.4 Conclusions 73

Chapter 4. Biofuel Purification in MOFs 76

4.1 Introduction 76
4.2 Models and Methods 79
4.3 Results and Discussion 82
4.3.1 Adsorption in Na-*rho*-ZMOF 83
4.3.2 Adsorption in $Zn_4O(bdc)(bpz)_2$ 88
4.3.3 Diffusion in Na-*rho*-ZMOF 91
4.3.4 Diffusion in $Zn_4O(bdc)(bpz)_2$ 94
4.3.5 Permselectivity 96
4.4 Conclusions 98

Chapter 5. Water Purification in *rho* Zeolite-like MOF 99

5.1 Introduction 99

5.2 Simulation Models and Methods 101

5.3 Results and discussion 104

5.3.1 Ion exchange process 105

5.3.2 Ions in *rho*-ZMOF 109

5.4 Conclusions 113

Chapter 6. Conclusions and Future Work 115

6.1 Conclusions 115

6.2 Future Work 118

References 121

Publications 136

Presentations 137

Appendix 138

Summary

In the last decade, metal–organic frameworks (MOFs) have emerged as a versatile class of hybrid nanoporous materials. Compared with zeolites, an exceptional degree of design tunability can be achieved in MOFs by judicious selection of inorganic and organic components, or via post-synthetic modifications. The possibilities of using MOFs have been realized in most applications where zeolites have been employed; however, major progress is achieved only on gas storage and separation applications. Recently, attention is turning towards employing MOFs in liquid-phase separation such as biofuel and water purification. For the facile usage of MOFs in these applications, it is of central importance to understand the chemical stability and properties of MOFs in aqueous environment. While a number of studies have investigated the stability of MOFs under humid atmosphere, very little is known about how MOFs interact with water and perform in water-containing applications. The pathway from laboratory synthesis and testing to practical utilization of MOF materials is substantially challenging and requires fundamental understanding from the bottom up.

With ever-growing computational resources, molecular simulation has become an invaluable tool for materials characterization, screening and design. At a molecular level, simulation can provide microscopic insights from the bottom-up and establish structure-function relationships. In this thesis, the objectives are to investigate biofuel and water purification in chemically and thermally stable MOFs by molecular simulation. As an initial step, the microscopic properties of water and alcohols in MOFs are examined. The whole thesis primarily consists of four parts:

(1) The adsorption, mobility and vibration of water in ion-exchanged *rho* zeolite-like MOF (ZMOF) are investigated. Because of the high affinity for nonframework ions, water is strongly adsorbed in *rho*-ZMOF with a three-step adsorption mechanism. Upon water adsorption, Na^+ cations are redistributed among different favorable sites and the mobility of ions is promoted, which reveals the subtle interplay between water and nonframework ions. The adsorption capacity and isosteric heat decrease with increasing ionic radius, as attributed to the reduced electrostatic interaction and free volume. The mobility of water in *rho*-ZMOF increases at low pressures but decreases upon approaching saturation. The vibrational spectra of water in Na-*rho*-ZMOF exhibit distinct bands corresponding to the librational motion, bending, and stretching of adsorbed water molecules.

(2) The adsorption of water and alcohols (methanol and ethanol) is investigated in two MOFs topologically similar to *rho*-zeolite, one is hydrophilic Na^+-exchanged *rho* zeolite-like MOF (Na-*rho*-ZMOF) and the other is hydrophobic zeolitic-imidazolate framework-71 (ZIF-71). The adsorption isotherms in Na-*rho*-ZMOF are type I as a consequence of the high affinity of adsorbates with framework. In water/methanol and water/ethanol mixtures, water adsorption increases continuously with increasing pressure and replaces alcohols competitively at high pressures. In ZIF-71, the framework-adsorbate affinity is relatively weaker and type V adsorption is observed. In water/alcohol mixtures, alcohols are selectively more adsorbed at low pressures, but surpassed by water with increasing pressure. The framework charges have a substantial effect on adsorption in Na-*rho*-ZMOF, but not in ZIF-71.

(3) Biofuel (water/ethanol mixtures) purification is studied in two MOFs, hydrophilic Na-*rho*-ZMOF and hydrophobic $Zn_4O(bdc)(bpz)_2$ at both pervaporation (PV) and vapor permeation (VP) conditions. In Na-*rho*-ZMOF, water is preferentially adsorbed over ethanol and the diffusion selectivity of water/ethanol increases in Na-*rho*-ZMOF with increasing water composition. In contrast, ethanol is adsorbed more in $Zn_4O(bdc)(bpz)_2$ and the diffusion selectivity of ethanol/water decreases slightly in $Zn_4O(bdc)(bpz)_2$ with increasing water composition. The permselectivities in the two MOFs at both PV and VP conditions are largely determined by the adsorption selectivities. Na-*rho*-ZMOF is preferable to remove a small fraction of water from water/ethanol mixtures and enrich ethanol at the feed side and $Zn_4O(bdc)(bpz)_2$ is promising to extract a small fraction of ethanol and enrich ethanol at the permeate side.

(4) Removal of toxic Pb^{2+} ions from water for purification is investigated. In *rho* ZMOF with nonframework Na^+ ions, ion exchange between Na^+ and Pb^{2+} ions is observed from simulation. By umbrella sampling, the potential of mean force for Pb^{2+} is estimated to be $-10\ k_BT$, which is more favorable than $-5\ k_BT$ for Na^+ and contributes to the observed ion exchange. The residence-time distributions and mean-squared displacements reveal that all the exchanged Pb^{2+} ions stay exclusively in *rho*-ZMOF without exchanging with other ions in solution due to the strong interaction with *rho*-ZMOF; however, Na^+ ions have a shorter residence time and a larger mobility than Pb^{2+} ions.

List of Tables

Table 2.1	Potential parameters for water atoms (OW and HW), ions (Li^+, Na^+ and Cs^+) and framework atoms (In, N, O, C and H).	38
Table 3.1	Potential parameters of adsorbates (water, methanol and ethanol).	60
Table 5.1	Lennard-Jones parameters of framework atoms and heavy metal ions.	103

List of Figures

Figure 1.1 Synthesis of MOF-5 and Cu-BTC from molecular building blocks. 3

Figure 1.2 Application-oriented properties of MOFs with prototypical linkers. 10

Figure 1.3 Number of publications for MOFs (from the ISI web of science). 20

Figure 2.1 (a) Eight-coordinated molecular building block. (b) Atomic charges in a fragmental cluster of *rho*-ZMOF. Color code: In, cyan; N, blue; C, grey; O, red; and H, white. 36

Figure 2.2 Locations of Na^+ ions in Na-*rho*-ZMOF. Site I (green) is at the single eight-membered ring (S8MR), while site II (orange) is in the α-cage. (a) unit cell and (b) eight-membered ring and α-cage. Color code: In, cyan; N, blue; C, grey; O, red; and H, white. (c) Mean squared displacements of Na^+ ions. 41

Figure 2.3 Density contours of water in Na-*rho*-ZMOF at 10^{-8}, 10^{-2} and 1 kPa. Na^+ ions are represented by the large pink spheres. The density is based on the number of water molecules per $Å^3$. 43

Figure 2.4 Radial distribution functions of (a) Na_I^+-OW (b) Na_{II}^+-OW (c) OW-OW in Na-*rho*-ZMOF at 10^{-8}, 10^{-2}, 0.1 and 1 kPa. For comparison, $g(r)$ of OW-OW in bulk water is included as the dashed line in (c). 43

Figure 2.5 Coordination numbers of water around (a) Na_I^+ and (b) Na_{II}^+ in Na-*rho*-ZMOF at 10^{-8}, 10^{-2}, 0.1 and 1 kPa. 45

Figure 2.6 (a) Adsorption isotherms of water in Li-, Na- and Cs-exchanged *rho*-ZMOF as a function of pressure. The inset shows the numbers of Na_I^+ and Na_{II}^+ as function of water loading in Na-*rho*-ZMOF. (b) Adsorption isotherms of water in Li-, Na- and Cs-exchanged *rho*-ZMOF at low-pressure regime. 46

Figure 2.7 Calculated isosteric heats of water adsorption in Li-, Na- and Cs-exchanged *rho*-ZMOF as a function of loading. 47

Figure 2.8 Locations of water in the single 8-membered ring in Li-, Na- and Cs-exchanged *rho*-ZMOF at 10^{-8} kPa. Color code: In, cyan; N, blue; C, grey; O, red; H, white; Li^+, yellow; Na^+, green; and Cs^+, pink. The distances between water and ions are in Angstroms. 49

Figure 2.9 (a) Mean-squared displacements of water and (b) Na^+ ions in Na-*rho*-ZMOF at various pressures. 50

Figure 2.10 Vibrational spectra of water in Na-*rho*-ZMOF at various pressures and in bulk water. 51

Figure 3.1 Pore morphologies and radii in (a) Na-*rho*-ZMOF and (b) ZIF-71. Color code: In/Zn, cyan; N, blue; C, grey; O, red; Cl, green; and H, white; and Na^+, purple. 57

Figure 3.2 Unit cells of (a) *rho*-ZMOF and (b) ZIF-71. Color code: In/Zn, cyan; N, blue; C, grey; O, red; Cl, green; and H, white. The nonframework Na^+ ions in *rho*-ZMOF are not shown. 58

Figure 3.3 (a) four-coordinated molecular building block. (b) Atomic charges in the fragmental clusters ZIF-71. Color code: Zn, cyan; N, blue; C, grey; O, red; Cl, green; and H, white. 59

Figure 3.4 Zeolite-analogue representation of (a) Na-*rho*-ZMOF and (b) ZIF-71. Two types of binding sites exist for Na^+ ions in Na-*rho*-ZMOF, in which site I (pink) is at the single eight-membered ring (S8MR) and site II (yellow) is in the α-cage. The two S8MRs form a double eight-membered ring (D8MR). 60

Figure 3.5 Adsorption isotherms of water, methanol, and ethanol in Na-*rho*-ZMOF. The inset shows the isotherms in the linear scale of pressure. The saturation pressure is 3.1 kPa for water, 16.8 kPa for methanol, and 7.2 kPa for ethanol. 62

Figure 3.6 Radial distribution functions $g(r)$ of (a) Na^+-adsorbate (b) O_2-adsorbate (c) In-adsorbate for water, methanol, and ethanol in Na-*rho*-ZMOF at 10^{-4} kPa. O_2 is the carboxylic oxygen atom of the framework as shown in Figure 3.3. 63

Figure 3.7 Density contours of water, methanol, and ethanol in Na-*rho*-ZMOF at 10^{-4} kPa. The density is based on the number of molecules per $Å^3$. The large pink spheres indicate Na^+ ions. The dotted circles indicate the single-eight membered rings (S8MRs). 65

Figure 3.8 Adsorption isotherms for the equimolar mixtures of (a) water/methanol (b) water/ethanol in Na-*rho*-ZMOF. (c) Selectivities. 66

Figure 3.9 Radial distribution functions $g(r)$ of In-adsorbate for the equimolar mixtures of (a) water/methanol (b) water/ethanol in Na-*rho*-ZMOF at 10^{-4} kPa. 67

Figure 3.10 Adsorption (filled symbols) and desorption (open symbols) isotherms of water, methanol, and ethanol in ZIF-71 as a function of (a) pressure and (b) reduced pressure. The saturation pressure P^o is 3.1 kPa for water, 16.8 kPa for methanol, and 7.2 kPa for ethanol. 69

Figure 3.11 Density contours of methanol in ZIF-71 at 13, 14, and 15 kPa, respectively. 70

Figure 3.12 Radial distribution functions $g(r)$ of (a) Zn-water (b) Zn-methanol and (c) Zn-ethanol for water, methanol, and ethanol in ZIF-71. 70

Figure 3.13 Adsorption isotherms for the equimolar mixtures of (a) water/methanol (b) water/ethanol in ZIF-71. (c) Selectivities. 71

Figure 3.14 Radial distribution functions $g(r)$ of Zn-adsorbate for the equimolar mixtures of (a) water/methanol at 16 kPa (b) water/ethanol at 10 kPa in ZIF-71. 72

Figure 3.15 Adsorption isotherms for the equimolar mixture of water/ethanol in (a) Na-*rho*-ZMOF and (b) ZIF-71 with and without the framework charges. 73

Figure 4.1 Atomic structures of (a) Na-*rho*-ZMOF and (b) $Zn_4O(bdc)(bpz)_2$. Color code: In, cyan; N, blue; Zn, green; C, grey; O, red; H, white; Na^+ ions, orange. 79

Figure 4.2 (a) Atomic charges in the fragmental clusters of $Zn_4O(bdc)(bpz)_2$. (b) Adsorption isotherms of methanol in $Zn_4O(bdc)(bpz)_2$ at 298 K. The open diamonds are the simulation results of this work, and the filled diamonds are experimental data. 80

Figure 4.3 Adsorption selectivities for water/ethanol mixtures in Na-*rho*-ZMOF at PV and VP conditions. The insets are adsorption isotherms. 83

Figure 4.4 Density contours of water and ethanol for water/ethanol mixture (10:90) at PV condition in Na-*rho*-ZMOF. 84

Figure 4.5 Radial distribution functions of (a) Na^+-adsorbates, (b) O_2-adsorbates, and (c) In-adsorbates. (d) Coordination numbers of water and ethanol around Na^+ ions for water/ethanol mixture (10:90) at PV condition in Na-*rho*-ZMOF. 85

Figure 4.6 Radial distribution functions of (a) Na^+-OW (OH), (b) O_2-OW (OH), and (c) In-OW (OH) for water/ethanol mixture (10:90) at PV condition in Na-*rho*-ZMOF. OW and OH are the oxygen atoms in water and ethanol, respectively. 87

Figure 4.7 Radial distribution functions of (a) O_{water}-$H_{ethanol}$, O_{water}-H_{water} and $O_{ethanol}$-$H_{ethanol}$ for water/ethanol equimolar mixture at PV condition. (b) O_{water}-$H_{ethanol}$ at PV condition and (c) O_{water}-$H_{ethanol}$ at VP condition with various feed compositions in Na-*rho*-ZMOF. 88

Figure 4.8 Adsorption selectivities for ethanol/water mixtures in $Zn_4O(bdc)(bpz)_2$ at PV and VP conditions. The insets are adsorption isotherms. 89

Figure 4.9 Density contours of ethanol and water for ethanol/water mixture (10:90) at PV condition in $Zn_4O(bdc)(bpz)_2$ 89

Figure 4.10 Radial distribution functions of (a) Zn-adsorbates, (b) C_6-adsorbates, and (c) C_3-adsorbates for ethanol/water mixture (10:90) at PV condition in $Zn_4O(bdc)(bpz)_2$. 90

Figure 4.11 Radial distribution functions of (a) O_{water}-$H_{ethanol}$, O_{water}-H_{water} and $O_{ethanol}$-$H_{ethanol}$ for water/ethanol equimolar mixture at PV condition. (b) O_{water}-$H_{ethanol}$ at PV condition and (c) O_{water}-$H_{ethanol}$ at VP condition with various feed compositions in $Zn_4O(bdc)(bpz)_2$. 91

Figure 4.12 Mean-squared displacements for water/ethanol mixtures in Na-*rho*-ZMOF with various feed compositions. 92

Figure 4.13 Mean-squared displacements on the log-scale for water/ethanol mixtures in Na-*rho*-ZMOF with various feed compositions. 93

Figure 4.14 Diffusivities at (a) PV and (b) VP conditions. (c) Diffusion selectivities for water/ethanol mixtures in Na-*rho*-ZMOF. 94

Figure 4.15 Mean-squared displacements for ethanol/water mixtures in $Zn_4O(bdc)(bpz)_2$ with various feed compositions. 94

Figure 4.16 Mean-squared displacements on the log-scale for ethanol/water mixtures in $Zn_4O(bdc)(bpz)_2$ with various feed compositions. 95

Figure 4.17 Diffusivities at (a) PV and (b) VP conditions. (c) Diffusion selectivities for ethanol/water mixtures in $Zn_4O(bdc)(bpz)_2$. 96

Figure 4.18 Permselectivities for water/ethanol mixtures in Na-*rho*-ZMOF and $Zn_4O(bdc)(bpz)_2$. 97

Figure 5.1 Unit cell of *rho*-ZMOF (nonframework ions are not shown). The 8-membered ring (8MR), 6-membered ring (6MR) and 4-membered ring (4MR) are indicated. Color code: In, cyan; N, blue; C, grey; O, red; and H, white. 102

Figure 5.2 Snapshots of simulation system (a) $t = 0$ (b) $t = 0.2$ ns and (c) $t = 2$ ns. Color code: Pb^{2+}: orange; Cl^-: green; Na^+: blue. 105

Figure 5.3 Numbers of Na^+, Pb^{2+} and Cl^- ions in Na-*rho*-ZMOF as a function of simulation duration. 106

Figure 5.4 Density profiles of Na^+, Pb^{2+} and Cl^- ions at (a) $t = 0$ (b) $t = 0.2$ ns and (c) $t = 2$ ns. The dotted-dashed line indicates solution/*rho*-ZMOF interface. 107

Figure 5.5 Potentials of mean force (PMFs) for Na^+, Pb^{2+} and Cl^- ions moving from solution to *rho*-ZMOF. The dotted-dashed line indicates the solution/*rho*-ZMOF interface. 108

Figure 5.6 Radial distribution functions of Na^+ and Pb^{2+} ions around the framework atoms (a) In (b) O_1 and (c) O_2. The insets show the coordination numbers of ions around the framework atoms. 110

Figure 5.7 (a) Residence time distributions and (b) mean-squared displacements of Pb^{2+} and Na^+ ions in *rho*-ZMOF. 111

Figure 5.8 (a) Mean-squared displacements and (b) velocity autocorrelation functions of Pb^{2+} ions in *rho*-ZMOF framework. Pb^{2+} in 8MR: pink; Pb^{2+} in 6MR, brown; Pb^{2+} in 4MR, orange. 112

Abbreviations

MOFs	Metal–Organic Frameworks
MOF-*n*	Metal–Organic Framework (with *n* an integer assigned in roughly chronological order)
IRMOF	Isoreticular Metal–Organic Framework
MIL	Materials of Institut Lavoisier
PCN	Porous Coordination Network
UMCM	University of Michigan Crystalline Material
CUK	Cambridge University-KRICT
POST-1	Pohang University of Science and Technology-1
PIZA	Porphyrinic Illinois Zeolite Analogue
ISE	Institut Solare Energiesysteme
MFU	Metal-Organic Framework Ulm University
DUT	Dresden University of Technology
ZIF-*n*	Zeolitic Imidazolate Framework (with *n* an integer assigned in roughly chronological order)
ZMOFs	Zeolite-like Metal Organic Frameworks
soc	Square Octahedral
MFI	Mobil Five
BEA	Zeolite Beta
MOR	Mordenite
FAU	Faujasite
ETS-10	Engelhard TitanoSilicate-10
SBU	Secondary Building Unit
TBUs	Tetrahedral Building Units
BDC	Benzene Dicarboxylate
BTC	Benzene Tricarboxylate
ImDC	Imidazolate Dicarboxylate
BPZ	Bipyrazolate
PDA	Phenylenediacetate

PZDC	Pyrazinedicarboxylate
BPEE	Bispyridylethene
DOE	Department of Energy
MC	Monte Carlo
MD	Molecular Dynamics
MSD	Mean Squared Displacement
GCMC	Grand Canonical Monte Carlo
DFT	Density Functional Theory
B3LYP	Becke's three parameter, Lee, Yang and Parr
CVFF	Consistent Valence Fore Field
TIP3P/Fs	Flexible Three Point Transferable Interaction Potential
TraPPE	Transferrable Potentials for Phase Equlibria
FF	Force Field
UFF	Universal Force Field
LJ	Lennard-Jones
LB	Lorentz-Berthelot
ESP	ElectroStatic Potential
D8R	Double eight Ring
S8R	Single eight Ring
VP	Vapor Permeation
PV	Pervaporation

Chapter 1

Introduction

1.1 Metal-Organic Frameworks

Nanoporous materials are an intriguing family of solid-state matter. The structures of these materials constitute a solid skeleton, which is usually described in terms of building units formed by the assembly of atoms, ions, or molecules, and a porous space of nanoscale. The porous space can act as an excellent platform to carry out reactions and separations with high specificity in chemical, petrochemical and pharmaceutical industries.[1] Since the discovery by Cronstedt in 1756, zeolites have been dominating the realm of nanoporous materials due to their unique pores and structural stability.[2] The pore size distribution in zeolites is narrower compared with other porous materials such as activated carbon, silica gel and activated alumina. The frameworks of zeolites are purely inorganic and constructed by oxygen bridged tetrahedral units of silica and aluminum. Zeolites have been used as size- and shape-selective molecular sieves in catalysis, as well in chemical separation and ion exchange.[3] However, the applications of zeolites have been confined only to specific operations, largely due to the limitation in enlarging pore sizes and less possibility to tailor the functionality of pore walls.[4,5] For example, the small pore size of zeolites is usually underlined as a key limitation in the catalytic transformation of large molecules (e.g. polyaromatics and carbohydrates) and the incorporation of transition elements**.** To develop new nanoporous materials of zeotype, several approaches have been implemented, such as varying primary building units to octahedrals, isomorphous substitution of other metal atoms, varying anions from O^{2-},

using templates to generate larger rings and scale chemistry to change the size of building units. Several such strategies have been used to design new inorganic nanoporous materials with improved properties.[6] In addition, organic functionalized zeolites also have been developed by applying appropriate functional groups as pendants onto the pore surfaces and also by partially incorporating into zeolitic frameworks to achieve selective host-guest interactions and heterogeneous catalysis.[7]

In supramolecular chemistry, one objective is to design new porous materials with predesigned molecular units. Consequently, the shape, size and functionality of the pores become more tunable.[8] However, a major difficulty in synthesizing porous solids based on molecular units is the isotropic interactions among organic molecules that usually lead to the closest packings.[9] Moreover, the network constructed by directional interactions with intention to create large cavities tends to self-interpenetrate in the voids of initial host structure and finally results in a dense structure. In early 1990's, Robson and coworkers produced an expanded diamondiod network with a 10.5 Å pore through the deliberate connection of tetrahedral building units formed by Cu^{+} node and nitrogen-donor 4,4′,4″,4‴-tetracyanotetraphenylmethane.[10] No interpenetration occurred in this framework and guest anions were readily exchanged with other ions. Following this work, a vast array of structures have been reported based on neutral nitrogen-donor ligands, particularly by using 4,4′-bipyridine (BPY).[11] However, the structures based on metal-BPY have several shortcomings, e.g., inclusion of a counterion was necessary, interpenetration was common, and thermal stability was often low (below 250 ^{o}C), especially upon guest removal. Subsequently, the success in use of anionic, polydentate rigid carboxylate linkers such as benzene-1,3,5-tricarboxylate (BTC) and benzene-1,4-

dicarboxylate (BDC) opened the era of reticular synthesis.[12] The strength of these building units arises from the enhanced electrostatic attractions and the size of carboxylate functionality permits the chelation of metal cations to produce rigid, geometrically defined clusters, which are termed as secondary building units (SBU). The yielded neutral, non-interpenetrated networks maintain crystallinity during exchange or complete removal of guests and the decomposition temperatures are up to 500 ^{o}C. Figure 1.1 illustrate the synthesis of two earliest MOFs, namely MOF-5[13] and Cu-BTC.[14] MOF-5 is prototypical framework constructed by $Zn_4O(CO_2)_6$ clusters connected with BDC linkers. Cu-BTC is formed by bimetallic "paddle wheel" Cu^{2+} clusters connected in a trigonal fashion by BTC linkers.

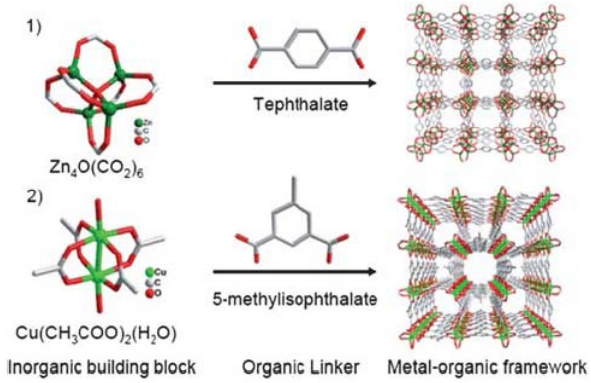

Figure 1.1. Synthesis of MOF-5 and Cu-BTC from molecular building blocks.[15] Reproduced with permission of the Royal Society of Chemistry (Appendix).

These robust MOFs are stable even after the removal and re-sorption of guest molecules, showing zeolites-like structures with permanent porosity. The access to this porosity is limited by the dimensions of pore windows rather than the cavities in the structures. Kitagawa and coworkers categorized them as the 2nd generation nanoporous materials.[16] In contrast, the 3rd generation MOFs have flexible and dynamic frameworks

that can respond to external stimuli such as light, electric field, gust molecules, and change pore size reversibly. As an early example, Kitagawa et al. reported a 3D crystalline pillared layer (CPL) $[Cu_2$(pyrazine-2,3-dicarboxylate)(1,2-dipyridylglycol).$8H_2O]_n$ (CPL-7), which shows a reversible crystal-to-crystal transformation on adsorption and desorption of H_2O or MeOH.[17] Upon dehydration, the 3D framework undergoes a pore contraction and the layer-layer distance drastically reduces to 9.6 Å from 13.2 Å. This drastic structural alternation influences sorption properties. As a consequence, N_2 and CH_4 cannot diffuse into the micropore of CPL-7, but H_2O and MeOH can diffuse albeit the pore size is smaller than MeOH molecule. Another example of dynamic MOF reported by Ferey et al. is MIL-53 (MIL = Materials of Institut Lavoisier). As a chromium dicarboxylate based MOF, MIL-53 exhibits a very large breathing upon hydration from MIL-53lt (lt = low temperature) to MIL-53ht (ht = high temperature). This phenomenon is not pronounced in vanadium based MIL-47, which is structural analogues to MIL-53.[18]

The salient strength of MOFs is not their thermal stability and in this aspect they cannot outperform than zeolites. Instead, the functionalization of organic linkers in MOFs or the direct incorporation of functional groups create unique porous solids that contain different groups capable of binding guests and/or catalyzing chemical reactions.[19] Especially by imparting chiral functionality and reactive groups, desired attributes can be obtained in a periodic manner throughout MOFs. Synthesis of chiral molecular sieves from polyhedral oxide is difficult, whereas homochiral MOFs are much straightforward to be produced by simply employing enantiomerically pure links. Kim et al. reported an enantiopure Zn-based framework POST-1, in which pyridinium functional groups are

protruded into the chiral channels.[20] These pyridine groups undergo exchange of protons with alkali metal ions or other ions. Attributed to the chiral environment, POST-1 can discriminate cationic enantiomers of $[Ru(2,2'\text{-bipy})_3]^{2+}$. They also found that immersion of L-POST-1 in a methanolic solution of racemic $[Ru(2,2'\text{-bipy})_3]^{2+}$ led to a change in crystal color from white to reddish yellow, and 80% of protons were exchanged by $[Ru(2,2'\text{-bipy})_3]^{2+}$.

1.1.1 Diversity in Design of MOFs

The field of MOFs has achieved an accelerated and sustained growth as reflected in two aspects: the new generation of ingenious topological structures and the potential applications in emerging areas.[21] Developments related to the former will be discussed below and the latter will be discussed in the next section.

Among a range of design principles, two approaches have been widely used to direct the synthesis of MOFs with desired topology and/or functionality. The first is 'node and spacer' approach, in which a net is usually constructed by metal-based node and organic spacer.[22] The node could be square, tetrahedral, octahedral, etc. The resultant network topology is dependent on the geometry and coordination environment of the node as the spacer is simply a linear connection between adjacent nodes. The second is reticular approach based on the secondary building unit (SBU) that is molecular polygon or polyhedron of metal cluster or molecular complex.[23] The network topology formed from this approach is mainly determined by the geometry of the pairing SBU. Although SBUs can be found in discrete molecules, only *in situ* formed SBUs have been exploited in the MOF synthesis. In each approach, the concept of using multitopic ligand of specific geometry to link metal ions or metal ion clusters with specific coordination preference is

common.[24] Using these approaches by deliberately choosing molecular building units, it is possible to explore the generation of three dimensional networks of varying known and unknown topologies.

In terms of the degree of chemical diversity compared with inorganic porous solids, MOFs allow a wider variety of coordination number ranging from 2 to 7 for transition metal ions and 7 to 10 for lanthanide ions. This feature, associated with the large choice of neutral and/or anionic functionalized organic linkers with possible chelation or single boding, provides a myriad of new MOFs.[16] An infinite number of materials can be designed by employing variations in both inorganic and organic building units. For example, inorganic building blocks in the SBU approach can be molecular triangle/triangular prism, square planar, octahedron, etc.; organic linkers may contain donors of O (polycarboxylates, polyphosponates) and N (imidazolates, polypyrazolates, polytetrazolates).[25] MOFs represent a breakthrough in materials chemistry since they combine all the desired possibilities occurring in other nanoporous solids with the tunability on all structural characteristics such as skeleton, surface and cage, thus leading to unlimited pore sizes and surface areas.[26,27] Similar to isomorphic substitution in zeolites, the principle of isoreticularity allows materials design with same geometry but varying functionality or changeable cavity size. Yaghi and coworkers demonstrated a beautiful example, in which a series of 16 isoreticular MOFs were produced by functionalizing the aromatic link of prototype MOF-5 with different organic linkers.[28] Using trigonal prismatic linkers to connect the same tetra zinc cluster, they further synthesized MOF-210 with the highest record surface area.[29] MOFs incorporate pores with crystallographically well-defined shapes including squared, rectangular and

triangular, in contrast to the spherical and slit-shaped pores usually observed in zeolites and activated carbons.[30] Several alternative names have been adopted for MOFs, such as porous coordination polymers, metal coordination polymer and porous coordination network. We use the name MOFs throughout this thesis to maintain consistency.

Over the past decade, there has been an explosive increase in the number of new MOFs reported.[31] Thousands of different MOFs with varying topologies have been deposited in CSD (Cambridge Structure Database). While some these structures were synthesized by rationally designed with predicted topology and properties, others were produced fortuitously or accidentally. In principle, if the nodes are well-defined, the network topology of resulting structure could be predicted.[32] For example, using the well-defined coordination geometries of metal centers as nodes, various minerals including quartz diamond, pervoskite, rutile, Pts, feldspar are produced by replacing O, S with polyatomic organic bridging ligands as linkers.[33,34] MOFs with topologies similar to inorganic zeolites exhibit unique properties, such as the presence of extra-large cavities (not present in zeolites), tunable organic functionality and ion-exchange capability. Zeolites consist of 4-connected tetrahedral building blocks, in which the T-O-T angle (T = metal atom) is around 145^{o}. The expansion and decoration of tetrahedral building blocks in zeolites can lead to highly porous MOFs with inorganic analogues structures.[35,36] In this regard, imidazolate has been used as a robust linker possessing an angle between the two nitrogen atoms analogous to the T-O-T angle in zeolites. In addition, imidazolate is mono-anionic and TX_2 (T = bivalent metal) can have a remarkable resemblance to SiO_2 units in zeolites.[37] In the synthesis of zeolites, structure directing agents (SDAs) play an important role and the structural diversity of zeolites is

in a large part due to the effect of various structure directing agents. Seminally, various possibilities have been exploited to incorporate structure directing effects on the generation of metal imidazolate with zeolitic topology. Tian et al. initiated the deliberate design of expanded tetrahedral building units based on imidazolate.[38] Such building blocks usually lead to diamond-like topology; however, by using piperazine as SDA they obtained an open cobalt imidazolate framework with topology analogous to pure silicate neutral framework. In a subsequent study, they reported the generation of zinc imidazolate frameworks with zeolitic topologies by using proper solvents as templates or as SDAs.[39] One of the structures possesses the GIS topology of natural zeolite. Chen and co-workers successfully synthesized three MOFs of zinc 2-alkylimidazolates with zeolitic SOD, ANA and RHO topologies by introducing methyl or/and ethyl groups substituent onto imidazolate, which acts as a template and SDA.[40] Meanwhile, Park et al. synthesized a series of ZIFs with several zeolitic topologies by properly controlling reaction conditions and exploiting amide solvent media and linker fictionalization as SDAs.[41] They also reported the first example of mixed-metal coordination net with zeolitic topology. Bu et al. used two complementary ligands to control framework topology in a cooperative manner with small ligand forming 4-rings and large ligand forming large rings such as 6- and 8-rings.[42] This study highlights the significance of framework building units to govern framework topology, in distinct contrast to inorganic analogues where SDAs primarily control topology. In all these approaches, the resultant frameworks are neutral and preclude the use of cationic SDAs, thus limiting structural diversity constructed from same metal ion and ligand. Eddaoudi et al. established a new strategy to develop zeolite-like MOFs. Specifically, an anionic framework is produced

from single metal ion based on molecular building blocks by judiciously selecting 6- or 8- coordinated metal and multi-valent, multifunctional ligand.[36] With this strategy, Liu et al. reported the first example of a 4-connected anionic MOF with *rho* topology.[43] It was synthesized by metal-ligand-directed assembly of In atoms and 4,5-imidazoledicarboxylic acid (H_3ImDC). In *rho*-ZMOF, each In atom is coordinated to four N and four O atoms of four separate doubly deprotonated H_3ImDC (HImDC), thus forming an eight-coordinated dodecahedron. Each independent HImDC is coordinated to two In atoms resulting in two rigid five-membered rings via N-, O-hetero-chelation. The structure of *rho*-ZMOF contains truncated cuboctahedra (α-cages) linked together through double eight-membered rings (D8MR). The substitution of oxygen in *rho*-zeolite with HImDCs generates a very open-framework with extra-large cavity of 18.2 Å in diameter. All these examples show the possibility of preparing open zeolitic structures based on metal imidazolates. Nevertheless, non-imidazolates can also be used to construct MOFs with zeolitic topology.[44,45]

While the design of new MOFs remains highly topical and several unprecedented network topologies are being discovered, the primary focus has shifted toward the development of new MOFs with multifunctional properties as discussed below.

1.2 Multifunctional Properties of MOFs

MOFs exhibit not only rich chemical diversity but also intriguing multifunctional properties in magnetism, conductivity and optical features.[46] These salient features lead to the new potential applications of MOFs as shown in Figure 1.2, which are far beyond traditional porous materials.[47] To date, MOFs have been largely investigated for gas

storage, chemicals separation, ion exchange and catalysis. Nevertheless, applications in other areas such as magnetic[48], electric[49] and optical properties[50] have been also explored.

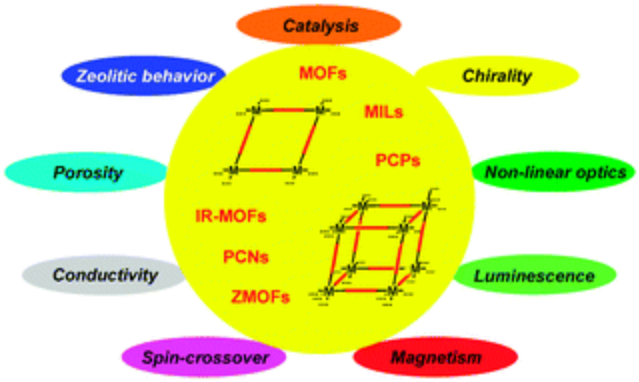

Figure 1.2. Application-oriented properties of MOFs with prototypical linkers.[47] Reproduced with permission of the Royal Society of Chemistry (RSC) for the Centre National de la Recherche Scientifique (CNRS) (Appendix).

1.2.1 Gas Storage

One of the most attractive functions of MOFs like other nanoporous solids is adsorption properties. Initial studies on adsorption of gases and vapors in MOFs were majorly carried out to examine the microporosity after complete evacuation of guest species. Kitagawa et al. first reported the adsorption of gases such as CH_4, N_2, and O_2 at 298 K and 1~36 atm in a 3D MOF formed by single metal ions bridged with 4,4′- bpy units.[51] Thereafter, Yaghi et al. reported the adsorption of CO_2 and N_2 in Zn(BDC).(DMF)(H_2O) at low-pressure range and determined the surface area and pore volume for the first time using Langmuir model.[52] Eddaoudi et al. performed a systematic study on adsorption of several gases and vapors in MOF-*n* (*n* =1-5).[53] Fletcher et al. reported the sorption measurements of vapors along with X-ray diffraction studies to examine host structural changes during adsorption in Ni_2(4,4′-bipyridine)$_3$(NO_3)$_4$.[54]

With the exceptionally high surface areas and low densities, porous MOFs stand out from other porous materials as good candidate for gas storage (e.g. H_2, CH_4 and CO_2). H_2 is a clean energy source and the major bottleneck for using H_2 fuel cell vehicles is the lack of a safe, efficient and economical on-board H_2 storage system. Since the first report of H_2 adsorption in MOFs by Yaghi and coworkers,[55] several MOFs have been evaluated as adsorbents for H_2 storage. In particular, PCN-12 shows the highest gravimetric uptake of H_2.[56] Although the Department of Energy (DOE) targets for H_2 storage are at near-ambient conditions, most studies have been based on 77 K and 1 atm which can be considered as benchmark state to compare H_2 adsorption capacities. CH_4 is another ideal energy source and the primary component of natural gas. Traditionally, CH_4 is stored by compressing at a high pressure of 200 atm. Carbon materials have been studied extensively for CH_4 storage, whereas MOFs are also tested. Kitagawa et al. first reported CH_4 uptake on a porous MOF.[51] PCN-14 was found to accommodate 230 v/v CH_4, which is 28% higher than DOE targets.[57] On the other hand, increasing concern on global warming has brought unprecedented attention to CO_2 capture by MOFs. From the seminal work of CO_2 adsorption in MOF-177, Yaghi and coworkers first reported that CO_2 uptake in MOFs could surpass the benchmark materials zeolite 13X and activated carbon MAXSORB by a factor of over 1.5 in both gravimetric and volumetric capacities.[58] A record capacity of 40 mmol/g has been achieved in MIL-101 for CO_2 adsorption, which is currently the highest among reported for MOFs.[59]

1.2.2 Gas/Vapor Separation

Many studies have explored the use of MOFs for the separation of industrially important gas mixtures (N_2/O_2, CO/H_2, CO_2/CH_4, CO_2/N_2 and CO_2/H_2). Wang et al.

investigated sorption behavior of several gases in Cu-BTC to analyze the separation performance.[60] Pan et al. reported the unprecedented selective sorption in a lanthanide-organic MOF. The dehydrated from of $[Er_2(pda)_3(OH_2)]$ adsorbs only CO_2 and almost no adsorption for Ar and N_2. The pore diameter is 3.4 Å and kinetic diameters of Ar, CO_2 and N_2 are 3.3 Å, 3.4 Å and 3.64 Å, respectively. N_2 is not adsorbed due to its large kinetic diameter; however, the large selectivity over Ar arises for CO_2 from the combined differentiations based on size and host-guest interactions.[61] A rigid porous MOF, manganese formate $Mn(HCOO)_2$, has unprecedented selectivity for H_2 over Ar and N_2 and also selective adsorption for CO_2.[62] Chen et al. exploited framework interpenetration to rationally design the pore size of MOFs to separate gas mixtures.[63] A chromatographic separation of $H_2/N_2/O_2/CH_4$ mixture was reported in CUK-1 on the basis of selective interaction.[64] Yang et al. reported selective gas adsorption in an interdigitated 3D MOF with 1D channels, and attributed the selectivity to the specific interactions between gas and framework surface.[65]

Kitaura et al. reported the selective adsorption of hydrogen-boding guests (e.g. MeOH and H_2O) against non hydrogen-bonding molecules (e.g. CH_4). Hysteresis was observed and attributed to the response of flexible framework to specific guest molecules and crystal to crystal transformation.[17] MOF-5 variant with high surface area MOCP was found to selectively adsorb *p*-xylene over *o*-xylene.[66] Maji et al. reported the selective adsorption of H_2O and MeOH over ethanol, THF and Me_2CO in [Cd(pzdc)(bpee)] due to size exclusion as a result of channel window of 3.5 Å × 4.5 Å.[67] Fletcher et al. reported the adsorption kinetics of MeOH and EtOH in MOFs prepared with MeOH and EtOH templates.[68] Takamizawa et al. reported EtOH adsorption in a MOF and elucidated the

formation of clusters/aggregates in the pore.[69] Favorable adsorption of H_2O over MeOH due to channel size was reported in a MOF with zeolitic topology.[70] Unprecedented selective adsorption of MeOH over H_2O in a MOF resulted from selective interaction with hydrophobic pore was observed by Pan et al.[71] Another hydrophobic MOF reported by Li and coworkers was found to be suitable for the separation of polar-nonpolar mixtures.[72] Later, Kitagawa and coworkers also reported several MOFs with hydrophobic surface showing type V adsorption for H_2O.[73,74] Zhang et al. reported an exceptionally flexible framework with hydrophobic channels, which selectively adsorb organic vapors over water.[75] Bourrelly et al. reported the adsorption behavior of polar vapors in flexible MIL-53 and found different structural transformations based on guest species.[76] MOFs with high adsorption capacity towards various organic solvents have been also investigated.[77,78] Achmann et al. identified that Fe-BTC material can be used as humidity sensor which has a more sensitive response for water over methanol and ethanol.[79] Yaghi and coworkers reported the high capacity and selective adsorption of harmful gases in various MOFs.[80] Lubbers et al. investigated the adsorption of 30 volatile organic compounds in IRMOF-1.[81] Separation of linear alkanes, alkane isomers, alkane/alkene have been also examined in MOFs based on various mechanisms, such as alkane mixtures with different sizes,[82] alkane isomers with different sizes and shapes,[83] paraffin/olefin mixtures with different π-π interactions[84] and xylene isomers with different packing efficiencies.[85,86]

1.2.3 Liquid Separation

As in gas phase, liquid separation is also important in chemical industry.[87] Yaghi et al. first observed the selective biding of MOFs for aromatic molecules such as benzene,

nitrobenzene over non-aromatic molecules. The remarkable selectivity towards aromatic molecules is a direct consequence of their π-stacking with the organic linkers in MOFs.[88] Thereafter, they further studied the selective binding of alcohols $C_{1-2} > C_3 > C_4 > C_5$ and C_7, which is in quantitative agreement with the expected trend based on size and shape. The absence of any competition from molecules without hydroxyl functionality reveals that the selectivity depends on not only shape and size, but electronic character.[89]

Much attention in the use of MOFs for liquid separation has been on the ability to separate chiral compounds. Kim and coworkers reported the separation of racemic mixture of $[Ru(2,2'\text{-bipy})_3]Cl_2$ in methanol by homochiral L-POST-1, which contains protonated pyridyl groups exposed in chiral channels.[20] Another hybrid MOF with zeolitic analogue composes of Cd^{2+} ions linked by quitenine was applied to the separation of racemic 2-butanol.[90] Suh and co-workers reported various MOFs that exhibited the selective binding of guest molecules based on host-guest interactions such as hydrogen bonding, hydrophobic and / or π-π interactions.[91,92] Takamizawa reported the selective inclusion of alcohols and the separation of alcohol/water mixture in MOF crystals dispersed in PDMS membrane. The separation factors were found to be 5.6 and 4.7 for methanol and ethanol, respectively, at room temperature in pervaporation conditions.[93] Based on the supramolecular assembly of carboxylate-substituted porphyrins with cobalt ions, microporous PIZA-1 was demonstrated as desiccant to dehydrate organic solvents such as benzene, toluene, and tetrahydrofuran. In comparison with zeolite 4A, PIZA-1 exhibits very good capacity and affinity for water over organic solvents. The size, shape and selectivity based on surface interactions were also investigate by studying the adsorption of various guests in MOFs.[94] A highly water selective MOF was reported

showing no adsorption for methanol, ethanol, acetonitrile or *n*-hexane under anhydrous conditions.[95] In addition, Bu et al. reported the adsorption of water over organic solvents[96] and Chen et al. reported the size based selection of water over methanol.[97] Denayer et al. investigated the separation of alkane mixtures and xylenes in HKUST-1[98], MIL-47[99] and MIL-53.[86] Adsorption of large organic dyes into MOF-177 from a solution was investigated to demonstrate the size selectivity in a regime previously not observed.[100] Another possible application of liquid adsorption in MOFs was shown by the use of a new copper MOF for the detection and adsorption of aromatic molecules in water.[101] Microwave-synthesized MIL-101 was employed for the removal of benzene from aqueous solution. Compared with activated carbon, MIL-101 adsorbs a larger amount of benzene. Additionally, the rate of benzene adsorption in MIL-101 is faster due to the large pore diameter.[102] This is an example where a MOF outperform activated carbon that is often used in industry and indicates that MOFs could be excellent alternatives to commonly used sorbents.

Not only can neutral molecules be separated using MOFs, but ions can also be removed from aqueous solutions. Mi et al. investigated the removal of heavy metal ions by adsorption onto the functional groups in porous metal sulfonate materials.[103,104] Wong et al. reported a luminescent porous framework comprised of terbium metal centers linked by mucic acid to separate I^-, Br^-, Cl^-, F^-, CN^-, and CO_3^{2-} from aqueous solutions. However, SO_4^{2-} and PO_4^{2-} were not adsorbed because they were too large to fit inside the framework pores.[105] Adsorption was attributed to the strong hydrogen bonding between anions and the OH groups of organic linkers. This example shows that size selective adsorption is possible for anions and that a MOF can be designed to enhance interactions

between anions and framework. Yet another important application in liquid adsorption is drug delivery. Ibuprofen was loaded into MIL-100 and MIL-101 from hexane solution. Due to the difference in pore sizes, the amount of IBU adsorbed in MIL-101 is 4 times higher than in MIL-100.[106]

1.2.4 Ion Exchange

Aluminum-substituted zeolites possess anionic frameworks, thus exhibit cation-exchange properties. However, MOFs may contain cationic, anionic or neutral frameworks, and have either anion- or cation-exchange properties. Anion exchange in MOFs was observed by Robson et al. in Cu^{I}[4,4′,4″,4‴-tetracyanotetraphenylmethane].[10] This MOF consists of very large admanantane-like cavities occupied by disordered nitrobenzene molecules together with BF_4^- ions, which could exchange with anions (e.g. PF_6^-). Later, Yaghi and coworkers reported anion exchange in a Cu-BPY connected MOF containing hydrated NO^{3-} ions. The loosely bound NO^{3-} ions are easily exchanged with hydrophobic BF_4^- or hydrophilic SO_4^{2-} ions in aqueous media.[107] In these two studies, no efforts were made to explain the mechanism for anion exchange and selectivity. Shu et al. reported a reversible anion exchange between Cl_4O^- and NO_3^- in porous MOFs formed by silver complexed with rigid tripodal nitrogen ligands. They found that anion exchange occurred by solid-state exchange mechanism rather than by solvent-mediated process; consequently, the exchange process was completely through the entire porous structure by the diffusion of ions in and out of the crystal, similar to ion exchange in resins and zeolites.[108] Wang et al. identified the selective anion exchange in a 3D-braided porous MOF containing two distinct types of channels with different sizes and shapes. In this

MOF, ClO_4^- ions exhibit selective exchange with PF_6^- anions over $CF_3SO_3^-$ due to the larger size of these triflate ions.[109]

In POST-1, cation exchange was observed with protons exchanged with Na^+, K^+ and Rb^+ from ethanol solution.[20] This structure also shows enantioselective cation exchange and inclusion of specific cation. In several studies, cation exchange was exploited to tune the capability of MOFs in various applications, e.g. cation exchanged *rho*-ZMOF in catalysis,[110] increasing H_2 uptake by varying cations,[111] tunable luminescent properties by cation exchange.[112] In addition to inorganic cations, organic cations have also been exchanged to tune MOF properties,[113] e.g., cation triggered drug release in bioMOF-1,[114] the effect of framework flexibility on ion exchange.[115]

1.2.5 Catalysis

MOFs also show a great potential in catalysis. The earliest example was a shape-specific catalytic activity observed in $[Cd(NO_3)_2(4,4'\text{-bpy})_2]_n$ with cadmium center acting as active Lewis acid site.[116] Similar type of Lewis acid catalyzed organic transformation also exists in MOFs with open metal sites such as Cu-BTC or MOF-199 and MIL-101.[117,118] Different from this, however, MIL-100 exhibits Bronsted-acid catalytic activity which catalyzes the Friedel-Crafts benzylation.[119] The catalytic activity of organic or pseudo-organic linkers were reported for Mn(III) and Zn(II) porphyrincarboxylate frameworks, which successfully catalyze the epoxidation of olefins and acyl transfer to pyridylcarbinols.[120,121] One of the interesting aspects of MOFs in catalysis is the catalytic sites can be modified according to the need of reaction by postsynthetic methods. For example, post-functionalized IRMOF-3 with vanadyl-salen catalytic site was used in the oxidation of cyclohexene.[122] During reaction, the reactive part may undergo a

geometrical rearrangement. This could lead to a structure collapse, deactivation of catalyst, and negative effects on activity, reproducibility and recycling. Therefore, there is a limitation on the design of active sites that also maintain the frameworks[123] Alternatively, MOFs can be used as support for active sites positioned within the pores by a non-covalent interaction. Due to the large pores available in MOFs, metal particles, complexes and clusters can be easily incorporated into the pores.

1.2.6 Water-Containing Systems

For successful implementation in liquid-phase applications, the thermal and chemical stability of MOFs are crucial. Compared with the strong covalent bonds in inorganic frameworks, MOFs are formed by metal-ligand coordination bonds or hydrogen bonds, thus result in less stable structures. Indeed, the thermal stability of MOFs is often limited below 400 °C and rarely above 500 °C. In terms of chemical stability, it is customary to know the structural integrity in the presence of water because water often exists during synthesis or application. Huang et al. initiated the experimental study on MOF stability.[66] It was found that MOF-5 analogue MOCP is not stable in water and acid medium, and one of the BDC ligand was replaced by water and the surface area and porosity decreased. Later, Panella et al. described the lowering of H_2 storage capacity in MOF-5 upon exposure to air.[124] Burrows et al. examined the effect of solvent hydrolysis on the synthesis of MOF-5.[125] Kaskel and coworkers found that Pd supported on MOF-5 has a higher catalytic activity for hydrogenation in comparison with Pd supported on activated carbon; however, a serious limitation of the Pd/MOF-5 catalyst was its instability in contact with water or humid air resulted from the low hydrothermal stability of MOF-5

support.[126] Kaye et al. proposed the conditions to synthesize and handle MOF-5 by examining the effect of exposure to atmospheric or water during sample preparation.[127]

A large number of MOFs are unstable in water or atmosphere, which impedes their applications. Kaskel et al.[128] and Low et al.[129] investigated the stability of several MOFs upon hydration. It was observed that MILs and ZIFs are stable and N-donor type MOFs are usually stable due to strong metal-ligand bonding. Many stable MOFs were reported with azole based linkers.[41,43] Post-synthetic modification by incorporating water repellent functional groups thus protecting the metal sites is another way to improve the moisture stability of MOFs.[130]

With the development of stable MOFs, the perspective of using MOFs expands to new applications. Janiak and coworkers employed ISE-1, a water stable MOF, as adsorbent for low-temperature heating and cooling.[131] Long and coworkers systematically investigated metal-azolate based stable MOFs for gas storage.[132,133] Tonigold et al. synthesized a stable cobalt-containing MOF (MFU-1) isostructural to MOF-5 and employed as catalyst in oxidation reactions.[134] Recently, Cychosz and Matzger used MIL-100 for the adsorption of pharmaceuticals and wastewater contaminants from aqueous solutions.[135] Ambiance of water influences both the stability and performance of MOFs. For example, the presence of water improves the selectivity for CO_2 over CH_4 in MIL-53.[136] For CO_2 adsorption in HKUST-1 and Ni/DOBDC, it was found that a small amount of water improves the adsorption in HKUST-1 but not in Ni/DOBDC.[137] In some situations, water might have a detrimental effect depending on the nature of water-MOF interaction.

A few studies have been reported to understand water adsorption in MOFs. For example, the adsorption of water vapor in MIL-53(Al) was investigated.[138] Kondo et al. examined water adsorption in water-resistant 3D pillared-layer MOFs with 1D semi-rectangular pores and found type-I adsorption isotherm.[139] Kaskel and coworkers studied water adsorption in several MOFs, namely, HKUST-1, ZIF-8, MIL-101, MIL-1009Fe) and DUT-4.[128]

1.3 Literature Review

Enormous studies have been reported on the synthesis, characterization and applications of MOFs. Figure 1.3 shows the number of publications for MOFs has increased rapidly in the recent years.

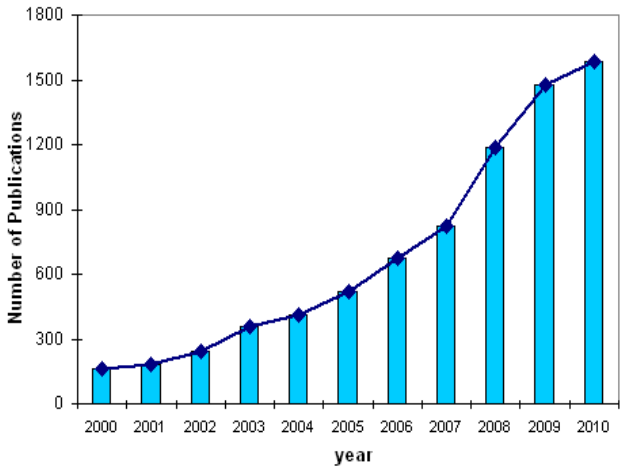

Figure 1.3. Number of publications for MOFs (from the ISI web of science).

As the number of MOFs synthesized to date is extremely large, experimentally testing and screening of ideal MOFs for a specific application is formidable and time-consuming. In this sense, molecular simulation has become an indispensible tool for materials characterization, screening and design. In this section, we briefly summarize simulation studies towards the development of MOFs in adsorption/separation

applications. Besides the separation of small gases mixtures (CO_2/N_2, CO_2/H_2, CO_2/CH_4, and O_2/N_2), MOFs have potential to be used in the separation of linear alkanes, alkane isomers, alkane/alkene, aromatics and also for removal/detection of harmful gases. Some representative examples are discussed first, followed by studies under ambient water.

1.3.1 Studies beyond Gas Storage and Separation

Düren and snurr investigated the separation of methane and *n*-butane mixtures in five IRMOFs with similar chemistry and topology but different pore sizes. They concluded that the selectivity for *n*-butane increases with decreasing cavity size and also with increasing the number of carbon atoms in organic linker.[140] Jiang and Sandler studied the separation of linear and branched alkanes in IRMOF-1. It was found that for a mixture of linear alkanes, energetic contribution is dominant at low fugacity thus long alkane was preferentially adsorbed, while short alkane replaces long alkane at high fugacity due to size entropy. For a mixture of linear and branched isomers, configurational entropy effect becomes more important, and linear isomer has a greater extent of adsorption.[141] Recently Jorge et al. reported the separation of propane and propylene in Cu-BTC. The main difference among the two adsorbates is the existence of a strong specific interaction between the π orbitals of propylene and the open metal sites of Cu-BTC.[142] Castillo et al. investigated the separation of xylene isomers in MIL-47. They found the order of preferential adsorption follows ortho > para > meta and the adsorption selectivity increases with pressure. The selective adsorption was attributed to the different packing efficiencies of xylene isomers.[143] Greathouse et al. studied the adsorption of complicated organic molecules relevant to chemical sensing and detection such as TNT, RDX and chemical warfare agents in IRMOFs, MIL-53 and Cu-BTC. They found π-π stacking

interactions are important contributors to the adsorption. MIL-53 shows the highest heat of adsorption thus it is suitable for detection of low-level organics.[144] Babarao and Jiang reported a computational study on the energetics and dynamics of IBU in two mesoporous MOFs, MIL-101 and UMCM-1.[145] They found that a coordination bond is formed between the carboxylic oxygen of IBU and the Cr site in MIL-101. However, no such bond is formed with UMCM-1 due to the absence of unsaturated metal sites. The mobility of IBU in MIL-101 is substantially smaller than UMCM-1. Snurr and coworkers reported the enantioselective separation of chiral hyrdrocarbons: (R,S)-1,3-dimethylallene, (R,S)-1,2-dimethylcyclobutane and (R,S)-1,2-dimethylcyclopropane in a homochiral MOFs consisting of cadmium centers and BINOL-type linkers.[146] They found that small zig-zag channels in the chiral MOFs largely contribute to most of the enantioselectivity, but the larger helical channels have an insignificant contribution.

1.3.2 Studies on Water-Containing Systems

Water is the most commonly encountering species in MOFs because of its presence as solvent molecule or as an inevitable component in practical applications. Some MOFs are not stable in water or tend to undergo structural transformation. Greathouse et al. reported the first molecular dynamics study to study the interaction of water with MOF-5. They used a hybrid force field by considering only nonbonded potential for Zn-O interactions and a modified CVFF force field for organic linkers. This force field was able to reproduce the experimentally measured lattice parameters of MOF-5. From the predicted lattice parameters at different water loadings, they found that MOF-5 is stable at a very low water content but unstable upon exposed to $\geq$ 4 wt% of water.[147] Later Schrock et al. used the same force field to examine the interfacial water in MOF-5, and

reported the instability of MOF-5 structure in presence of water based on the vibrational modes of hydrated structure.[148] Low et al. investigated the hydrothermal stability of a large series of MOFs. Using a cluster model, they estimated the energies of ligand displacement and hydrolysis for MOF-5, HKUST-1, MIL-101 and ZIF-8. By combining simulation with experiment, they reported a steam stability map and ZIF-8 was found to have the highest hydrothermal stability.[129] Recently, Han et al. applied a reactive force field to accurately simulate hydrolysis reaction and water stability in MOFs. Among MOF-5, IRMOF-10 and MOF-74, they found MOF-74 has a superior resistance to water than other MOFs.[149]

The presence of water in MOFs influences not only structure stability, but also separation performance. In hydrated MIL-101, the terminal water molecules on the open metal sites enhance the adsorption selectivity of CO_2/CH_4. The reason is the terminal water molecules act as additional adsorption sites and CO_2 interacts more strongly with them than CH_4.[150] A similar phenomenon is observed by Yazaydin et al. for the adsorption of CO_2/CH_4 and CO_2/N_2 mixtures in Cu-BTC with H_2O molecules coordinated to the exposed Cu atoms.[151] Thus, in addition to examine the stability of MOFs under humidity, it is also of primary importance to understand the interactions between water and MOFs for adsorption/separation applications. Castillo et al. simulated water adsorption in Cu-BTC and showed water has a large affinity for the open metal centers. The adsorption behavior is extremely sensitive to the partial charges of the Cu atoms.[152] Based on experimental adsorption isotherms and simulated adsorption enthalpies, Bourrelly et al. compared water adsorption with other polar molecules (methanol and ethanol) in flexible MIL-53. A significant contraction of the framework was found during

water adsorption, where the framework contracted and then expanded upon alcohol adsorption. The interaction energies calculated from DFT showed that ethanol has a stronger interaction with MIL-53 than water.[76] Recently, Paranthaman et al. simulated water adsorption in hydrophobic water-stable Al(OH)(1,4-naphthalenedicarboxylate) containing two types of channels. A type-V adsorption isotherm with a transition pressure around 1 kPa was observed due to the weak interaction between hydrophobic surface and water. At low pressures, water is adsorbed in the large channels; where at very high pressures ≥ 100 MPa, water is also adsorbed into the small channels.[153] Krishna et al. illustrated the effect of hydrogen boding on the adsorption and diffusion of water/alcohol mixtures in ZIF-8 and several zeolites.[154] Jiang and coworkers systematically studied the separation performance of gas mixtures in MOFs under the presence of small amount water. In ionic Na-*rho*-ZMOF, the presence of 0.1% water decreases the selectivity of CO_2/CH_4 by one order of magnitude. This suggests that the interaction between CO_2 and nonframework Na^+ ions is significantly reduced by water because water is a highly polar molecule and interacts with ions more strongly than CO_2.[155] Despite similar ionic framework, *soc*-MOF exhibits different behavior in which water promotes CO_2 adsorption at low pressures. This is because water interacts preferentially onto the metal sites rather than nonframework ions thus acts as additional adsorption site.[156] In a neutral framework $Zn(BDC)(TED)_{0.5,}$ water has no effect on the adsorption selectivity of CO_2/CH_4. This is attributed to the highly hydrophobic nature of this MOF.[157] Xiong et al. studied the adsorption and diffusion of RDX in IRMOF-1 in both dry and wet air conditions.[158]

In contrast to the large number of studies for gas-phase applications in MOFs, the simulation studies reported for liquid separation are scarce. This is primarily due to the significant amount of computational time required to simulate dense liquid phase. Consequently, the microscopic understanding of liquid phase separation is less complete. With increasing computational power, however, we expect more simulation studies will be reported in this area and a deeper molecular insight will be provided. Recently, Hu and Jiang investigated the desalination of NaCl solution through a ZIF-8 membrane.[159] Na^+ and Cl^- ions could not transport through the membrane and water desalination was observed because of the sieving effect of small apertures in ZIF-8.

1.4 Simulation Methodology

Molecular simulation has become as a robust tool to resolve many issues in science and engineering.[160] In particular, for the fundamental understanding of macroscopic physicochemical processes, simulation a molecular level is indispensible as experimental techniques may not provide microscopic information. In principle, the time-dependent Schrodinger's equation describes the underlying properties of molecular systems. However, its solution is very complex for systems larger than a few atoms. Therefore, classical simulation of complex systems in terms of atomic/molecular models has received a broader acceptance.[161] The advantage of molecular simulation is that it can not only calculate macroscopic properties but also provide microscopic details. Consequently, fundamental insights gained from molecular simulation can assist in the rational design of new materials and establish structure-function relationships to guide practical applications.

1.4.1 Force Field

The underlying information required in molecular simulation is intermolecular potentials, which exclusively determine the accuracy and reliability of simulation results. Intermolecular potentials are commonly referred as a force field consisting of a set of potential functions and parameters. In general the classical potential function consists bonded and nonbonded terms

$$u^{total} = u^{bonded} + u^{non-bonded} \tag{1.1}$$

where u^{bonded} is the intramolecular interaction consisting of

$$u^{bonded} = u^{stretching} + u^{bending} + u^{torsion} \tag{1.2}$$

The nonbonded interaction energy term $u^{non-bonded}$ includes

$$u^{non-bonded} = u^{VDW} + u^{Coulomb} \tag{1.3}$$

For very simple molecules (e.g. H_2, N_2, etc.), the force field can be derived based on quantum mechanics (QM) calculations. For large/complex molecules, however, force fields are commonly derived from experimental data, or sometimes combining with QM calculations. Over the years, several semi-empirical force fields have been developed with different analytical functional forms and a wide set of potential parameters. For example, class-I force fields (e.g. AMBER,[162] CHARMM,[163] GROMOS[164]) are mainly for condensed state properties, while class-II force fields (e.g. CVFF,[165] MM3[166] and UFF[167]) are focused on molecular structures and conformational equilibria. One of the criteria for a good force field is that it can be applied for a broad range of materials such as organic compounds, metals and transition metals. UFF is such a force field designed for simulating molecules containing any combination of elements.[167]

The extrapolation of molecular level information to macroscopic properties is attained through average over representative statistical ensembles. Macroscopic physical properties can be either static equilibrium properties such as potential energy and radial distribution function, or non-equilibrium properties such as viscosity and diffusion. To generate statistical ensembles, two simulation methods are available, namely Monte Carlo (MC) and molecular dynamics (MD).

1.4.2 Monte Carlo

MC simulation is a stochastic method that consists of a set of Markov trial moves to generate representative configurations. In general, MC simulation starts from an initial configuration of a system, then a trial move is attempted to change the configuration.[168] Based on the acceptance criteria, the move is accepted or rejected in such a way that the configurations are sampled from an appropriate ensemble distribution. A simple acceptance criterion was proposed by Metropolis as[169]

$$P_{acc}(o \to n) = \min\left(1, \exp\left\{-\beta\left[U(n) - U(o)\right]\right\}\right) \tag{1.4}$$

where β is the inverse temperature $1/k_B T$, k_B is Boltzmann's constant. U is the potential energy, and 'o' refers to an old state and 'n' refers to a new state. During each trial move, a pseudorandom number with value between 0 and 1 is generated. If this number is less than $P_{acc}(o \to n)$, then the trial move is accepted.

One attractive aspect of MC simulation is that only energies rather than forces are evaluated during configurational sampling. MC simulation can be performed with physically unnatural moves such as jump from one position to the other or random

insertion/deletion, and thus significantly increasing efficiency. MC simulation can be conducted in different ensembles, e.g. canonical ensemble and grand canonical ensemble.

Canonical Monte Carlo

In a canonical ensemble, temperature, volume and number of molecules are fixed. For MC simulation in a canonical ensemble, sample distribution is performed according to the Metropolis scheme. Three types of trial moves, namely translation, rotation and regrowth are commonly performed. The algorithm generates random trial moves from an old state (o) to a new state (n). If $P_B(o)$ and $P_B(n)$ denote the probability in the state (o) and (n), respectively, and $\alpha(o \to n)$ and $\alpha(n \to o)$ denote the conditional probability to perform a trial move from $(o \to n)$ and $(n \to o)$, respectively, then the probability $P_{acc}(o \to n)$ is related to $P_{acc}(n \to o)$ by

$$P_B(o)\alpha(o \to n)P_{acc}(o \to n) = P_B(n)\alpha(n \to o)P_{acc}(n \to o) \tag{1.5}$$

The probability of generating a particular configuration is constant and independent of the conformation

$$\alpha(o \to n) = \alpha(n \to o) = \alpha \tag{1.6}$$

By introducing this condition in the detailed balance, the acceptance rule becomes

$$P_{acc}(o \to n) = \min\left[1, \frac{P_B(n)}{P_B(o)}\right] \tag{1.7}$$

Grand Canonical Monte Carlo

In a grand canonical ensemble, temperature, volume and chemical potential are fixed. Consequently, the number of molecules is allowed to fluctuate. In addition to the trial moves commonly used in canonical MC simulation, molecules can be inserted or deleted in grand canonical MC (GCMC) simulation. In the insertion move, a new molecule is

inserted into the system at a randomly chosen position. The new configuration is accepted with a probability

$$P_{acc}(N \to N+1) = \min\left[1, \frac{fV\beta}{(N+1)} \exp\left\{-\beta\left[U(N+1) - U(N)\right]\right\}\right] \tag{1.8}$$

where f is the gas fugacity, V is the volume of the simulation box, N is the number of molecules present before the attempted insertion. In the deletion move, a molecule is randomly chosen to be deleted with a probability

$$P_{acc}(N \to N-1) = \min\left[1, \frac{N}{fV\beta} \exp\left\{-\beta\left[U(N-1) - U(N)\right]\right\}\right] \tag{1.9}$$

In a typical GCMC, the insertion is attempted throughout the entire volume of simulation box. Nevertheless, part of the volume is already occupied and inaccessible to the inserted molecule. Therefore, it is preferentially to find a region that is energetically favorable for the insertion with enhanced acceptance rate. In this case, the acceptance rules for insertion and deletion must be altered to ensure microscopic reversibility.

1.4.2 Molecular Dynamics

MD simulation mimics the natural pathway of motion to sample successive configurations. The Newton's second law of motion for a system of N interacting particles gives

$$F_i = m_i a_i \qquad (i = 1 \ldots N) \tag{1.10}$$

where F_i is the force acting on particle i, m_i and a_i are the particle's mass and acceleration, respectively. Since we are interested in the time evolution of the particle, Eq. (1.11) can be expressed in terms of displacement r with respect to time t.

$$\frac{\mathrm{F_i}}{m_i} = \frac{d^2 r_i}{dt^2} \tag{1.11}$$

The trajectory of the system can be obtained by solving Eq. (1.12). To integrate Eq. (1.12), several finite-difference schemes are available. In particular, the Verlet algorithm is probably the most widely used scheme. The basic equation in the Verlet algorithm is

$$\mathrm{r}(t + \Delta t) = \mathrm{r}(t) + \mathrm{v}(t)\Delta t + \mathrm{a}(t)\Delta^2 t \tag{1.12}$$

The time step Δt is chosen such a way that the integration is accurate and the total energy of the system is conserved. The average properties of the system can be determined from the trajectory obtained over a sufficiently long period of time.

1.5 Scope of the Thesis

Emerged as an intriguing class of nanoporous materials, MOFs have been considered versatile candidates for widespread applications in chemical industry. However, the pathway from laboratory synthesis and testing to practical utilization of MOF materials is substantially challenging and requires fundamental understanding. With ever-growing computational resources, molecular simulation has become an invaluable tool for materials characterization, screening and design. At a molecular level, simulation can provide microscopic insights from the bottom-up and establish structure-function relationships.

Currently, gas storage and separation in MOFs have received much attention and numerous simulation studies have been reported. Nevertheless, the knowledge pertaining to other important applications such as liquid separation is very limited. In this thesis, we aim to unravel from simulation the microscopic properties of water, alcohols and their mixtures in MOFs relevant to liquid-phase applications. The scope includes:

- To study the adsorption, mobility, and vibration of water in ion-exchanged zeolite-like MOFs
- To understand the adsorption of water and alcohols in hydrophilic and hydrophobic zeolitic MOFs
- To investigate the separation of water/ethanol mixtures by pervaporation and vapor permeation in MOFs for biofuel purification
- To investigate ion exchange in *rho* zeolite-like MOF for water purification

1.6 Organization of the Thesis

This thesis is organized into six chapters. In Chapter 1, the special features of MOFs along with interesting properties related to applications are discussed. A literature review highlighting adsorption and separation in MOFs is included. In addition, a brief introduction about simulation techniques employed in the thesis is described. In Chapters 2 to 5, simulation results pertaining to the objectives mentioned above are discussed. More specifically, Chapter 2 describes the adsorption, mobility, and vibration of water in ion-exchanged zeolite-like MOFs. Molecular understanding for the adsorption of water and alcohols in hydrophilic and hydrophobic zeolitic MOFs is discussed in Chapter 3. Chapter 4 addresses the biofuel purification by pervaporation and vapor permeation in MOFs. In Chapter 5, ion exchange in *rho* zeolite-like MOF is explored for water purification. Finally, key conclusions from the thesis and suggestions for future work are presented in Chapter 6.

Chapter 2

Water in Ion-Exchanged Zeolite-like MOFs

2.1 Introduction

Water exists ubiquitously in many natural and synthesized nanoporous materials such as zeolites, clays, and proteins.[170,171] As attributed to the surface interactions and geometry constrains, water in nanoconfined space behaves significantly different from bulk phase. For instance, unique two-dimensional layers, cyclic pentamers, infinite chains, and helical heptamers were observed for water upon confinement in various nanoporous materials.[172-175] The chemical composition of materials, charged species and hydration level all come into play in a complicated way and govern the microscopic properties of water. Therefore, an atomic-level understanding of water in nanoporous materials is fundamentally important for tuning material structures, functionalities, and applications.

A large number of experimental and simulation studies have been reported for water in a variety of nanoporous materials such as carbons, zeolites, and protein crystals. Gubbins and coworkers examined the structure and melting of water in carbon nanotubes and silica glasses, and found that the melting point was depressed relative to bulk water.[176,177] Murad and coworkers suggested that carbon nanotubes could be used for the separation of water and ions from salt solutions.[178,179] Do and coworkers simulated the effects of curvature and surface heterogeneity on water adsorption in finite-length carbon nanopores, and proposed a new adsorption-desorption model for water in activated carbon.[180,181] Sholl and coworkers examined the transport properties of hydrogen-bonding

liquids (water and alcohols) in single-walled metal-oxide nanotubes, and concluded that the hydrogen-bond network of water causes diffusion behavior different from alcohols.[182] Beauvais *et al.* quantitatively showed the redistribution of nonframework ions in FAU-zeolite during water adsorption, as well as the influence of hydration on separation of *p*- and *m*-xylene.[183] Di Lella *et al.* studied the effect of preadsorbed water on cation rearrangement and adsorption of hydrocarbon mixtures in zeolites.[184] Demontis *et al.* provided an atomic-scale description on nano-clustered water, along with the intra and intermolecular vibrational properties of water in zeolites.[185] Nalaparaju *et al.* simulated the adsorption and diffusion of water in Na-exchanged ETS-10 and observed a redistribution of Na^+ ions upon water adsorption.[186] Hu and Jiang investigated the spatial and temporal properties of water in bio-zeolites – protein crystals with different morphologies and chemical topologies, and found that the flexibility of protein framework promotes water mobility.[187,188]

In the past decade, there has been explosive interest in the potential applications of MOFs for gas storage and separation, catalysis, ion exchange, etc.[21,28,31,189,190] MOFs possess well-defined pores with record-breaking surface areas and pore volumes. In a large number of MOFs, water exists in the samples after synthesis. Some MOFs preferably allow the inclusion of water rather than other guest solvents.[95] It was observed that Zn- or Cu-based MOFs are sensitive to moisture and could degrade upon exposure to air.[66] As a consequence, water plays a crucial role in governing their structures and properties. From a MD simulation study, Greathouse and Allendorf found that MOF-5 is stable at very low water content but dissociates upon exposure to ≥ 4% water. They attributed the dissociation of MOF-5 to weak metal-linker interactions.[147] Kanoh and

coworkers experimentally determined water adsorption in pillared-layer MOFs with one-dimensional semi-rectangular pores and observed type-I isotherms.[139] Henninger *et al.* demonstrated that dehydratable-hydratable water stable MOF could be used for low-temperature heating and cooling.[131] Castillo *et al.* performed simulation to understand water adsorption in Cu-BTC and showed that water has a larger affinity for metal sites than light gases and hydrocarbons.[191] Küsgens *et al.* measured water adsorption in Cu-BTC, ZIF-8, MIL-101, DUT-4; and estimated the hydrophobicity and stability of MOFs toward moisture.[128]

Recently, Eddaoudi and coworkers developed a unique subset of MOFs, zeolite-like MOFs (ZMOFs), by utilizing metal-centers as nodes and polyatomic organic-ligands as linkers.[43,192,193] ZMOFs are topologically relevant to inorganic zeolites and exhibit similar structural properties. However, the substitution of oxygen atoms in zeolites with tunable organic linkers leads to extra-large pores. The edge expansion offers a great potential toward the design and synthesis of very open ZMOFs. Particularly interesting, a number of ZMOFs consist of ionic frameworks with charge-balancing nonframework ions, e.g., *rho*-ZMOF synthesized by assembly of tetrahedral building units with a long ditopic organic linker.[43] The presence of nonframework ions in charged ZMOFs offers several advantages over neutral structures in many industrial applications. Similar to highly stable zeolites, most ZMOFs largely maintain their structural integrity in water and organic solvents. From a practical point of view, ZMOFs could be potentially used in aqueous media for pervaporation, water treatment, and ion exchange. Therefore, a clear fundamental understanding on the microscopic properties of water in ZMOFs will be a

major step forward for their emerging applications. However, currently there is no study reported for water in ZMOF.

In this work, we investigate the adsorption, mobility, and vibration of water in ion-exchanged *rho*-ZMOF. First, the locations and dynamics of Na^+ cations in dry Na-*rho*-ZMOF are discussed; then the adsorption sites, isotherms and isosteric heats of water are presented; the effect of ion type on water adsorption is also explored. Finally, the mobility and vibration properties of water are reported.

2.2 Models and Methods

As the first example of a 4-connected MOF based on the topology of *rho*-zeolite, *rho*-ZMOF possesses a space group of *Im-3m* and a lattice constant of 31.062 Å. It was synthesized by metal-ligand-directed assembly of In atoms and 4,5-imidazoledicarboxylic acid (H_3ImDC).[43] Each In atom is coordinated to four N atoms and four O atoms of four separate doubly deprotonated H_3ImDC (HImDC) ligands, respectively, to form an eight-coordinated molecular building block as shown in Figure 2.1a. Each HImDC is coordinated to two In atoms by forming two rigid five-member rings via N-, O-hetero-chelation. The *rho*-ZMOF has a truncated cuboctahedron (α-cage) containing 48 In atoms, which link together through double eight-member rings (D8MR). The substitution of oxygen in *rho* zeolite with HImDC generates a very open-framework with extra-large cavity of 18.2 Å in diameter. Unlike *rho*-zeolite and other *rho*-aluminosilicate or aluminophosphate, *rho*-ZMOF contains twice as many positive charges (48 vs. 24) in a unit cell to neutralize the anionic framework. On the basis of the charge density (number of charges per cubic nanometer), however, *rho*-zeolite may contain higher charge density than *rho*-ZMOF. The as-synthesized negatively charged

rho-ZMOF contains charge-balancing doubly protonated 1,3,4,6,7,8-hexahydro-2H-pyrimido[1,2-a]pyrimidine (HPP). The HPP organic cations in the parent framework are fully exchangeable with other organic and inorganic cations. For instance, Na-exchanged *rho*-ZMOF with structural formula $[In_{48}(C_5N_2O_4H_2)_{96}][Na^+_{48}(H_2O)_{282}]$ was obtained by replacing HPP cations with Na^+ ions. Experimental thermogravimetric analysis showed that all residential water molecules in Na-*rho*-ZMOF can be completely evacuated.[43]

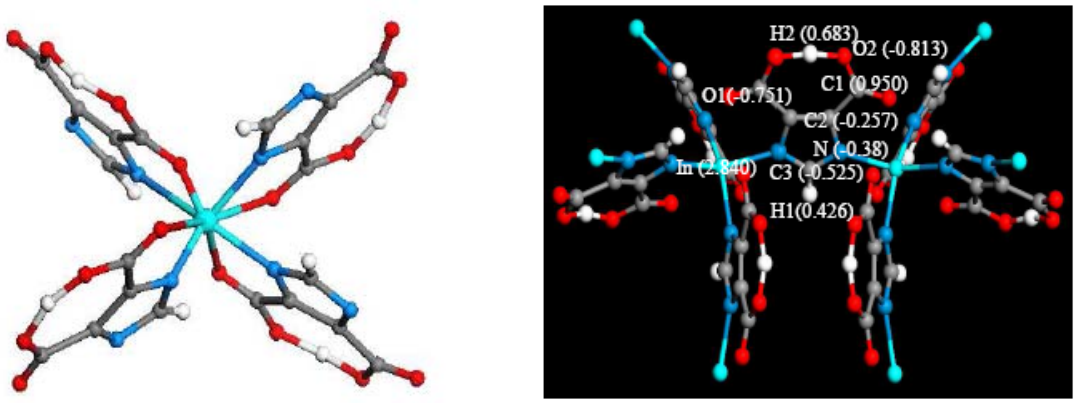

Figure 2.1. (a) Eight-coordinated molecular building block. (b) Atomic charges in a fragmental cluster of *rho*-ZMOF. Color code: In, cyan; N, blue; C, grey; O, red; and H, white.

Water was represented by the flexible three-point transferable interaction potential model (TIP3P/Fs).[194] The heat of vaporization predicted by TIP3P/Fs model is 43.68 kJ/mol, very close to the experimental value 43.93 kJ/mol. This model also satisfactorily reproduces the essential aspects of water vibration. The intramolecular interaction u^{intra} in TIP3P/Fs includes harmonic bond-stretching and bond-bending potentials

$$u^{\text{intra}} = \frac{k_b}{2}\left[(r_{\text{OH}_1} - r^{\text{o}}_{\text{OH}})^2 + (r_{\text{OH}_2} - r^{\text{o}}_{\text{OH}})^2\right] + \frac{k_\theta}{2}(\theta_{\angle\text{HOH}} - \theta^{\text{o}}_{\angle\text{HOH}})^2 \quad (2.1)$$

where force constant k_b = 4427.297 kJ/mol/Å^2 and equilibrium bond length r^{o}_{OH} = 0.96 Å; force constant k_θ = 284.604 kJ/mol/rad^2 and equilibrium bond angle $\theta^{o}_{\angle HOH}$ = 104.5°. The intermolecular u^{inter} is a combination of Lennard-Jones (LJ) and Coulombic potentials

$$u^{inter}(r) = \sum_{i,j} 4\varepsilon_{ij}\left[\left(\frac{\sigma_{ij}}{r_{ij}}\right)^{12} - \left(\frac{\sigma_{ij}}{r_{ij}}\right)^{6}\right] + \frac{q_i q_j}{4\pi\varepsilon_0 r_{ij}} \tag{2.2}$$

where ε_{ij} and σ_{ij} are LJ well depth and collision diameter, q_i is the atomic charge on *i*th atom, $\varepsilon_0 = 8.8542\times10^{-12}\ C^2N^{-1}m^{-2}$ is the permittivity of vacuum. Table 2.1 lists the corresponding LJ parameters and atomic charges.

The atomic charges of *rho*-ZMOF framework were calculated by density-functional theory (DFT) on a fragmental cluster shown in Figure 2.1b. It has been commonly recognized that quantum mechanically derived charges fluctuate appreciably with small basis sets. Nevertheless, they tend to converge beyond the basis set 6-31G(d). Consequently, 6-31G(d) was used in our DFT calculations for all atoms except In atoms, for which LANL2DZ basis set was used. The DFT computations used the Lee-Yang-Parr correlation functional (B3LYP) and were carried out with Gaussian 03 package.[195] It is noteworthy that the concept of atomic charges is solely an approximation and currently no unique straightforward method is available to determine atomic charges rigorously. In our study, the atomic charges were estimated by fitting to the Electrostatic Potential (ESP). The nonframework ions considered were alkali Li^+, Na^+ and Cs^+ each with a positive unit charge. The dispersion interactions of framework atoms and ions were represented by the LJ potential with parameters from the universal force field (UFF),[167]

as listed in Table 2.1. The Lorentz-Berthelot combining rules were used to estimate the cross LJ parameters between water, ions and framework atoms. Our recent study showed UFF can predict water adsorption in Na-exchanged ETS-10 fairly well.[186]

Table 2.1. Potential parameters for water atoms (OW and HW), ions (Li^+, Na^+ and Cs^+) and framework atoms (In, N, O, C and H).

atom/ion	σ (Å)	ε (kJ/mol)	q (e)
OW	3.1506	0.6362	–0.834
HW	0	0	+0.417
Li^+	2.184	0.104	+1
Na^+	2.658	0.126	+1
Cs^+	4.024	0.188	+1
In	3.976	2.504	Shown in Figure 2.1b
N	3.260	0.288	
O	3.118	0.251	
C	3.431	0.439	
H	2.571	0.184	

The locations of Na^+ ions in dehydrated Na-*rho*-ZMOF were characterized using Monte Carlo (MC) simulation in canonical ensemble (NVT) at 298 K. The simulation box contained a unit cell of *rho*-ZMOF with 48 Na^+ ions and the periodic boundary conditions were applied in three dimensions. The unit cell was divided into three-dimensional grids with the potential energy maps tabulated in advance and then used by interpolation during simulation. In such as way, the simulation was accelerated by two orders of magnitude. A spherical cutoff of 15.0 Å was used to evaluate the LJ interactions, and beyond the cutoff the usual long-range corrections for homogeneous system were used. For the Coulombic interactions, a simple spherical truncation could

result in significant errors; consequently, the Ewald sum with a tin-foil boundary condition was used. The real/reciprocal space partition parameter and the cutoff for reciprocal lattice vectors were chosen to be 0.2 $Å^{-1}$ and 8, respectively, to ensure the convergence of the Ewald sum. The 48 Na^+ ions were introduced into the system randomly and followed by 10^7 trial moves. Two types of trial moves were used with equal probability, including displacement and regrowth. In the former, a randomly chosen Na^+ ion attempted to move around its initial position; in the latter, Na^+ ion attempted to grow in a randomly selected position which could be considered as 'jump move' in the entire simulation box.

Grand canonical Monte Carlo (GCMC) simulations were carried out for water adsorption in Li-, Na- and Cs-exchanged *rho*-ZMOF at 298 K. Because the chemical potentials of adsorbate in adsorbed and bulk phases are identical at thermodynamic equilibrium, GCMC simulation allows one to directly relate the chemical potentials of adsorbate in both phases and has been widely used to simulate adsorption. In this study, the bulk phase was vapor water at room temperature and thus behaved approximately as ideal gas. The framework was assumed to be rigid during simulation because adsorption involves low-energy equilibrium configurations and the framework flexibility has only a marginal effect. The potential energy between framework and each type of adsorbate atom or ion was pre-tabulated. The LJ interactions and Coulombic interactions were calculated using the same way as in the NVT simulation mentioned above. The number of trial moves in a typical simulation was 2×10^7, though additional trial moves were used at high loadings. The first 10^7 moves were used for equilibration and the subsequent 10^7 moves for ensemble averages. Five types of trial moves were randomly attempted in

the GCMC simulation, namely, displacement, rotation, and partial regrowth at a neighboring position; complete regrowth at a new position; and swap with the reservoir including creation and deletion with equal probability. The nonframework ions were allowed to move, and as discussed below, the locations of ions were indeed altered upon water adsorption.

Molecular dynamics (MD) simulations were performed to examine the dynamics of Na^+ ions in dehydrated Na-*rho*-ZMOF and the mobility of adsorbed water in wet Na-*rho*-ZMOF. The Nosé-Hoover thermostat was used to maintain temperature at 298 K. The initial configurations were taken from the above MC simulations. In MD simulations, 1 ns equilibration and 2 ns production were conducted. The potential and kinetic energies were monitored to ensure equilibration. A time step of 1 fs was used to ensure proper energy conservation. Trajectory in production run was saved every 1 ps to calculate the mean-squared displacements (MSDs) of water. In addition, a 20 ps trajectory was saved every 1 fs to calculate the velocity-autocorrelation functions of hydrogen atoms in water, which were then used to obtain vibrational spectra. DL_POLY program was used in the MD simulations.[196]

2.3 Results and Discussion

First, the locations and dynamics of Na^+ ions are characterized in Na-*rho*-ZMOF. Then, the density contours and structural properties are presented for water adsorption in Na-*rho*-ZMOF, as well as the adsorption isotherms and isosteric heats in *rho*-ZMOF with different types of ions. Finally, the mobility of water is examined in Na-*rho*-ZMOF; the vibrational spectra of water are shown to investigate how vibration is affected by confinement and interplayed with ions.

2.3.1 Locations and Dynamics of Na^+ Ions

Na^+ ions in Na-*rho*-ZMOF were characterized in our previous study and briefly described here.[197] Figure 2.2a shows two types of favorable sites for Na^+ ions.

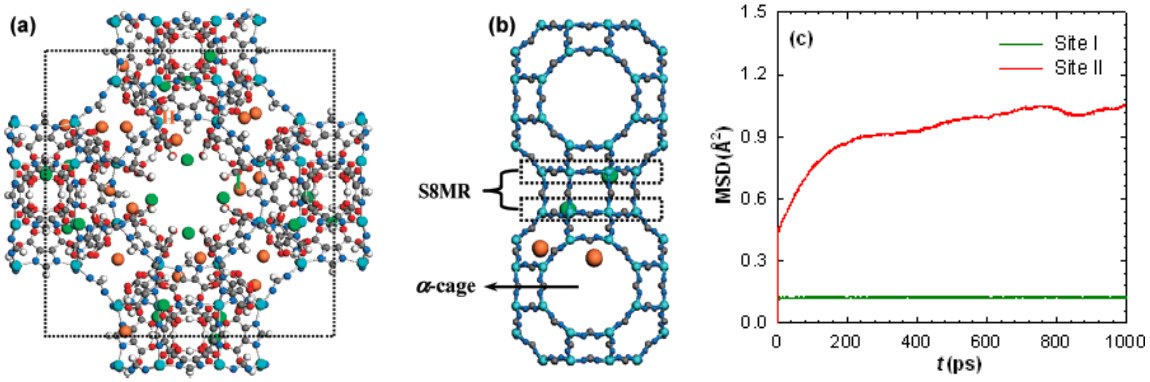

Figure 2.2. Locations of Na^+ ions in Na-*rho*-ZMOF. Site I (green) is at the single eight-membered ring (S8MR), while site II (orange) is in the α-cage. (a) unit cell and (b) eight-membered ring and α-cage. Color code: In, cyan; N, blue; C, grey; O, red; and H, white. (c) Mean squared displacements of Na^+ ions.

Site I is at the single eight-membered ring (S8MR) and near the entrance to the truncated cuboctahedron (α-cage). Two S8MRs in neighboring unit cells form a double eight-membered ring (D8MR). The distance from site I to the nearest In atoms in S8MR is 5.0 ~ 5.3 Å and approximately 7.8 Å to the next-to-nearest In atoms in the D8MR. Site II is in the α-cage and proximal to the four-membered ring (4MR). In one unit cell, twenty six Na^+ ions are located at site I and the remaining at site II. The distribution of nonframework ions in the two sites is governed by the attractions between ions and framework, in addition to the repulsions between ions. Compared to site II, site I has a larger coordination number with neighboring atoms in the octagonal S8MR, thus a stronger interaction with the framework. The sites identified here match fairly well with those of Mg^{2+} ions in *rho*-ZMOF.[193] Nevertheless, a slight difference is observed between

monovalent Na^+ and divalent Mg^{2+}. To compensate the framework charges, Mg^{2+} ions are located in less anchored positions in the framework and thus near the center of 4MR in the α-cage. In contrast, the number density of Na^+ ions is doubled and they anchor closer to the framework. Interestingly, the two types of binding sites in *rho*-ZMOF resemble those in its inorganic counterpart *rho*-zeolite.[198] In the latter, however, an additional type of site is located at the center of the D8MR and equally distanced from both S8MRs.

Figure 2.2c shows the dynamics of Na^+ ions in Na-*rho*-ZMOF calculated from MD simulation. The mobility of Na^+ at site II is greater than at site I due to the relatively weaker interaction with framework and the larger void space available around site II. However, the overall mobility of Na^+ ions in *rho*-ZMOF is generally small. This is attributed to the strong electrostatic interactions of ion-framework and the degenerated favorable sites away from each other, which largely prohibits ion hopping within the nanosecond time scale of the MD simulation. In addition, the steric hindrance of metal atoms connecting organic linkers also reduces ion mobility.

2.3.2 Adsorption of Water

Figure 2.3 shows the density contours of adsorbed water in Na-*rho*-ZMOF at 10^{-8}, 10^{-2} and 1 kPa. At 10^{-8} kPa, water molecules are localized close to Na^+ ions and scattered from one other. Therefore, Na^+ ions can be regarded as preferential adsorption sites for water. With increasing pressure to 10^{-2} kPa, water adsorption occurs primarily near the framework surface. At 1 kPa approaching saturation, the large cage is gradually filled and Na^+ ions appear to be solvated by continuously distributed water shells. Such a three-step adsorption mechanism was previously observed for water adsorption in NaX and NaY

zeolites.[199] From low to high pressure, the locations of Na^+ ions are observed to shift upon water adsorption. It is also found that water adsorbs preferentially near Na^+ ions at site II rather than at site I. This is attributed primarily to the steric effect, as shown in Figure 2.2b, the void space near site II in the α-cage is larger than at site I.

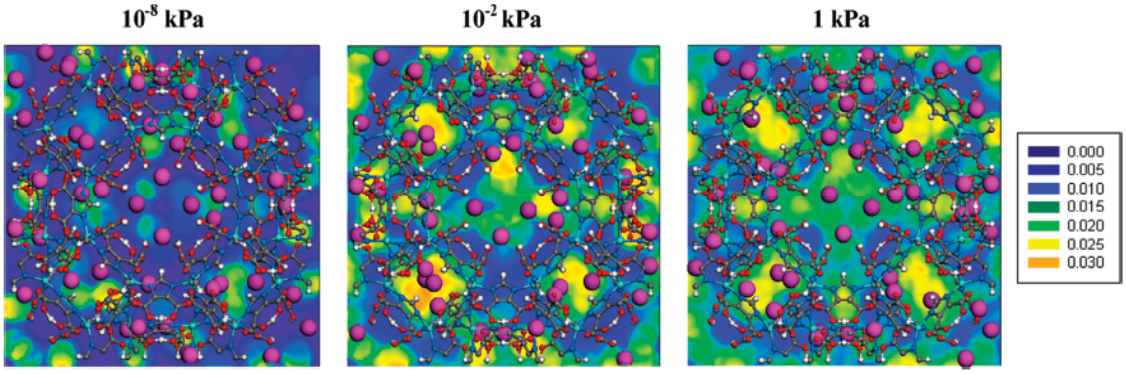

Figure 2.3. Density contours of water in Na-*rho*-ZMOF at 10^{-8}, 10^{-2} and 1 kPa. Na^+ ions are represented by the large pink spheres. The density is based on the number of water molecules per $Å^3$.

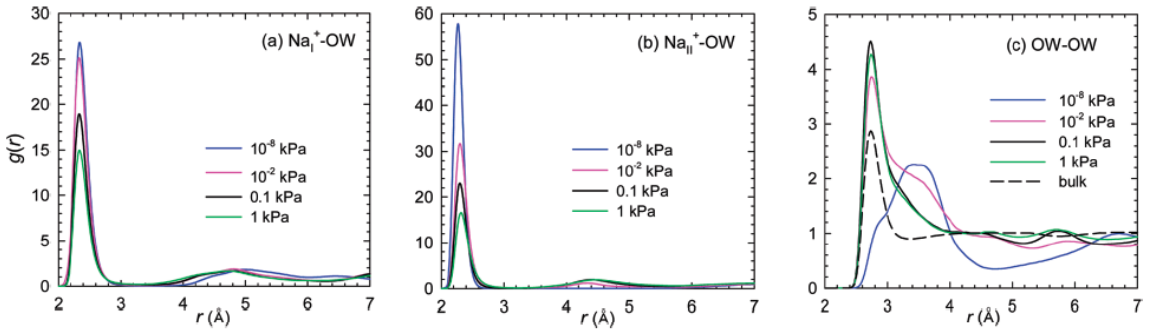

Figure 2.4. Radial distribution functions of (a) Na_I^+-OW (b) Na_{II}^+-OW (c) OW-OW in Na-*rho*-ZMOF at 10^{-8}, 10^{-2}, 0.1 and 1 kPa. For comparison, $g(r)$ of OW-OW in bulk water is included as the dashed line in (c).

Figures 2.4a and 2.4b show the radial distribution functions $g(r)$ between Na^+ ions and oxygen atoms (OW) of water, calculated from

$$g_{ij}(r) = \frac{\left\langle \Delta N_{ij}(r, r+\Delta r) \right\rangle V}{4\pi r^2 \Delta r \, N_i N_j} \tag{2.3}$$

where r is the distance between species i and j, $\left\langle \Delta N_{ij}(r, r+\Delta r) \right\rangle$ is the ensemble averaged number of j around i within a shell from r to $r + \Delta r$, V is the system volume, N_i and N_j are the numbers of i and j.

For both Na_I^+-OW and Na_{II}^+-OW, a pronounced peak is observed in $g(r)$ at r = 2.3 Å and the peak height drops with increasing pressure. This is due to two factors: first, water molecules are located further away from ions; second, the average density of adsorbed water increases. As we shall see below, however, there are more water molecules around Na^+ ions as water pressure increases, i.e., Na^+ ions are solvated by more water molecules. At a given pressure, the peak height is larger in Na_{II}^+-OW than in Na_I^+-OW. This confirms that water is located predominantly near site II. Because of the increasingly cooperative attractions of adsorbed water at site II, Na^+ ions at site I are progressively shifted to site II as pressure increases. Such a redistribution of Na^+ ions is observed in Figure 2.3 and will be discussed further below. The second peak in $g(r)$ of Na-OW is indistinct, unlike the case of water adsorption in NaX and NaY.[199] This is because *rho*-ZMOF has a very open structure with extra-large cavity. Figure 2.4c shows $g(r)$ of OW-OW for water adsorption in Na-*rho*-ZMOF and for bulk water. At 10^{-8} kPa, the peak of $g(r)$ in Na-*rho*-ZMOF is located at 3.3 ~ 3.6 Å, and this relatively long distance is between the scattered water molecules near the neighboring Na^+ ions as seen in Figure 2.3. With increasing pressure, water molecules get closer, form hydration shell, and behave as bulk water. Consequently, $g(r)$ of OW-OW exhibits a peak at 2.7 Å resembling bulk water. In the literature, it was observed that the peak location of water in ionic solutions is similar to bulk water.[200]

Figure 2.5 shows the coordination numbers of water N_{water} around Na^+ ions as a function of distance *r* between ion and water. N_{water} was calculated from

$$N_{water}(r) = \rho_{water} \int_0^r g_{Na^+-water}(r') 4\pi r'^2 \, dr' \tag{2.4}$$

where ρ_{water} is the average density of water.

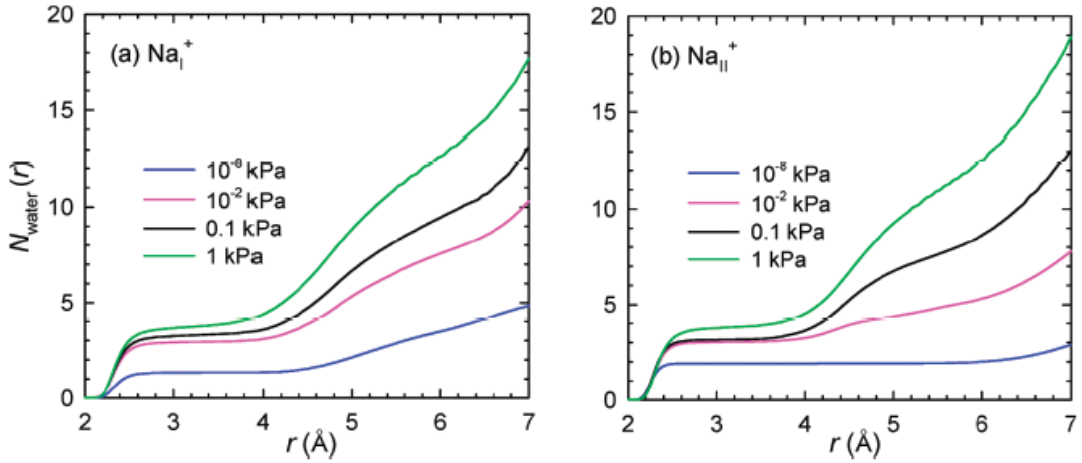

Figure 2.5. Coordination numbers of water around (a) Na_I^+ and (b) Na_{II}^+ in Na-*rho*-ZMOF at 10^{-8}, 10^{-2}, 0.1 and 1 kPa.

As seen in Figure 2.4, the peak height of g(*r*) for both Na_I^+-OW and Na_{II}^+-OW drops with increasing pressure. Nevertheless, N_{water} becomes larger with pressure at any given *r*. This simply reveals that the number of water molecules around Na^+ ions increases as pressure increases. In other words, Na^+ ions are hydrated in a greater degree. At *r* = 3.4 Å, corresponding to the first minimum of *g*(*r*) in Figures 2.4a and 2.4b, N_{water} of Na_{II}^+ is larger than that of Na_I^+, especially at 10^{-8} kPa. This further demonstrates the preferential location of water near Na^+ ions at site II rather than site I.

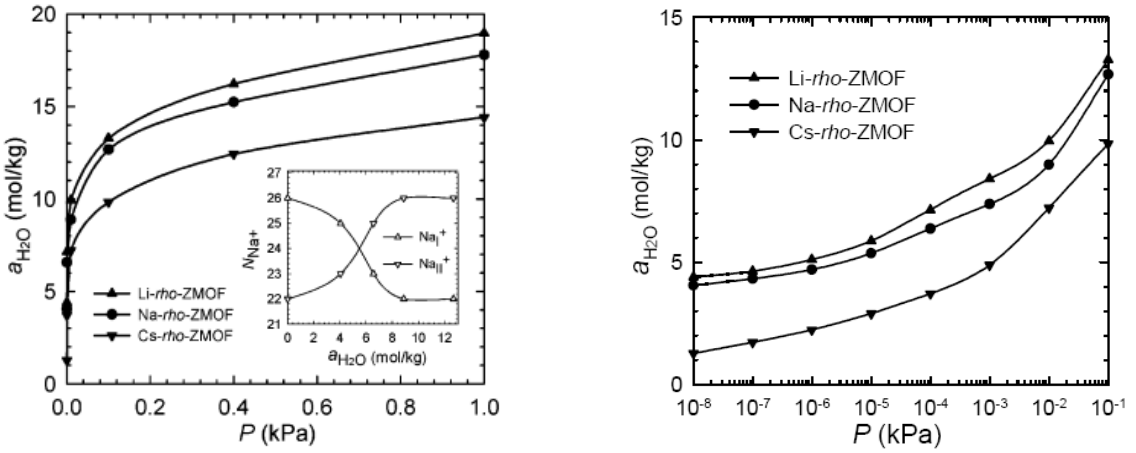

Figure 2.6. (a) Adsorption isotherms of water in Li-, Na- and Cs-exchanged *rho*-ZMOF as a function of pressure. The inset shows the numbers of Na_I^+ and Na_{II}^+ as function of water loading in Na-*rho*-ZMOF. (b) Adsorption isotherms of water in Li-, Na- and Cs-exchanged *rho*-ZMOF at low-pressure regime.

The adsorption isotherms of water in Li-, Na- and Cs-exchanged *rho*-ZMOF are shown in Figure 2.6a, as well as in Figure 2.6b at low-pressure regime. At low pressures, adsorption increases sharply, indicating a micropore-filling mechanism. This is attributed to the strong affinity of water for the ionic framework and the nonframework ions. With increasing pressure, adsorption tends to approach saturation. The isotherms in all three systems exhibit same shape and belong to type I as classified by IUPAC. Nevertheless, the extent of adsorption is the largest in Li-*rho*-ZMOF, followed by Na-*rho*-ZMOF and Cs-*rho*-ZMOF. In other words, adsorption becomes weak with increasing size of alkali ion in *rho*-ZMOF. The porosity is estimated to be 0.55, 0.54 and 0.50 in Li-, Na- and Cs-exchanged *rho*-ZMOF, respectively. A smaller ion interacts with water more strongly due to greater local electric fields around the ion. With increasing ionic size, the interaction between ion and water is reduced, in addition to the free volume. These results are in good accordance with water adsorption in cation-exchanged FAU zeolite.[201]

The inset of Figure 2.6a shows the numbers of Na^+ ions at site I and II as a function of loading. As loading increases, Na_I^+ ions decrease from 26 to 22 and correspondingly Na_{II}^+ ions increase from 22 to 26. As discussed above, the redistribution of Na^+ ions from site I to II is due to the preferential adsorption of water near Na_{II}^+ ions, which in turn exerts attractive force on Na_I^+ ions and facilitates them to relocate. In our recent study, the redistribution of Na^+ ions in Na-ETS-10 was also observed upon water adsorption.[186]

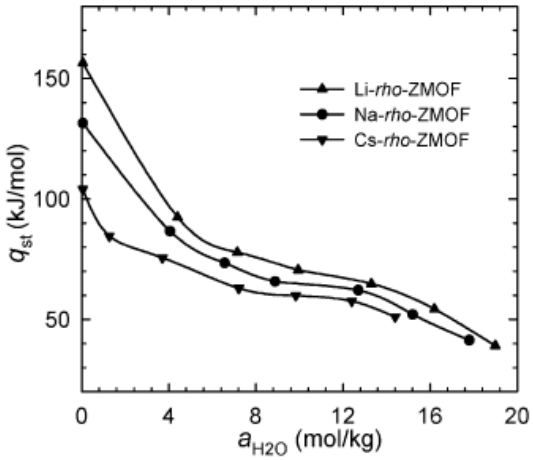

Figure 2.7. Calculated isosteric heats of water adsorption in Li-, Na- and Cs-exchanged *rho*-ZMOF as a function of loading.

The isosteric heat of water adsorption was calculated from

$$Q_{st} = RT - \left[\frac{\partial (U_{total} - U_{intra})}{\partial a} \right]_{T,V} \tag{2.5}$$

where R is gas constant, a is loading of water, U_{total} is the total adsorption energy including contributions from both adsorbate-adsorbent and adsorbate-adsorbate interactions, and U_{intra} is the intramolecular energy of water. Compared with adsorption isotherm, isosteric heat is more sensitive to loading thus more commonly used to ascertain adsorption mechanism. Figure 2.7 shows Q_{st} of water in Li-, Na- and Cs-exchanged *rho*-ZMOF as a function of loading. At infinite dilution, Q_{st} is about 156.4,

131.5 and 104.1 kJ/mol in Li-, Na- and Cs-*rho*-ZMOF, respectively. At any given loading, Q_{st} in Cs-*rho*-MOF is consistently smaller than in Li- and Na-*rho*-ZMOF. As discussed earlier, this is because the electrostatic interaction of water with larger cation is weaker. The decrease in isosteric heat with increasing size of cation was previously observed in cation-exchanged zeolites.[201] In all-silica MFI and BEA, Q_{st} is in the range of 80 – 50 kJ/mol, significantly lower than in the proton-exchanged counterparts.[202] This reveals that the framework charges and nonframework ions play a crucial role in water adsorption. In all the three systems, Q_{st} drops as loading rises indicating the energetic heterogeneity of the framework. With a closer look, we can find three regions with different slopes, particularly in Li-*rho*-ZMOF: 0 – 5 mol/kg, 5 – 15 mol/kg, and beyond 15 mol/kg. This corresponds to the three-step adsorption observed in Figure 2.3. Water is initially adsorbed onto the nonframework ions, then close to the framework surface, and finally in the large cage. Near saturation, Q_{st} approaches a value of 40 ~ 50 kJ/mol, which is approximately the enthalpy of vaporization of bulk water.

Figure 2.8 shows the locations of water in Li-, Na- and Cs-exchanged *rho*-ZMOF at a bulk pressure of 10^{-8} kPa. For clarity, only water molecules in the S8MR are shown. The adsorbed water molecules interact with the nonframework ions and carbonyl groups. The distance between water and ion is approximately 2.1 – 2.3 Å in Li-*rho*-ZMOF, 2.3 – 2.5 Å in Na-*rho*-ZMOF, and 3.1 – 3.7 Å in Cs-*rho*-ZMOF. The distance increasing from Li-, Na- to Cs-*rho*-ZMOF is attributed to the reduced electrostatic interaction for larger cation, as discussed earlier. This trend was also observed for CO_2 adsorption in ion-exchanged FAU zeolites.[203] Due to the formation of H-bonds, interestingly, water

molecules in all the three *rho*-ZMOF are oriented in such a way that the hydrogen atoms point toward the carbonyl groups.

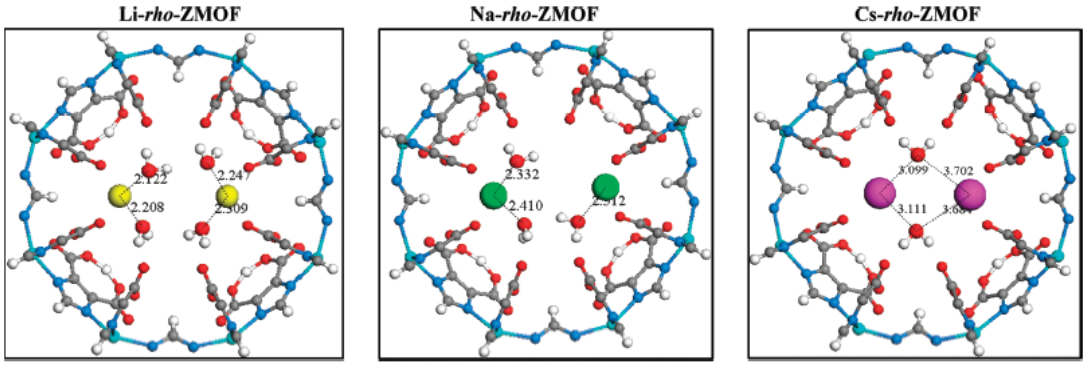

Figure 2.8. Locations of water in the single 8-membered ring in Li-, Na- and Cs-exchanged *rho*-ZMOF at 10^{-8} kPa. Color code: In, cyan; N, blue; C, grey; O, red; H, white; Li^+, yellow; Na^+, green; and Cs^+, pink. The distances between water and ions are in Angstroms.

2.3.3 Mobility of Water

The mobility of water was analyzed by mean-squared displacement (MSD) from MD simulation

$$\mathrm{MSD}(t) = \frac{1}{KN}\sum_{k}^{K}\sum_{i=1}^{N}\left|\mathbf{r}_i(t+t_k) - \mathbf{r}_i(t_k)\right|^2 \tag{2.6}$$

where t is time, N is the number of water molecules, and $\mathbf{r}_i(t)$ is the position of ith water at time t. The multiple time-origin method was used to evaluate MSDs and K is the number of time origins. Figure 2.9a shows the MSDs of water in Na-*rho*-ZMOF at various pressures. At a low pressure, water is strongly adsorbed onto the nonframework ions. Thus, water exhibits a local motion around ions with a negligible mobility. With increasing pressure, ions are gradually solvated by hydration shells and water experiences less interaction with ions; consequently, water can move relatively free in the large cavity and the mobility increases. Near saturation, however, steric hindrance plays a dominant

role; that is, there is no large room available for motion and hence the mobility is retarded. In principle, if all the empty space is filled, molecules cannot hop from one place to other and mobility becomes essentially zero. The trend is similar to the behavior of water in Na-ETS-10 and FAU zeolite.[199]

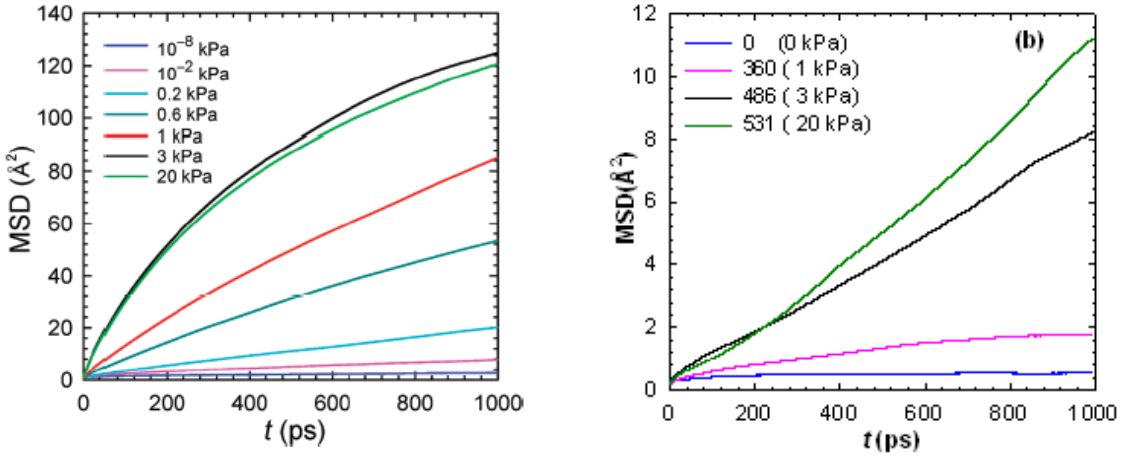

Figure 2.9. (a) Mean-squared displacements of water and (b) Na^+ ions in Na-*rho*-ZMOF at various pressures.

The dynamics of nonframework Na^+ ions can be substantially affected by adsorbed water. In Figure 2.9b, MSD of Na^+ ions are shown in Na-*rho*-ZMOF at different water loadings (with 360, 486 and 531 water molecules in one unit cell). Like in dehydrated Na-*rho*-ZMOF, the mobility of Na^+ ions is marginal at a loading less than 486. Interestingly, several Na^+ ions are found to move rather fast at loading of 486 or 531, implying that the dynamics of ions can be enhanced in the presence of sufficient amount of water. This is attributed to the strong interactions of water with the ionic framework and nonframework ions, which substantially perturbs ion distribution and promotes ion migration.

2.3.4 Vibration of Water

Spectroscopy is commonly used to probe the structure and dynamics of fluids. The peak position, bandwidth and intensity of spectra in confined space are different from those in bulk phase, and extremely sensitive to the changes of geometry and strength upon confining. To obtain the vibrational information of water adsorption in Na-*rho*-ZMOF, the normalized velocity autocorrelation functions (VACFs) $C_v(t)$ were estimated from MD simulation

$$C_v(t) = \frac{\langle u(0) \cdot u(t) \rangle}{\langle u(0) \cdot u(0) \rangle} \tag{2.7}$$

where $v(t)$ is the velocity of hydrogen atoms of water at time t. The spectra were then calculated by the Fourier transform of VACFs,

$$I(v) = \int_0^{+\infty} C_v(t) \cos(vt)\, \mathrm{d}t \tag{2.8}$$

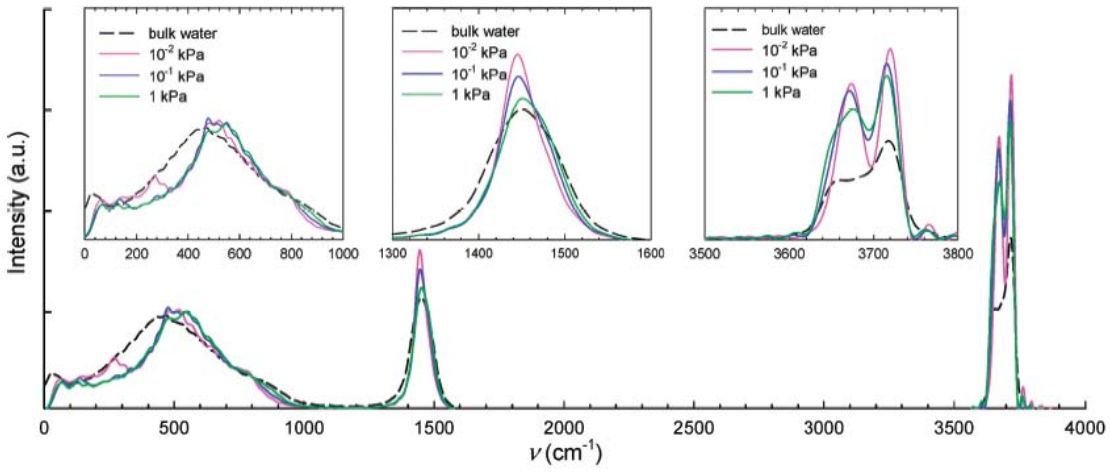

Figure 2.10. Vibrational spectra of water in Na-*rho*-ZMOF at various pressures and in bulk water.

where v is freequecny. Figure 2.10 shows the simulated vibrational spectra of water in Na-*rho*-ZMOF at various pressures. For comparison, the spectra of bulk water were also

calculated and found to be consistent with the literature results.[204] Three distinct bands are observed for water in Na-*rho*-ZMOF, corresponding to the librational motion, H-O-H bending, and H-O stretching of water, respectively. The frequency of librational motion in *rho*-ZMOF (500 cm^{-1}) is higher than in bulk water (~ 420 cm^{-1}). As pressure increases, the confinement effect is enhanced and a blue shift is observed in the peak. A similar effect was observed for the librational motion of water in FER zeolite.[205] For H-O-H bending, the frequency in *rho*-ZMOF is around 1440 cm^{-1}, slightly lower than in bulk water (1450 cm^{-1}). With increasing pressure, however, the bending frequency exhibits a blue shift and is closer to bulk water. This is because of the increasing coordination with the increased number of surrounding water molecules.[206] Consequently, the behavior of confined water gradually approaches bulk water and the number of H-bonds increases. The two pronounced frequencies around 3670 and 3720 cm^{-1} are identified to be the symmetric and asymmetric modes of H-O stretching. The splitting of symmetric and asymmetric modes, occurred particularly at low loadings, is similar to the behavior of interfacial water.[207] This is attributed to the strong interactions between water and cations, which break the regular tetrahedral arrangement of water and lead to a decrease in the number of H-bonds. As loading increases, the coordination with the surrounding water molecules becomes stronger and the stretching band has a red shift and is close to bulk water.

Among the three vibrational modes, the H-O stretching is very sensitive to the change in the connectivity degree of H-bond network in the surrounding water, while the librational motion and H-O-H bending depend largely on the local arrangement of water molecules.[208] In a porous material with structure-making capability, the confined water

behaves close to bulk water; consequently, the librational motion and H-O-H bending are generally similar to bulk water. For all the three bands in Na-*rho*-ZMOF, the spectral intensity and width exhibit similar trend as a function of pressure. At a low pressure, the intensity is large because water is adsorbed onto cations and scattered, thus the distance of H-bond is long and the vibration has great amplitude; and the width is narrow due to the limited number of H-bonds. At a high pressure, water molecules stay close to one another and the number of H-bonds increases; consequently, the spectra have small amplitude and wide bandwidth.

2.4 Conclusions

The adsorption, mobility and vibration of water in ion-exchanged *rho*-ZMOF have been investigated using atomistic simulations. As a 4-connected ZMOF with topology similar to *rho*-zeolite, *rho*-ZMOF is a very open-framework with extra-large cavity. Two types of favorable sites were identified for Na^+ ions in dehydrated Na-*rho*-ZMOF. Site I is at the single eight-membered ring and site II is in the α-cage. Ions at site I have a larger coordination number with the neighboring atoms and hence stronger interaction with the framework. The locations of Na^+ ions are largely in accordance with Mg^{2+} ions in Mg-*rho*-ZMOF and resemble those in *rho*-zeolite. The mobility of Na^+ ions in dehydrated *rho*-ZMOF is generally small.

Attributed to the high affinity for the ionic framework and the nonframework ions, water is strongly adsorbed in *rho*-ZMOF with a three-step adsorption mechanism. At a low pressure, water is adsorbed proximally to Na^+ ions. With increasing pressure, adsorption occurs near the framework, and finally in the large cage. Interestingly, water is adsorbed preferentially near Na^+ ions at site II; Na^+ ions at site I are progressively shifted

to site II upon water adsorption. With increasing pressure, water molecules get closer, form hydration shells around ions, and behave largely like bulk water. For different ions (Li^+, Na^+ and Cs^+), the interaction between ion and water is reduced with increasing ionic size. Consequently, the extent of adsorption and isosteric heat decrease following the order of Li-*rho*-ZMOF, Na-*rho*-ZMOF, and Cs-*rho*-ZMOF.

Water exhibits a negligible local motion around ions at a low pressure. Nevertheless, the mobility increases with pressure and finally decreases upon saturation. The mobility of Na^+ ions is enhanced at sufficiently high loadings of water. Three distinct spectral bands were observed for water in Na-*rho*-ZMOF, corresponding to the librational motion, bending, and stretching of water, respectively. The frequency of librational motion is blue shifted from that of bulk water, attributed to the confinement effect. With increasing pressure, the bending exhibits a blue shift because of the increasing coordinative attraction of water. The stretching splits into symmetric and asymmetric modes at low pressures due to the strong water-cation interaction, and approaches the band of bulk water as pressure increases. For the three bands of water vibration in Na-*rho*-ZMOF, the spectral amplitude drops and the width broadens with increasing pressure.

Chapter 3

Water and Alcohols in Hydrophilic and Hydrophobic Zeolitic MOFs

3.1 Introduction

Most experimental and theoretical studies in MOFs to date have been focused on gas storage and separation. For example, CO_2 adsorption was determined in a series of MOFs and MOF-177 was found to exhibit a high capacity up to 33 mmol/g.[58] Adsorption of various gases in MOFs were simulated and compared with experimental data to test the proposed atomic models.[209,210] H_2 uptake in IRMOFs from simulations was found to correlate well with isosteric heat at low pressures, with surface area at moderate pressures, and with free volume at high pressures.[211] The adsorption and selectivity of CO_2/CH_4 mixture were simulated in IRMOF-1 and Cu-BTC.[212,213] The permeability and separation were predicted for CO_2/H_2, CO_2/CH_4 and CO_2/H_2 mixtures in IRMOF-1 and Cu-BTC membranes.[214,215] Carborane-based MOFs in the presence and absence of exposed metal sites were examined for the separation of CO_2/CH_4 mixture, and a higher selectivity was observed in the former case.[216]

Nevertheless, a few studies have investigated the adsorption of water and alcohols in MOFs. In a pillared-layer MOF with one-dimensional semi-rectangular pores, water adsorption was experimentally determined.[139] Hydrophobic paddle-wheel MOFs were found to exhibit substantial adsorption of alcohols.[71,72] Water adsorption in Cu-BTC was found to be sensitive to the framework charges, with a larger affinity for metal sites compared to light gases.[191] The hydrophobicity and stability of Cu-BTC, ZIF-8, MIL-101, DUT-4 toward moisture were measured.[128] The size-based selective adsorption of

water over methanol was observed in a rationally tuned microporous MOF.[217] It was demonstrated that dehydratable-hydratable water stable MOF could be used for low-temperature heating and cooling.[131]

For applications in aqueous media or organic solvents, chemically stable MOFs are desired. However, most common MOFs cannot meet this requirement. Recently, zeolite-like MOFs (ZMOFs) and zeolitic-imidazolate frameworks (ZIFs) have attracted considerable attention.[218,219] They have topologies resembling inorganic zeo-type networks and exhibit similar structural properties. Intriguingly, the substitution of oxygen atoms in zeolites with tunable organic linkers leads to extra-large cavities. More importantly, ZMOFs and ZIFs are exceptionally stable and remarkably resistant to water and organic solvents. These salient features facilitate their potential applications in catalysis, separation, biofuel dehydration, etc. A highly porous ZMOF with large cavities was found to be catalytically active pertinent to large molecules.[110] Ionic ZMOFs containing charge-balancing nonframework ions were demonstrated to enhance H_2 storage.[193] Unprecedentedly high selective adsorption of industrially important CO_2-containing gas mixtures was predicted in ionic ZMOFs.[197] ZIFs have been examined for the adsorption of small gases[220-224] and hydrocarbons.[225]

Molecular design of MOFs with zeolitic topologies is currently very active. While new ZMOFs and ZIFs are being discovered, exploring their scope for practical applications is still in an infant stage. Toward this end, a clear fundamental understanding for the microscopic properties of guest molecules in these nanoporous structures is indispensable. In this work, we report a molecular simulation study on the adsorption of water and alcohols (methanol and ethanol) in two MOFs with *rho*-type topology, one is

hydrophilic Na-*rho*-ZMOF and the other is hydrophobic ZIF-71. While Na-*rho*-ZMOF consists of an anionic framework and nonframework Na^+ ions, ZIF-71 is non-ionic in nature. Both Na-*rho*-ZMOF and ZIF-71 possess a three dimensional pore network formed by large α-cages interconnected via small windows. In Na-*rho*-ZMOF, two types of binding sites exist for Na^+ ions, in which site I is at the single eight-membered ring (S8MR) and site II is in the α-cage.[197]

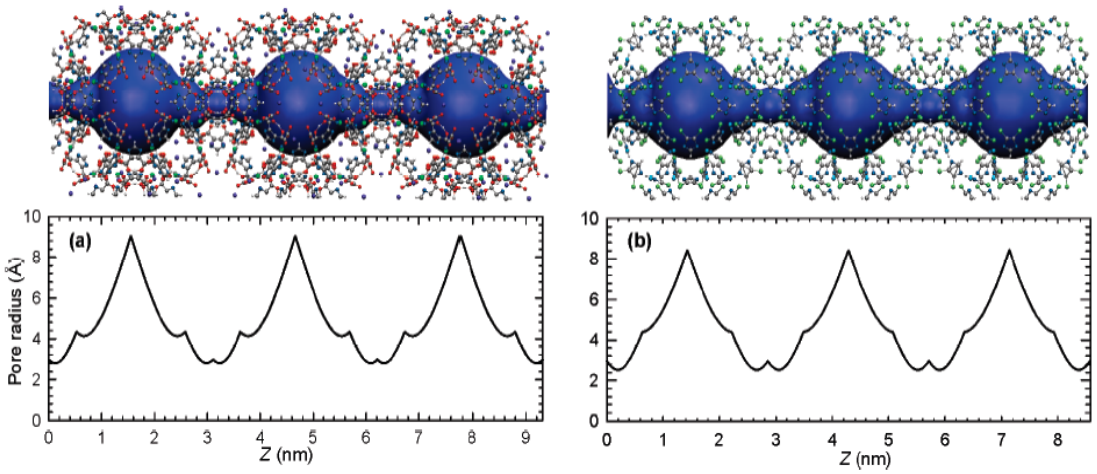

Figure 3.1. Pore morphologies and radii in (a) Na-*rho*-ZMOF and (b) ZIF-71. Color code: In/Zn, cyan; N, blue; C, grey; O, red; Cl, green; and H, white; and Na^+, purple.

Figure 3.1 shows the pore morphologies and radii estimated by the HOLE program.[226] Na-*rho*-ZMOF and ZIF-71 have identical pore morphologies with alternating cages and windows along the pore axis. The cage radii are approximately 9.1 and 8.4 Å in Na-*rho*-ZMOF and ZIF-71, respectively. The window radii are 2.8 and 2.4 Å, respectively, which allow water, methanol and ethanol (kinetic diameters 2.65, 3.36 and 4.40 Å) to enter. We investigated the adsorption of pure and mixed water/alcohols in Na-*rho*-ZMOF and ZIF-71 at 298 K. The extents of adsorption, selectivities of mixtures, and adsorption mechanisms are examined comprehensively.

3.2 Models and Methods

In Sections 2.2, *rho*-ZMOF model has been described in detail. *Rho*-ZMOF has a space group of *Im-3m* and a lattice constant of 31.062 Å (Figure 3.2a).[218] We have identified that there are two types of binding sites for the nonframework Na^+ ions in Na-*rho*-ZMOF. Site I is at the single eight-membered ring (S8MR) and site II is in the α-cage. Compared to site II, Na^+ ions at site I have a stronger affinity for the framework and thus a smaller mobility. Nevertheless, the dynamics of Na^+ ions in Na-*rho*-ZMOF can be regarded as local vibrations at their favorable binding sites and the overall mobility is small.[197,227]

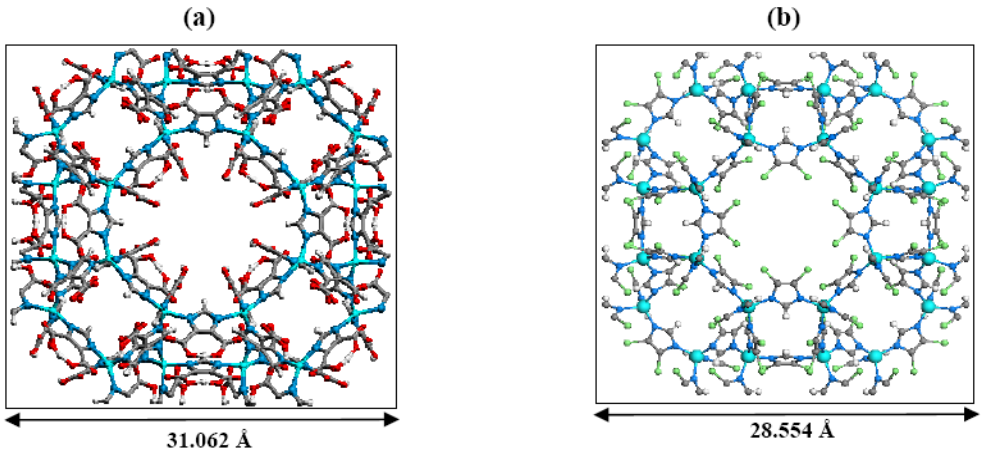

Figure 3.2. Unit cells of (a) *rho*-ZMOF and (b) ZIF-71. Color code: In/Zn, cyan; N, blue; C, grey; O, red; Cl, green; and H, white. The nonframework Na^+ ions in *rho*-ZMOF are not shown.

ZIF-71 has a space group of *Pm-3m* and a lattice constant of 28.554 Å (Figure 3.2b). A unit cell of ZIF-71 possesses a truncated cuboctahedron (α-cage) with 48 Zn atoms. Each Zn atom is coordinated with four N atoms of 4,5-dicholoroimidazolate ligands to form four-coordinated molecular building block (Figure 3.3a). The framework contains large cages of 16.8 Å connected by windows of 4.8 Å.[220] The substitution of oxygen in *rho*-zeolite with imidazolate-based ligands leads to a very open framework in ZIF-71,

almost twice as large as in *rho*-zeolite. Both *rho*-ZMOF and ZIF-71 are formed by the assembly of tetrahedral building units (TBUs). As illustrated in Figure 3.4, the neighboring truncated cuboctahedra (α-cages) in the two MOFs are connected through a double eight-member ring (D8MR).

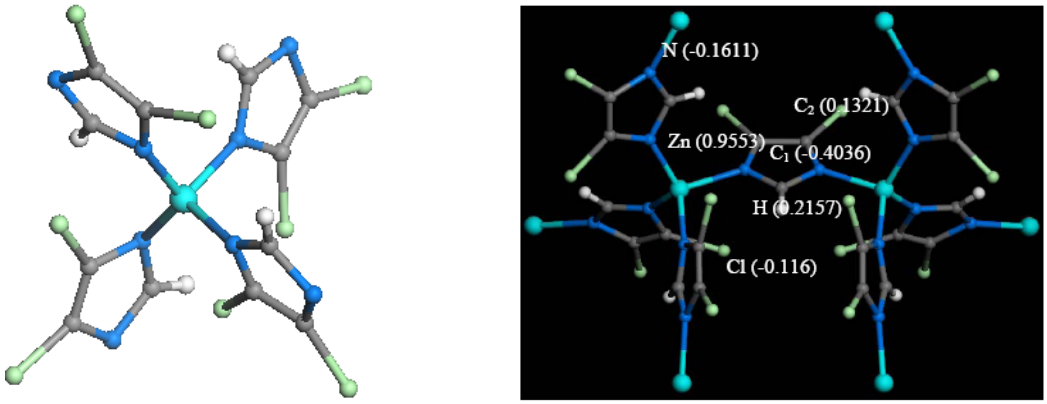

Figure 3.3. (a) four-coordinated molecular building block. (b) Atomic charges in the fragmental clusters ZIF-71. Color code: Zn, cyan; N, blue; C, grey; O, red; Cl, green; and H, white.

Similar to the case of *rho*-ZMOF as described in Section 2.2, the charges of ZIF-71 framework atoms were calculated by density-functional theory (DFT) on a fragmental cluster shown in Figure 3.3b. The 6-31G(d) basis was used for all atoms except metal atoms, for which LANL2DZ basis set was used. LANL2DZ is a double-zeta basis set and contains effective pseudo-potentials to represent the potentials of nucleus and core electrons. The atomic charges were fitted to the electrostatic potentials using the Merz-Kollman scheme.[228,229] The dispersion interactions of the framework atoms in both *rho*-ZMOF and ZIF-71 were represented by the Lennard-Jones (LJ) potential with parameters from the universal force field (UFF) in consistent with the previous study. A number of simulation studies have shown that UFF can accurately predict adsorption in various MOFs.[209,210,230,231]

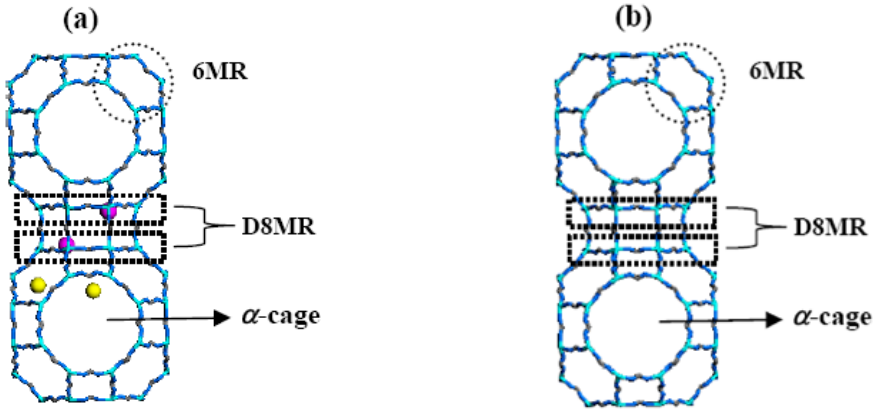

Figure 3.4. Zeolite-analogue representation of (a) Na-*rho*-ZMOF and (b) ZIF-71. Two types of binding sites exist for Na^+ ions in Na-*rho*-ZMOF, in which site I (pink) is at the single eight-membered ring (S8MR) and site II (yellow) is in the α-cage. The two S8MRs form a double eight-membered ring (D8MR).

Table 3.1. Potential parameters of adsorbates (water, methanol and ethanol).

Adsorbates	LJ parameters and charges				Bond stretching	Bond bending
	site	σ (Å)	ε/k_B (K)	q (e)		
water	O	3.151	76.47	–0.834	$r_{H\text{-}O}$ = 0.96 Å	$\theta_{\angle H\text{-}O\text{-}H}$ = 104.52°
	H	0	0	+0.417	k_b/k_B = 533020.66 K	k_θ/k_B = 34264.61 K
methanol	CH_3	3.75	98.0	+0.265	$r_{CH3\text{-}O}$ = 1.43 Å	$\theta_{\angle CH3\text{-}O\text{-}H}$ = 108.5°
	O	3.02	93.0	–0.700	$r_{O\text{-}H}$ = 0.945 Å	k_θ/k_B = 55400 K
	H	0	0	+0.435	(fixed bond lengths)	
ethanol	CH_3	3.75	98.0	0	$r_{CH3\text{-}CH2}$ = 1.54 Å	$\theta_{\angle CH3\text{-}CH2\text{-}O}$ = 109.47°
	CH_2	3.95	46.0	+0.265	$r_{CH2\text{-}O}$ = 1.43 Å	k_θ/k_B = 50400 K
	O	3.02	93.0	–0.700	$r_{O\text{-}H}$ = 0.945 Å	$\theta_{\angle CH2\text{-}O\text{-}H}$ = 108.5°
	H	0	0	+0.435	(fixed bond lengths)	k_θ/k_B = 55400 K

As also used in Chapter 2, water was represented by the flexible three-point transferable interaction potential model (TIP3P/Fs).[194] Methanol and ethanol were

represented by the united-atom models with CH_x as a single interaction site. The potential parameters were adopted from the transferable potentials for phase equilibria (TraPPE) force field, which was fitted to the critical properties and vapor-liquid equilibria of alkanes and alcohols.[232] The intramolecular bending and torsion interactions were also taken into account

$$u_{\text{bending}}(\theta) = 0.5 k_\theta (\theta - \theta^{\text{o}})^2 \tag{3.1}$$

$$u_{\text{torsion}}(\phi) = c_0 + c_1[1 + \cos\phi] + c_2[1 - \cos(2\phi)] + c_3[1 + \cos(3\phi)] \tag{3.2}$$

where $c_0/k_B = 0$, $c_1/k_B = 209.82$, $c_2/k_B = -29.17$, and $c_3/k_B = 187.93$. Table 3.1 lists the potential parameters of the adsorbates.

Grand canonical Monte Carlo (GCMC) simulations were conducted for the adsorption of pure components and binary mixtures in Na-*rho*-ZMOF and ZIF-71 at 298 K. The simulation box contained one unit cell of Na-*rho*-ZMOF or ZIF-71, with the periodic boundary conditions exerted in three dimensions. The frameworks were assumed to be rigid during simulation because adsorption involves low-energy equilibrium configurations and the framework flexibility has only a marginal effect on thermodynamic quantities. GCMC simulation procedure was the same as that in Chapter 2, thus all details were not described here. For pure component adsorption, five types of trial moves were randomly attempted namely, displacement, rotation, and partial regrowth at a neighboring position, complete regrowth at a new position, and swap between reservoir including creation and deletion with equal probability. For mixtures, the exchange of molecular identity was also conducted. The nonframework Na^+ ions in Na-*rho*-ZMOF were not fixed and could move upon adsorption.

3.3 Results and Discussion

3.3.1 Pure components in Na-*rho*-ZMOF

Figure 3.5 shows the adsorption isotherms of water, methanol, and ethanol in Na-*rho*-ZMOF up to 100 kPa, which is beyond their saturation pressures (3.1 kPa for water, 16.8 kPa for methanol, and 7.2 kPa for ethanol).[233] As observed in Chapter 2, water is strongly adsorbed in Na-*rho*-ZMOF because of high affinity with the ionic framework and nonframework ions. At a low pressure, water is preferentially adsorbed onto Na^+ ions, particularly at site II rather than site I. With increasing pressure, adsorption occurs near the framework, and finally in the large α-cage.

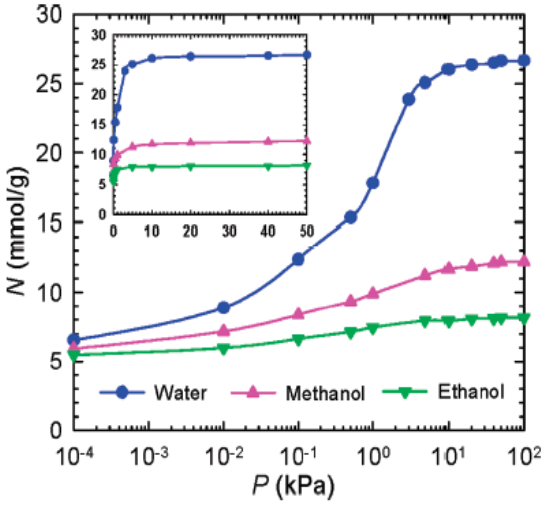

Figure 3.5. Adsorption isotherms of water, methanol, and ethanol in Na-*rho*-ZMOF. The inset shows the isotherms in the linear scale of pressure. The saturation pressure is 3.1 kPa for water, 16.8 kPa for methanol, and 7.2 kPa for ethanol.

The isotherms of water, methanol, and ethanol are of type I as classified by IUPAC with strong adsorption even at low pressures. Interestingly, methanol and ethanol exhibit qualitatively similar adsorption behavior to water; however, they differ quantitatively in the extent of adsorption. At a low pressure, the difference is small but becomes

pronounced at high pressures. Water adsorption increases in a much larger extent with increasing pressure than methanol and ethanol. The saturated adsorption capacity follows the order of water > methanol > ethanol. Apparently, the substitution of hydrogen in water by methyl and ethyl groups leads to less polar and bigger molecules. In the hydrophilic Na-*rho*-ZMOF, highly polar water is thus more strongly adsorbed than methanol and ethanol.[185] In addition, water is more associative than alcohols and thus has a higher amount of adsorption at high pressures. In cation exchanged *rho*-zeolite, the different adsorption capacities of water and alcohols were attributed to the accessibility of adsorbates to the available free space especially near the windows.[234]

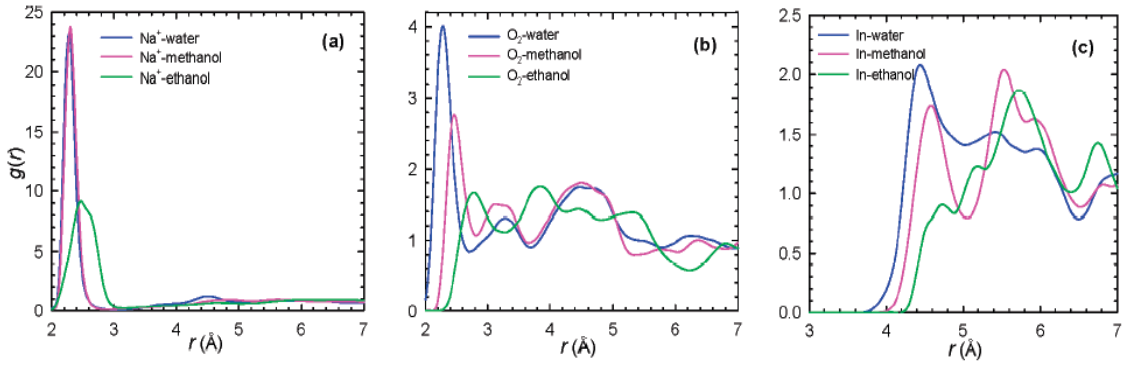

Figure 3.6. Radial distribution functions $g(r)$ of (a) Na^+-adsorbate (b) O_2-adsorbate (c) In-adsorbate for water, methanol, and ethanol in Na-*rho*-ZMOF at 10^{-4} kPa. O_2 is the carboxylic oxygen atom of the framework as shown in Figure 3.3.

To examine the structures of adsorbate molecules in Na-*rho*-ZMOF and thus provide insight into the adsorption mechanism, radial distribution functions g(r) were calculated. Figure 3.6 shows the g(r) of adsorbates around Na^+ ions, the carboxylic oxygen (O_2) and In atoms of the framework, respectively at 10^{-4} kPa. Although water, methanol, and ethanol have a close amount of adsorption at 10^{-4} kPa, they exhibit significantly different g(r). Pronounced peaks are observed in the g(r) around Na^+ ions (Figure 3.6a), revealing Na^+ ions are the preferential adsorption sites for all the three adsorbates. From the

simulation snapshots at a low pressure (not shown), we observe that the oxygen atoms of water and alcohols are oriented toward the Na^+ ions. Compared to ethanol, however, water and methanol have a substantially higher peak at a shorter distance r = 2.3 Å. This suggests that ethanol has a weaker interaction with Na^+ ions due to its smaller polarity and bulkier size. With a closer look, we find that methanol appears to have a slightly higher peak than water at r = 2.3 Å as also observed in zeolites.[235] This denotes methanol adsorbs more strongly than water onto Na^+ ions at 10^{-4} kPa. Nevertheless, there is a larger peak for water at a long distance ($r \approx 4.5$ Å) and overall water has a higher extent of adsorption.

Increase in the molecular size of adsorbate affects the accessibility to the free space in the framework. Figure 3.6b shows the g(r) around the carboxylate oxygen (O_2) atoms of the framework. While water has a distinct peak at a short distance, methanol exhibits a lower peak at a relatively longer distance. In marked contrast, no pronounced peak is observed for ethanol. These imply that the adsorbate molecules move away from the framework with increasing molecular size (from water to methanol and then to ethanol). As discussed above, Na^+ ions are the preferential adsorption sites for all the three adsorbates. Therefore, it can be expected that water is adsorbed onto the Na^+ ions at site I more than methanol and ethanol, because site I is closer to the framework compared to site II. With a smaller size, water experiences a less steric hindrance to adsorb at site I near the narrow windows. The shift in the peak position away form the O_2 with increasing adsorbate size is attributed to the adsorption in the open α-cage. Similar phenomenon of alcohol adsorption away from the windows was also observed in NaA zeolite.[235] Figure 3.6c shows the g(r) of adsorbate around In atoms of the framework. A

pronounced peak is seen for water and this reveals, in accordance with Figure 3.6b, water is close to the framework in a highly coordinated fashion with Na^+ ions. Two peaks are observed for methanol, one corresponding to adsorption proximal to the framework and the other to adsorption in the α-cage. For ethanol, a dispersed g(r) is observed which denotes the adsorption is primarily in the α-cage.

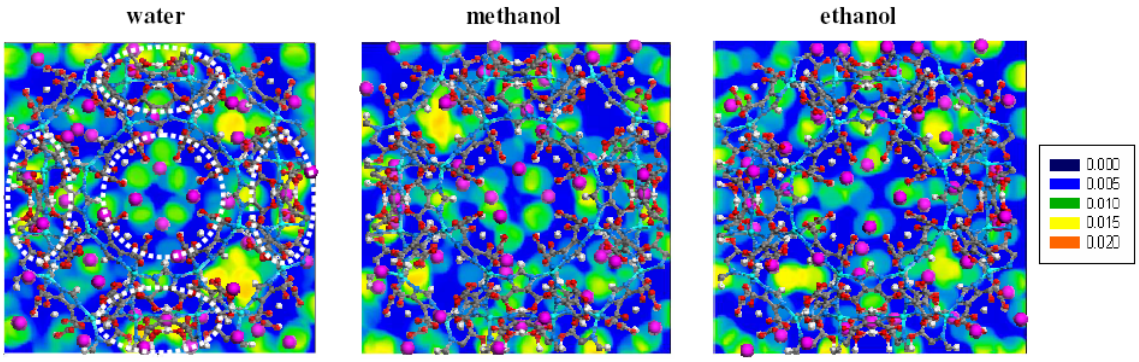

Figure 3.7. Density contours of water, methanol, and ethanol in Na-*rho*-ZMOF at 10^{-4} kPa. The density is based on the number of molecules per Å3. The large pink spheres indicate Na^+ ions. The dotted circles indicate the single-eight membered rings (S8MRs).

Figure 3.7 shows the density contours of water, methanol, and ethanol in Na-*rho*-ZMOF at 10^{-4} kPa. As discussed, adsorption at a low pressure is mainly on the Na^+ ions. It can be see that water is strongly adsorbed at the S8MR near the window region. In contrast, methanol and ethanol are more populated in the α-cage. Though now shown here, adsorption at a moderate pressure is observed to occur near the framework surface. At a high pressure, the open α-cage is filled and Na^+ ions appear to be solvated by adsorbate molecules. Such a three-step adsorption mechanism was previously observed for adsorption in NaX and NaY zeolites.[199] It is also interesting to point out that a few Na^+ ions were observed to shift from site I to site II with increasing pressure of water.

This is attributed to the preferential adsorption of water on the Na^+ ions at site II, which in turn exerts attractive force on the Na^+ ions at site I and facilitates them to redistribute.

3.3.2 Binary mixtures in Na-*rho*-ZMOF

Figure 3.8a and 3.8b show the adsorption isotherms for the equimolar mixtures of water/methanol and water/ethanol, respectively. As observed in pure components, water has a stronger adsorption than methanol and ethanol. In accordance with this, water is also more adsorbed in both mixtures.

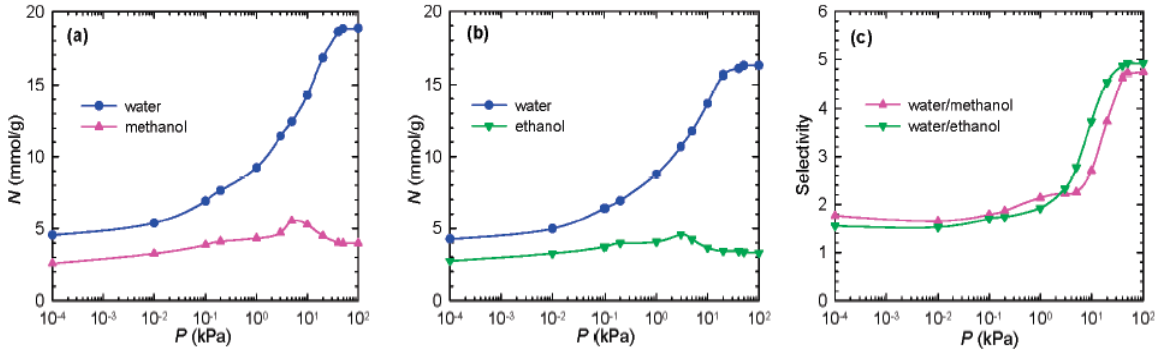

Figure 3.8. Adsorption isotherms for the equimolar mixtures of (a) water/methanol (b) water/ethanol in Na-*rho*-ZMOF. (c) Selectivities.

With increasing pressure, water adsorption becomes more pronounced than alcohols due to the highly associating nature and smaller size of water, which extends the hydrogen bonding network and fills the free space more easily than alcohols. As a consequence of competitive adsorption, adsorbed water replaces alcohols after reaching a certain pressure and subsequently the amount of alcohols adsorbed decreases. The separation factor of a binary mixture is usually quantified by adsorption selectivity $S_{i/j} = (x_i / x_j)(y_j / y_i)$, where x_i and y_i are the mole fractions of component i in adsorbed and bulk phases, respectively. Figure 3.8c shows the selectivities of water over

methanol and ethanol, respectively, as a function of pressure. The selectivities increase with increasing pressure as a result of the preferential adsorption of water at high pressures. The increase of water/alcohol selectivity with increasing pressure, especially at high pressures, was also observed in cation-exchanged zeolites from experiment[236] and simulation.[237] The selectivity of water/methanol and water/ethanol in Na-*rho*-ZMOF ranges from 1.5 at low pressures to 5 at high pressures, which is close the value observed in zeolites.[235,238] Thus the appropriate condition for the separation of water/alcohols in Na-*rho*-ZMOF is at high pressures.

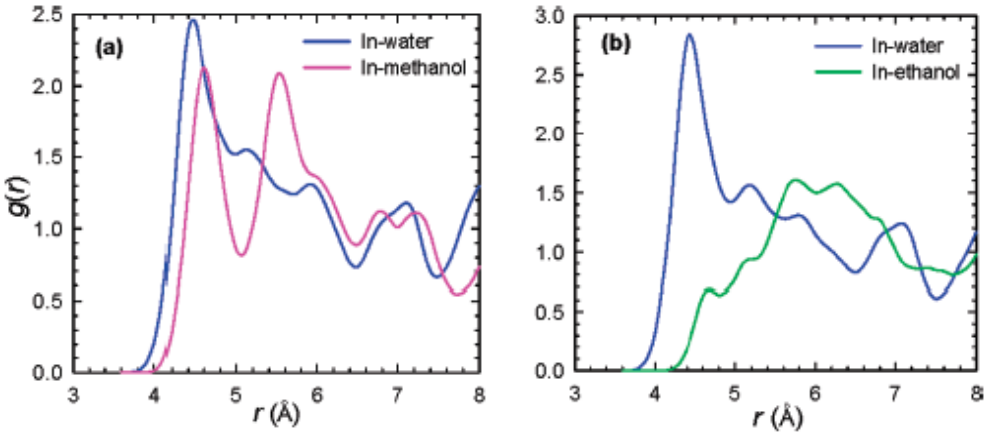

Figure 3.9. Radial distribution functions $g(r)$ of In-adsorbate for the equimolar mixtures of (a) water/methanol (b) water/ethanol in Na-*rho*-ZMOF at 10^{-4} kPa.

Figure 3.9 shows the g(r) of adsorbates around In atoms for water/alcohol mixtures at 10^{-4} kPa. The behavior of g(r) is qualitatively similar to that for pure components in Figure 3.6c. Compared to methanol and ethanol, water adsorbs more closely to the framework. This implies that the mechanism involved in the adsorption of pure components still comes into play in mixture adsorption. Water is adsorbed more closely in the window region, while methanol and ethanol are primarily in the α-cage away from the framework surface due to the steric hindrance. This interesting behavior might be

advantageous to attain kinetic separation of water/alcohol mixtures because the windows are not blocked by alcohols and allow for the easy transport of water across the cages.

3.3.3 Pure components in ZIF-71

Figure 3.10 show the adsorption and desorption isotherms of water, methanol, and ethanol in ZIF-71. The isotherms are of *S*-shaped type V, which signifies the adsorption of weakly interacting adsorbates in a microporous framework. Similar to other ZIF materials,[222-224,239] the preferential adsorption sites in ZIF-71 are organic linkers rather than metal sites. Therefore, the affinity of ZIF-71 is weaker compared to Na-*rho*-ZMOF. The open framework structure in ZIF-71 also contributes to the weak potential field for adsorption. Almost no adsorption is observed for water even at saturation pressure, indicating ZIF-71 cage is hydrophobic. It is energetically unfavorable for water to break hydrogen-bonds in bulk phase and then adsorbed in a hydrophobic environment. At 22 kPa ($P/P^o \approx 7.1$), water exhibits a sharp increase in adsorption and approaches saturation rapidly. This adsorption behavior is attributed to capillary condensation through the nucleation of water molecules and followed by the collapse of water clusters into a liquid state. A hysteresis loop is observed in the adsorption and desorption isotherms between 8 and 22 kPa. Similar behavior was observed for water in hydrophobic zeolites.[240,241] The occurrence of hysteresis is mainly attributed to how easy water can fill and drain the pores. A hysteresis suggests the existence of meta-stable states and local minima in the grand free energy of the system. The states above the upper closure point or below the lower closure point are thermodynamically stable.

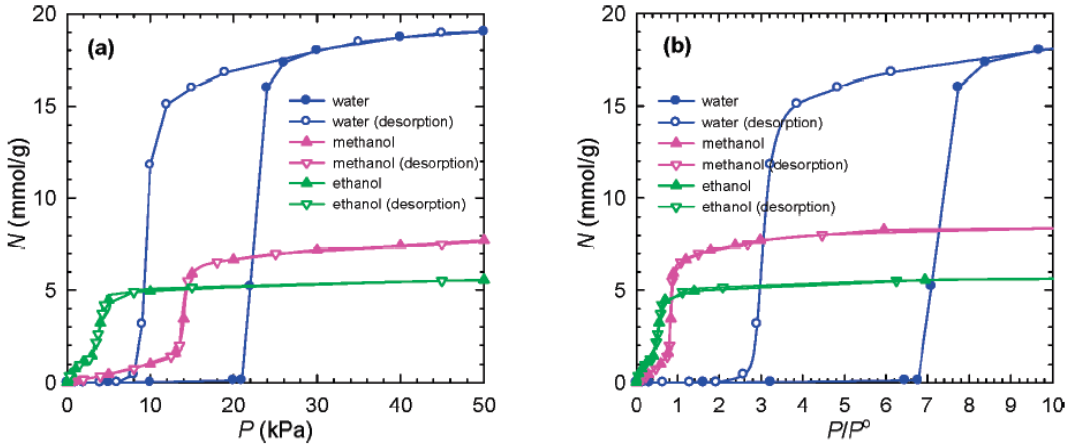

Figure 3.10. Adsorption (filled symbols) and desorption (open symbols) isotherms of water, methanol, and ethanol in ZIF-71 as a function of (a) pressure and (b) reduced pressure. The saturation pressure P^o is 3.1 kPa for water, 16.8 kPa for methanol, and 7.2 kPa for ethanol.

At a low pressure, methanol adsorption in ZIF-71 is weak. Above 14 kPa, however, the adsorption increases sharply as a consequence of continuous pore filling. Initially, the adsorbed methanol molecules form small clusters (seeds), which exert attractions for the later adsorbed molecules and grow into a three-dimensional network filling the cage. Upon comparison, ethanol exhibits a significant amount of adsorption even at a low pressure. With increasing pressure, continuous pore filling also occurs for ethanol. Different from water, the adsorption and desorption of methanol and ethanol in ZIF-71 are completely reversible. In remarkable contrast to the case in Na-*rho*-ZMOF, the extent of adsorption in ZIF-71 at a low pressure increases following the order of water < methanol < ethanol. This is because the hydrophobic ZIF-71 has a stronger affinity for less polar alcohols than water. Alcohols are amphiphilic in nature containing polar hydroxyl and nonpolar alkyl groups. At a high pressure, where the adsorption to a large extent is controlled by entropy effect, the smallest water exhibits the largest saturation capacity, followed by methanol and then ethanol.

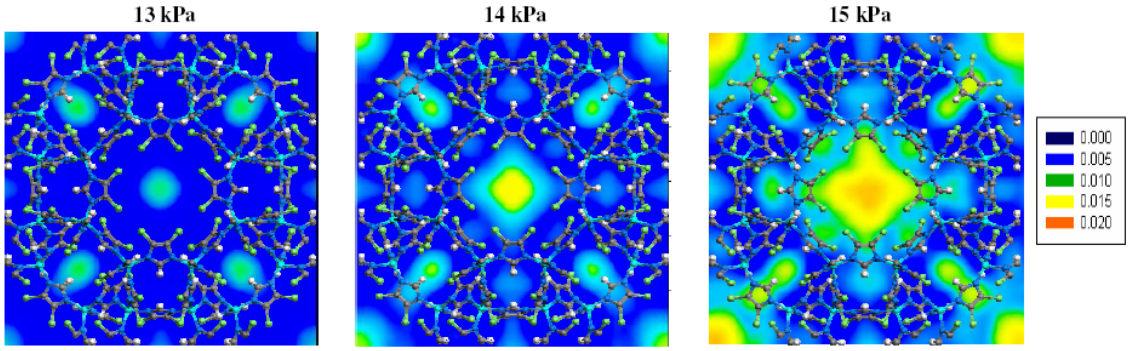

Figure 3.11. Density contours of methanol in ZIF-71 at 13, 14, and 15 kPa, respectively.

Figure 3.11 shows the density contours of methanol in ZIF-71 at 13, 14, and 15 kPa, respectively. It is obviously to see the cluster growth mechanism for methanol adsorption. At 13 kPa, methanol molecules are adsorbed at eight- and six-membered rings and form clusters. The clusters grow with increasing pressure at 14 kPa and fill the cage at 15 kPa. Similar trend is also observed for ethanol and thus not shown here. This type of behavior is usually expected in hydrophobic porous materials.

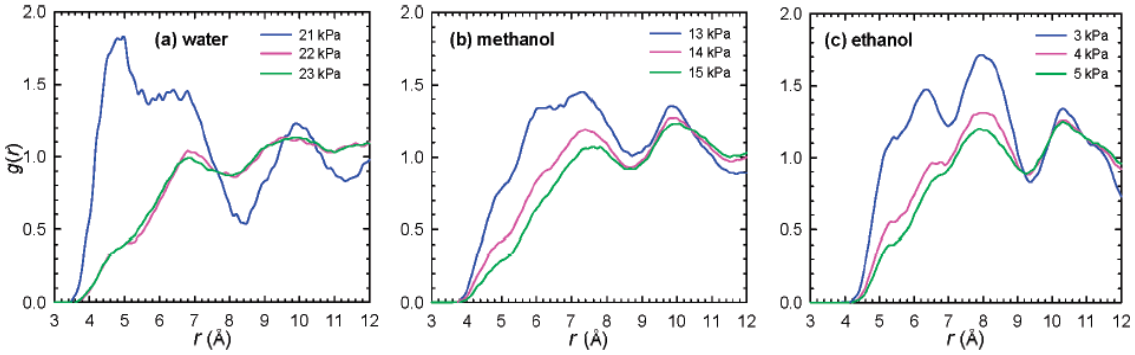

Figure 3.12. Radial distribution functions $g(r)$ of (a) Zn-water (b) Zn-methanol and (c) Zn-ethanol for water, methanol, and ethanol in ZIF-71.

Figure 3.12 shows the g(r) of water, methanol, and ethanol respectively around Zn atoms at pressures near the inflection point. At a pressure slightly below the inflection point, the peak in g(r) corresponds to the clustered molecules near the framework. With a

marginal increase in pressure, the g(*r*) appears to be dispersed representing the occurrence of cage filling. The simulation snapshots (not shown) indicate that the carbon atoms of alcohols are in proximal to the ZIF-71 framework, particularly at a low pressure.

3.3.4 Binary mixtures in ZIF-71

Figures 3.13a and 3.13b show the adsorption isotherms for the equimolar mixtures of water/methanol and water/ethanol, respectively.

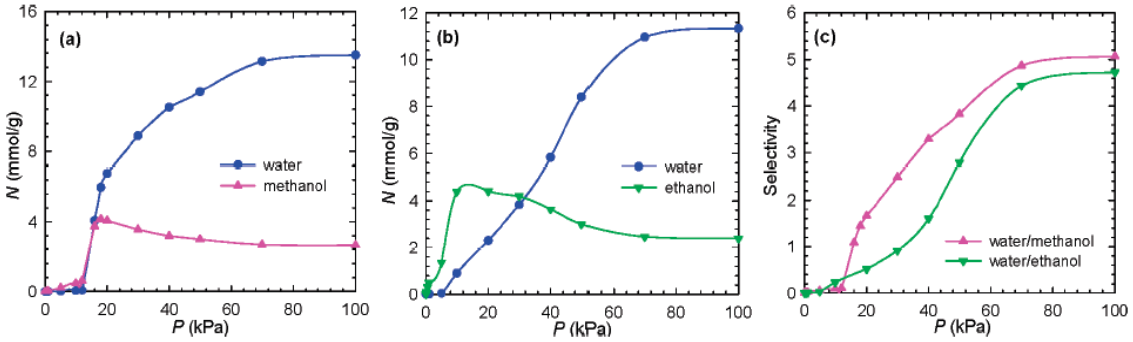

Figure 3.13. Adsorption isotherms for the equimolar mixtures of (a) water/methanol (b) water/ethanol in ZIF-71. (c) Selectivities.

In both mixtures, alcohols are adsorbed more than water at low pressures. Particularly, ethanol has a significant amount of adsorption due to the preferential interactions with the hydrophobic ZIF-71. It is instructive to note that water exhibits an appreciable amount of adsorption in the mixtures even at low pressures. This is different from pure water which has vanishing adsorption below 22 kPa. The reason is that the already adsorbed alcohol molecules induce cooperative attractions for water and cause water adsorption. In addition, the inflection point in the mixture adsorption is observed to shift towards lower pressures. With increasing pressure, water adsorption increases rapidly due to its highly associative nature and small molecular size. Thus, the competitive adsorption, as seen in Na-*rho*-ZMOF, also occurs in ZIF-71. This behavior

was also observed in the adsorption of water/methanol mixture in hydrophobic carbon pores.[242,243] Figure 3.13c shows the selectivities of water over methanol and ethanol, respectively. At a low pressure, the selectivities are substantially less than 1 because alcohols are exceptionally selectively adsorbed relative to water. At a high pressure, however, water is preferentially adsorbed and the selectivities increase up to 5. This implies that the optimal condition for the separation of water/alcohols in ZIF-71 is at a low or high pressure, but not at a moderate pressure.

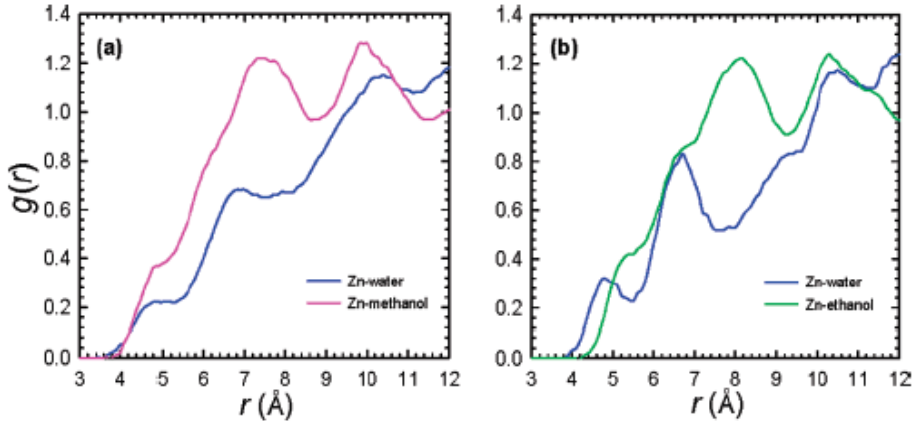

Figure 3.14. Radial distribution functions $g(r)$ of Zn-adsorbate for the equimolar mixtures of (a) water/methanol at 16 kPa (b) water/ethanol at 10 kPa in ZIF-71.

The mechanism for binary-mixture adsorption could be further elucidated from the structural information. Figure 3.14 shows the g(r) of adsorbates around Zn atoms of ZIF-71. Methanol and ethanol exhibit more pronounced peaks than water at two positions. This indicates that alcohols interact more strongly than water with the ZIF-71 framework; additionally, alcohols are located at two favorable sites, one at the 8-membered ring and the other at 6-membered ring as illustrated in Figure 3.11. The relatively smaller value of g(r) for water implies the co-adsorption between alcohols and water, which is induced by the initially adsorbed alcohols.

Additional simulations were performed to investigate the influence of the framework charges on adsorption. Figure 3.15 shows the adsorption for the equimolar mixture of water/ethanol in Na-*rho*-ZMOF and ZIF-71 with and without the framework charges. The framework charges have a substantial effect on the adsorption in hydrophilic Na-*rho*-ZMOF, but a small effect in hydrophobic ZIF-71. Intriguingly, the isotherms in Na-*rho*-ZMOF without the framework charges behave like in ZIF-71. This is because the neutral structure of Na-*rho*-ZMOF tends to be hydrophobic.

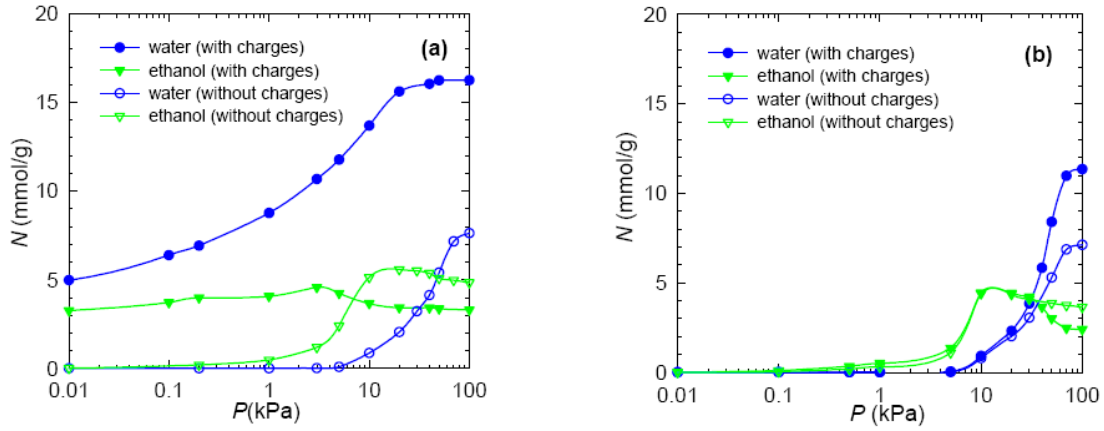

Figure 3.15. Adsorption isotherms for the equimolar mixture of water/ethanol in (a) Na-*rho*-ZMOF and (b) ZIF-71 with and without the framework charges.

3.4 Conclusions

The adsorption of water, methanol, and ethanol in Na-*rho*-ZMOF and ZIF-71 has been investigated by molecular simulation. In hydrophilic Na-*rho*-ZMOF, the three adsorbates exhibit type-I isotherms. Water is preferentially adsorbed than alcohols and the adsorption capacity follows the order of water > methanol > ethanol. The adsorption in Na-*rho*-ZMOF shows a three-step adsorption mechanism. At a low pressure, Na^+ ions are the preferential adsorption sites. Water experiences a less steric hindrance to adsorb at site I near the narrow windows. With increasing molecule size, the adsorbate prefers to

stay in the large α-cage. Thus, the accessibility to the free space in framework is influenced by the size of adsorbate. At a moderate pressure, adsorption occurs near the framework surface; and at a high pressure, the α-cage is largely filled. In water/methanol and water/ethanol mixtures, the competitive adsorption occurs. Water adsorption increases continuously with pressure, whereas alcohol adsorption increases up to a certain pressure and then decreases. The selectivities of water/alcohol in Na-*rho*-ZMOF are in the range from 1.5 at a low pressure to 5 at a high pressure.

Because of the preferential adsorption sites on organic linkers and the widely open structure, ZIF-71 possesses relatively weak affinity for adsorbates. The adsorption isotherms in hydrophobic ZIF-71 are of type V. Water has negligible adsorption even when pressure is up to 22 kPa. A hysteresis loop is observed for water as a result of capillary condensation and evaporation. The cluster-growth mechanism is observed for the adsorption of methanol and ethanol, followed by continuous pore filling with increasing pressure. The adsorption in ZIF-71 at a low pressure increases in the order of water < methanol < ethanol. At a high pressure, adsorption is primarily determined by entropy effect; consequently, water has the largest saturation capacity, followed by methanol and ethanol. In water/methanol and water/ethanol mixtures, alcohols particularly ethanol are more selectively adsorbed than water at a low pressure. At a high pressure, water adsorption increases rapidly. The selectivities are less than 1 but reversed with increasing pressure.

This work reveals that the adsorption mechanisms of water and alcohols in hydrophilic Na-*rho*-ZMOF and hydrophobic ZIF-71 are substantially different, though both MOFs have the identical *rho*-type topology and similar pore size. The operating

conditions for water/alcohol separation vary in the two MOFs, being at a high pressure in Na-*rho*-ZMOF and at a low or high pressure in ZIF-71. Although no experimental data are currently available for comparison with simulation results, the quantitative understanding at a molecular level is useful for the further development of new MOFs toward high-efficacy dehydration or purification of alcohol-based biofuels.

Chapter 4

Biofuel Purification in MOFs

4.1 Introduction

Biofuel is a renewable energy resource and an alternative to the conventional petroleum based fossil-fuels.[244,245] The most common biofuel is ethanol and there has been considerable interest to produce water-free fuel-grade ethanol, as water adversely affects the performance.[246] For the separation of water/ethanol in biofuel, membrane technology is considered as one of feasible methods because of high selectivity and low energy cost.[247] Two typical processes are usually applied in membrane separation, namely, pervaporation (PV) with a liquid feed or vapor permeation (VP) with a vapor feed. The separation factor is largely governed by the adsorption and diffusion properties of water and ethanol in the membrane.

A wide variety of membrane materials ranging from polymers, carbons to inorganic zeolites have been studied for the separation of water/ethanol mixtures. With an appropriately chosen membrane, the separation process can be carried out to enrich ethanol in either feed or permeate side. For example, if ethanol concentration is low, a hydrophobic membrane (e.g. silicalite) can be used for the enrichment of ethanol in the permeate side. With a high ethanol concentration, however, the feed side is enriched by ethanol using a hydrophilic membrane (e.g. NaA zeolite) permselective for water. Molecular sieving zeolites are thermally and chemically stable, but fragile and not easily processable. Polymeric membranes can be fabricated in a relatively easy way, whereas their separation performance and mechanical strength need to be improved. It has been

recognized that the new generation membranes preferably possess the high stability of inorganic building blocks and the tunable functionality of organic moieties.[248]

In the past decade, MOFs have emerged as a new class of hybrid nanoporous materials.[31] Composed of metal-oxide clusters and organic linkers, MOFs have extremely large surface area (up to 6000 m^2/g) and high porosity (up to 90%) ever recorded for crystalline materials. In contrast to the spherical or slit-shaped pores usually present in zeolites, MOFs possess well-structured pores such as squared, rectangular, triangular and window-connected. More importantly, the judicious choice of controllable organic linkers and the variation of metal oxides allow the pore sizes, volumes and functionalities of MOFs to be tailored in a rational way. MOFs are considered as versatile materials for storage, separation, catalysis, biomedical, and other potential applications.[25] Most experimental and theoretical studies of MOFs to date have focused on gas storage and separation.[249-251] Only a few studies were reported to examine the separation of liquid mixtures in MOFs.[87] Ahmad et al. evaluated the potential use of microporous MOFs as the stationary phase in a liquid chromatographic separation of organic compounds.[252] Chen et al. synthesized a MOF with pores of 2.8 × 3.6 Å for the selective adsorption of water/methanol liquid mixtures.[217] Alaerts et al. examined the selective adsorption of xylene isomers and ethylbenzene in MIL-47, and also tested three MOFs with similar pore window diameters for the separation of olefins, alkylnaphthalenes and dichlorobenzenes.[253] We performed molecular simulations attempting to understand the adsorption mechanisms of water and alcohols in zeolitic MOFs.[227,254]

For the practical applications in aqueous media or organic solvents, chemically stable MOFs are desired. However, many common MOFs especially Zn- or Cu-based cannot

meet this requirement. The design of highly stable MOFs resistant to water and organic solvents is an active research area. Recently, several azolate–based MOFs have been synthesized with good thermal and chemical stability, which is attributed to the strong interactions between metals and azolate linkers relative to carboxylic linkers. For example, zeolite-like MOFs (ZMOFs)[193,218] and zeolitic-imidazolate frameworks (ZIFs)[219,220] demonstrate exceptional stability and receive considerable interest. In a recent report, a MOF named $Zn_4O(bdc)(bpz)_2$ (bdc = benzenedicarboxylate, bpz = tetramethyl bipyrazolate) was reported with structure similar to prototype MOF-5. This hydrophobic MOF consists of methyl-decorated pores and is stable in water and common organic solvents.[78]

For the successful implementation of a MOF in liquid-phase separation, a clear fundamental understanding of separation mechanism is indispensable. This is particularly important as the number of stable MOFs is growing rapidly. In this work, biofuel purification or specifically the separation of water/ethanol mixtures in MOFs is investigated using molecular simulation. Both PV and VP separation processes are examined in two typical MOFs, one is hydrophilic Na-*rho*-ZMOF and the other is hydrophobic $Zn_4O(bdc)(bpz)_2$. In Section 4.2, the molecular models and simulation methods are briefly described. In Section 4.3, the adsorption properties of water/ethanol mixtures in Na-*rho*-ZMOF[218] and $Zn_4O(bdc)(bpz)_2$[78] are first presented, particularly the adsorption isotherms and selectivities. Then, the diffusivities and diffusion selectivities are discussed. Finally, on the basis of adsorption and diffusion selectivities, the permselectivities are predicted. By this systematic study, we aim to seek microscopic

guideline on which MOF is better suited for PV or VP separation of water/ethanol mixtures.

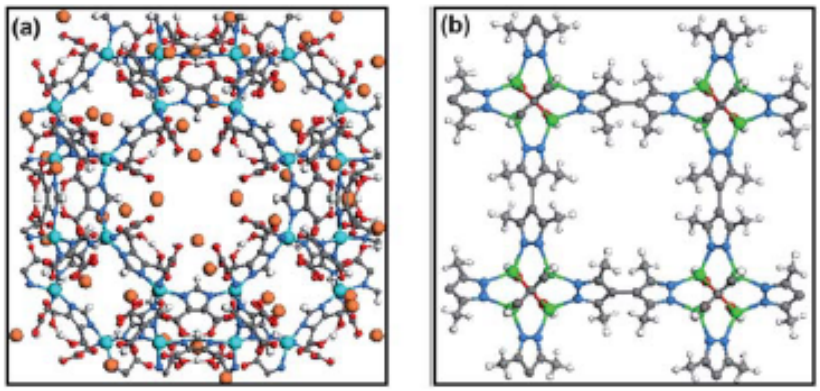

Figure 4.1. Atomic structures of (a) Na-*rho*-ZMOF and (b) $Zn_4O(bdc)(bpz)_2$. Color code: In, cyan; N, blue; Zn, green; C, grey; O, red; H, white; Na^+ ions, orange.

4.2 Models and Methods

Figures 4.1a and 4.1b show the atomic structures of Na-*rho*-ZMOF and $Zn_4O(bdc)(bpz)_2$, respectively. In Section 2.2, *rho*-ZMOF model has been described in detail. $Zn_4O(bdc)(bpz)_2$ possesses a highly porous crystal structure analogous to MOF-5. The framework is constructed by the assembly of tetrahedral Zn_4O with mixed-ligands 1,4-benezenedicarboxylate (bdc) and 3,3',5,5'-tetramethyl-4,4'-bipyrazolate (bpz). Each tetrahedral Zn_4O is edge-bridged by four pyrazolate and two carboxylate groups resulting in an octahedral $Zn_4O(O_2C\text{-})_2(NN\text{-})_4$ building unit. All the Zn_4O clusters are connected by bpz linkers on the (001) plane and these layers are further pillared along the (001) plane to form a porous network. The space group of $Zn_4O(bdc)(bpz)_2$ belongs to $P4_2/mcm$ with lattice constants of a = 11.5228 Å and c = 25.7692 Å. Its atomic structure in Figure 4.1b is viewed on the (001) plane and the bdc linkers are invisible. The structure contains cube-like cavities connected by windows of 4.9 × 6.8 $Å^2$ along the (100, 010) plane and

5.7 × 5.7 Å^2 along the (001) plane. The methyl groups of bpz ligands contribute to the hydrophobic feature of the cavities.[78]

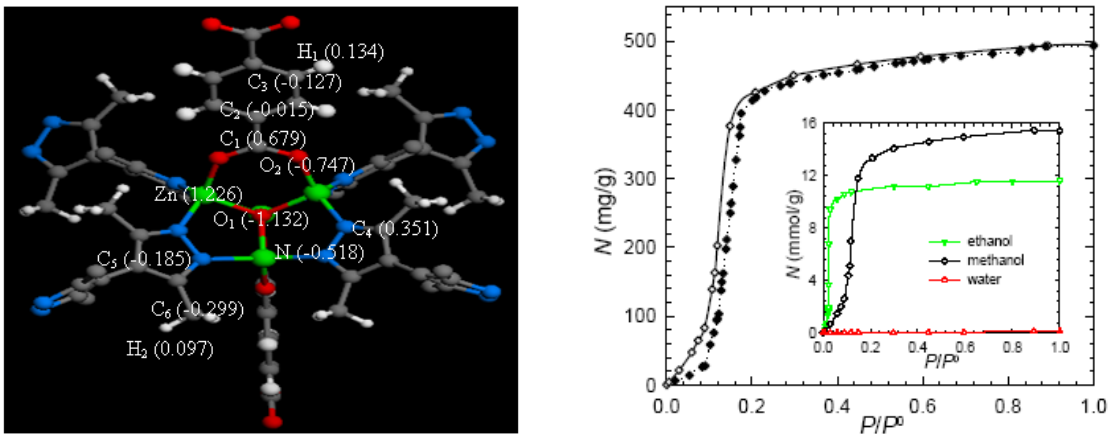

Figure 4.2. (a) Atomic charges in the fragmental clusters of $Zn_4O(bdc)(bpz)_2$. (b) Adsorption isotherms of methanol in $Zn_4O(bdc)(bpz)_2$ at 298 K. The open diamonds are the simulation results of this work, and the filled diamonds are experimental data

The atomic charges on the framework atoms of $Zn_4O(bdc)(bpz)_2$ were calculated by density-functional theory (DFT) on a fragmental cluster shown in Figure 4.2a. The *rho*-ZMOF and water/ethanol were modeled with the same force fields as described in Chapters 2 and 3, thus the details are not provided here. We note that the adsorption isotherm of methanol in $Zn_4O(bdc)(bpz)_2$ is experimentally available.[78] To validate the model and force field used, we simulated the adsorption of methanol in $Zn_4O(bdc)(bpz)_2$ and compared with the experimental data. As shown in Figure 4.2b, the simulated and experimental adsorption isotherms of methanol are in good agreement. In addition, ethanol has a greater extent of adsorption than methanol at a low pressure and the adsorption of water is vanishingly small, because $Zn_4O(bdc)(bpz)_2$ is hydrophobic.

As mentioned earlier, two processes PV and VP are considered for the separation of water/ethanol mixtures in this study. The feed in PV is a liquid phase at 50 °C and 1 bar,

and the feed in VP is a vapor phase at 100 °C and 1 bar. The fugacity of component *i* at the PV condition is estimated by

$$f_i = P_i^{sat}\phi_i^{sat}x_i^{feed}\gamma_i \exp\left(\frac{\overline{V_i}(P-P_i^{sat})}{RT}\right) \quad (4.1)$$

where P_i^{sat} is saturation pressure, ϕ_i^{sat} is fugacity coefficient, x_i^{feed} is mole fraction in liquid feed phase, γ_i is activity coefficient, $\overline{V_i}$ is partial molar volume, P is operating pressure (1 bar). The saturation pressure was calculated by the Antonie equation, and the activity coefficients was evaluated by the Non-Random Two Liquid (NRTL) excess Gibbs energy model with the binary parameters of water/ethanol from the literature.[255] At the PV condition applied, the fugacity coefficient and the Poynting factor were approximately equal to unity.

At the VP condition, the fugacity of component *i* is calculated by

$$f_i = P\,y_i^{feed}\phi_i^{feed} \quad (4.2)$$

where y_i^{feed} is mole fraction in vapor feed phase, and ϕ_i^{feed} is fugacity coefficient and assumed to be unity.

At both PV and VP conditions, grand canonical Monte Carlo (GCMC) simulations were conducted to investigate the adsorption of water/ethanol mixtures in Na-*rho*-ZMOF and $Zn_4O(bdc)(bpz)_2$. The fugacities required in the GCMC simulations were calculated by Eq. (4.1) and (4.2) for the PV and VP conditions, respectively. The simulation box contained one unit cell of Na-*rho*-ZMOF or nine (3×3×1) unit cells of $Zn_4O(bdc)(bpz)_2$, with the periodic boundary conditions exerted in three dimensions. The frameworks were assumed to be rigid, and the unit cell was divided into fine grids with the potential energies pre-tabulated and subsequently used by interpolation during simulation. In such

a treatment, the simulation was accelerated by two orders of magnitude. Six different types of trial moves were randomly attempted in the GCMC simulations, namely, displacement, rotation, and partial regrowth at a neighboring position, complete regrowth at a new position, swap between reservoir including creation and deletion with equal probability, and the exchange of molecular identity. The nonframework Na^+ ions in Na-*rho*-ZMOF were allowed to move upon the adsorption of water/ethanol.

The diffusion of water/ethanol mixtures was examined by molecular dynamics (MD) simulations with GROMACS package v.4.0.[256] The initial configurations for MD simulations were taken from the final configurations of above GCMC simulations. The Nosé-Hoover method was used to maintain temperature with a relaxation time of 0.1 ps. The particle-mesh-Ewald (PME) technique was applied to calculate the Coulombic interactions with a grid spacing of 0.12 and a fourth-order interpolation. The bond lengths in ethanol molecules were constrained using a linear constraint solver (LINCS).[257] For each system, 2 ns equilibration and 10 ns production MD runs were conducted. The potential and kinetic energies were monitored to ensure equilibration. The trajectory in the production run was saved every 1 ps for subsequent analysis.

4.3 Results and Discussion

First, the adsorption isotherms and selectivities for water/ethanol mixtures are presented at both PV and VP conditions in Na-*rho*-ZMOF and $Zn_4O(bdc)(bpz)_2$, respectively. Then, the diffusivities and diffusion selectivities are reported. Finally, the permselectivities are discussed on the basis of the adsorption and diffusion selectivities.

4.3.1 Adsorption in Na-*rho*-ZMOF

For a binary mixture, the adsorption-based separation factor is usually quantified by adsorption selectivity

$$S_{\mathrm{ad}\,(i/j)} = (N_i / N_j)(z_j / z_i) \tag{4.3}$$

where N_i is the adsorption amount of component i, and z_i is the feed composition.

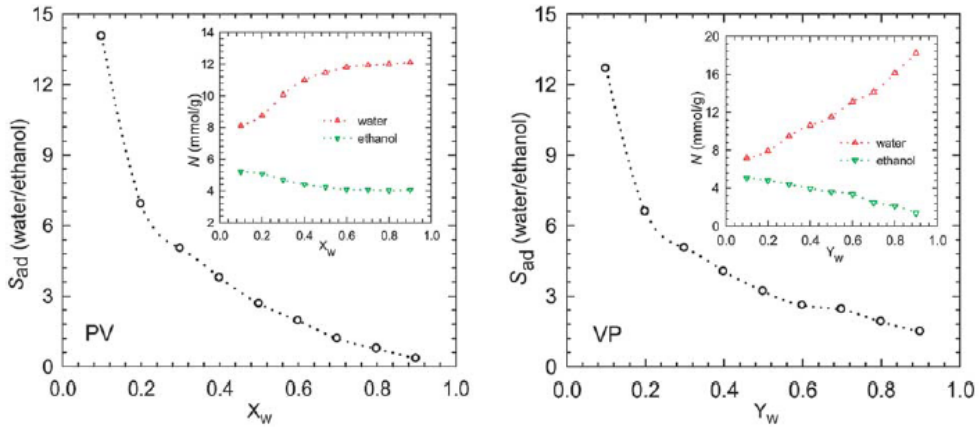

Figure 4.3. Adsorption selectivities for water/ethanol mixtures in Na-*rho*-ZMOF at PV and VP conditions. The insets are adsorption isotherms.

Figure 4.3 shows the adsorption selectivities for water/ethanol mixtures in Na-*rho*-ZMOF at PV and VP conditions versus the feed composition of water. Our previous study suggests that water and alcohols are adsorbed in Na-*rho*-ZMOF with a three-step adsorption mechanism.[227] At a low loading, adsorption occurs preferentially near the nonframework Na^+ ions; with increasing loading, a monolayer is formed on the framework surface and finally the large α-cage is filled. As seen from the adsorption isotherms in the insets, water competitively adsorbs over ethanol at all the feed compositions. This is attributed to the stronger interaction of highly polar water with the nonframework Na^+ ions and ionic framework. The bulky nonpolar alkyl groups cause

ethanol to be less competitive for ionic adsorption sites in the framework as electrostatic interactions play a dominating role. In addition, it should be noted that at the conditions in the current study for PV and VP, the adsorption is near saturation and the packing effect is important to determine adsorption amount. Water is smaller than ethanol and thus packs more efficiently, resulting in higher adsorption.

Interestingly, at a given water composition, the selectivity at PV and VP conditions is approximately same. With increasing water composition, the number of adsorbed water molecules increases and there are fewer favorable adsorption sites for water; consequently, the adsorption selectivity of water over ethanol decreases. The selectivity has a higher value at a lower feed composition of water, suggesting that Na-*rho*-ZMOF is more suitable for the adsorption-based separation of water/ethanol mixtures which are rich in ethanol. A similar dependence of selectivity on water composition was also observed in zeolites (MFI, MOR, CFI and DON).[258] The maximum adsorption selectivity over the composition range studied here is approximately 14, which is close to that in NaA zeolite for water/ethanol separation.[238]

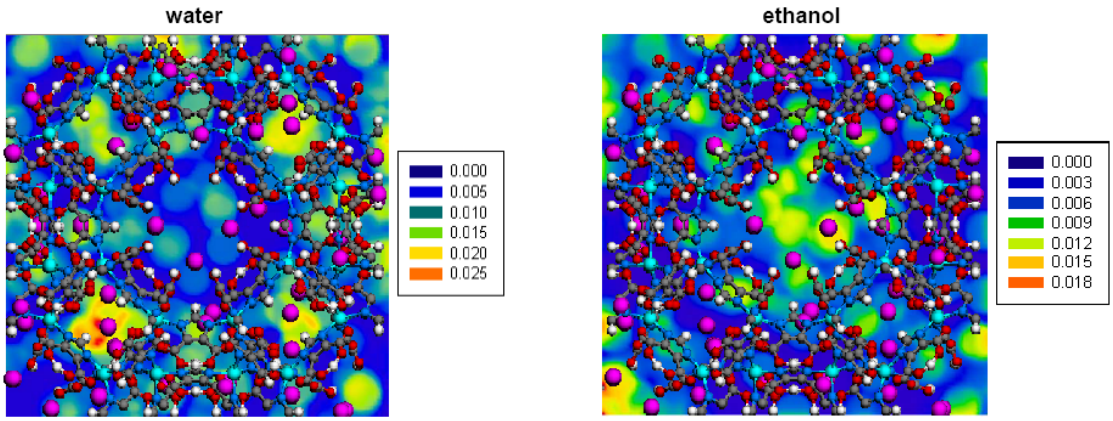

Figure 4.4. Density contours of water and ethanol for water/ethanol mixture (10:90) at PV condition in Na-*rho*-ZMOF.

Figure 4.4 illustrates the density contours of water and ethanol for water/ethanol mixture (10:90 in mole fraction) at PV condition in Na-*rho*-ZMOF. Water is observed to preferentially locate near the Na^+ cations and ionic framework, as attributed to the strong electrostatic interactions. In particular, the density of water near the six-member rings is higher. However, ethanol is a weaker adsorbate compared to water and thus primarily localized in the open α-cages, as will be further discussed below.

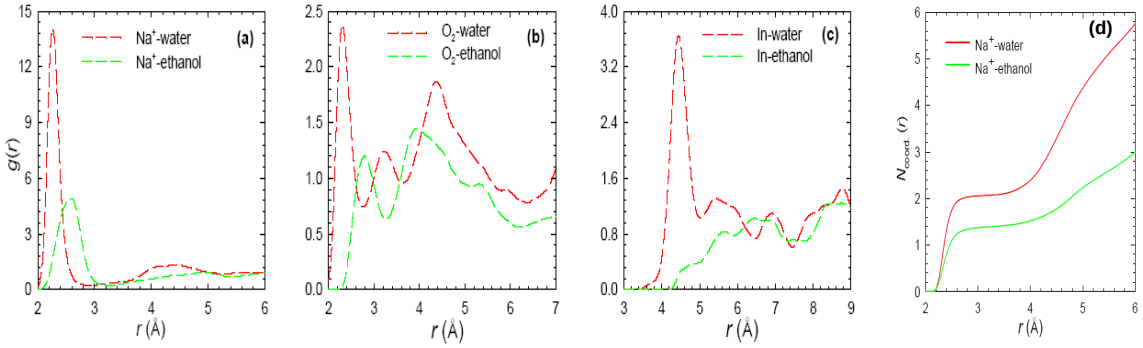

Figure 4.5. Radial distribution functions of (a) Na^+-adsorbates, (b) O_2-adsorbates, and (c) In-adsorbates. (d) Coordination numbers of water and ethanol around Na^+ ions for water/ethanol mixture (10:90) at PV condition in Na-*rho*-ZMOF.

To elucidate the structures of adsorbates and thus provide molecular insight into the adsorption mechanism, radial distribution functions g(*r*) were calculated. Figure 4.5 shows g(*r*) for the centers-of-mass of adsorbates around Na^+ ions, carboxylic oxygen (O_2), and In atoms of the framework for the adsorption of water/ethanol mixture (10:90) at PV condition. It should be noted that qualitatively similar profiles of *g*(*r*) are observed at other feed compositions. In Figure 4.5a for g(*r*) around Na^+ ions, water exhibits a pronounced peak at 2.3 Å that is much higher than the peak of ethanol. This is because water is smaller in size and more associative. An increase of adsorbate size affects the accessibility to the free space in the framework. As shown in Figure 4.5b for g(*r*) around the framework O_2 atoms, water exhibits a distinct peak compared to ethanol. This is

attributed to the greater steric hindrance of bulkier ethanol compared to water; consequently, fewer ethanol molecules are located in the window region, which also results in less coordination of ethanol around Na^+ ions in this region. From the g(*r*) of adsorbates around In atoms in Figure 4.5c, a pronounced peak is observed for water and this reveals, in accordance with Figures 4.5a and 4.5b, water is close to the framework in a highly coordinated fashion with the Na^+ ions. For ethanol, however, a dispersed g(*r*) is observed which denotes the adsorption is primarily in the *α*-cages. Compared to ethanol, water adsorbs more closely to the framework, similar to the mechanism involved in the adsorption of pure water and ethanol.[227] As discussed in our previous study, water in Na-*rho*-ZMOF is adsorbed proximately in the window region, while ethanol is primarily in the *α*-cages away from the framework surface due to the steric hindrance.[227] This interesting behavior might be advantageous to attain kinetic separation of water/ethanol mixtures because the windows are not blocked by ethanol and allow for the easy transport of water across the cages.

To further elaborate, the coordination numbers of water and ethanol surrounding Na^+ ions were calculated respectively by

$$N_{\text{cood.}}(r) = \rho_{\text{adsorbate}} \int_0^r g_{\text{Na}^+-\text{adsorbate}}(r') 4\pi r'^2 \, \mathrm{d}r' \tag{4.4}$$

where $\rho_{\text{adsorbate}}$ is the average density of adsorbate. As shown in Figure 4.5d, water has a larger coordination number than ethanol at any given distance *r*. This simply reveals that more water molecules surround Na^+ ions than ethanol.

The g(*r*) in Figure 4.5 are based on the centers-of-mass of adsorbates. Instead, Figure 4.6 shows the g(*r*) of Na^+-OW (OH), O_2-OW (OH), and In-OW (OH) for water/ethanol mixture (10:90) at PV condition in Na-*rho*-ZMOF. The OW and OH are the oxygen

atoms in water and ethanol, respectively. Because of highly polar nature, OW and OH exhibit a comparable peak around Na^+ ions, and also a similar peak around the framework O_2 atoms. As discussed above, however, the g(r) around In atoms and the overall g(r) of whole molecules in Figure 4.5 are different between water and ethanol.

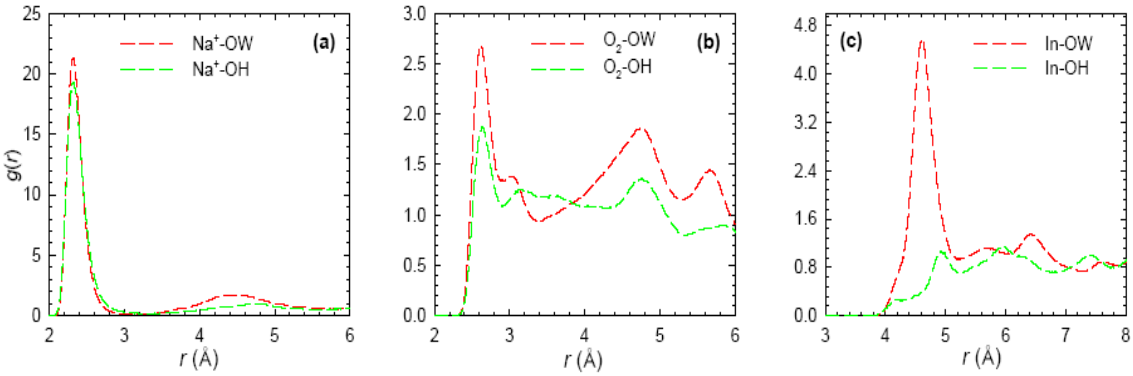

Figure 4.6. Radial distribution functions of (a) Na^+-OW (OH), (b) O_2-OW (OH), and (c) In-OW (OH) for water/ethanol mixture (10:90) at PV condition in Na-*rho*-ZMOF. OW and OH are the oxygen atoms in water and ethanol, respectively.

To examine the structural information between adsorbates, Figure 4.7a shows the g(r) of water-ethanol, water-water, and ethanol-ethanol for the adsorption of water/ethanol equimolar mixture at PV condition in Na-*rho*-ZMOF. A pronounced peak is observed at 1.8 Å in all three curves suggesting the formation of hydrogen bonds among the adsorbate molecules. The peak in g(r) of water-ethanol appears to be higher than those of water-water and ethanol-ethanol. This implies the hydrogen bonding is stronger in water-ethanol compared to water-water and ethanol-ethanol, as observed by Krishna and van Baten in the adsorption of water/alcohol mixtures in zeolites.[154,259] Figures 4.7b and c show the g(r) of water-water and ethanol-ethanol, respectively, at PV and VP conditions with various feed compositions of water. With increasing water composition, the peak in g(r) for water-ethanol increases at both PV and VP conditions, which denotes the

increasingly stronger hydrogen bonding between water and ethanol. A similar trend of increase in hydrogen bonding with increasing water concentration was also seen for water/ethanol mixtures in NaA zeolite.[260]

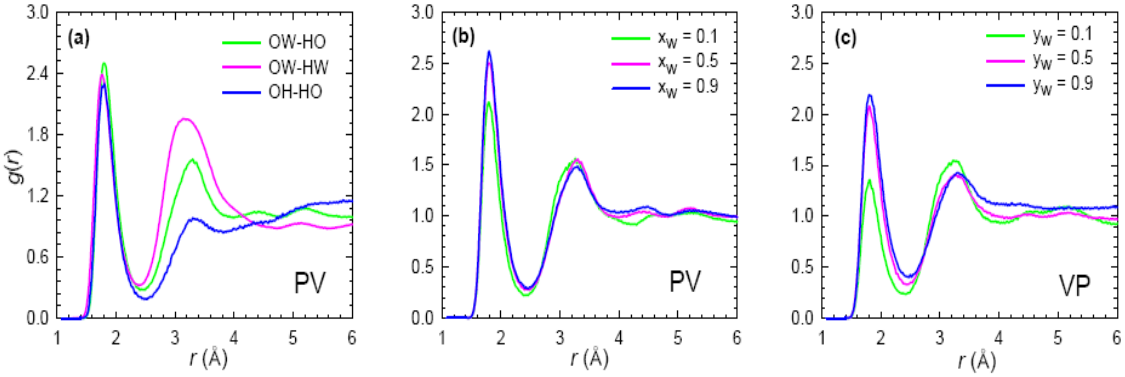

Figure 4.7. Radial distribution functions of (a) O_{water}-$H_{ethanol}$, O_{water}-H_{water} and $O_{ethanol}$-$H_{ethanol}$ for water/ethanol equimolar mixture at PV condition. (b) O_{water}-$H_{ethanol}$ at PV condition and (c) O_{water}-$H_{ethanol}$ at VP condition with various feed compositions in Na-*rho*-ZMOF.

4.3.2 Adsorption in $Zn_4O(bdc)(bpz)_2$

Figure 4.8 shows the adsorption selectivities and isotherms for ethanol/water mixtures in $Zn_4O(bdc)(bpz)_2$ at PV and VP conditions. The preferential adsorption of ethanol over water at all the feed compositions is clearly visible. This is attributed to the stronger interaction of ethanol with the framework, especially the methyl groups on the pore surface which induce hydrophobicity. With increasing ethanol composition in the feed, the adsorption selectivity of ethanol over water decreases at both PV and VP conditions. This is because the number of adsorption sites favorable for ethanol in hydrophobic $Zn_4O(bdc)(bpz)_2$ decreases when more ethanol is adsorbed. Thus the selectivity has a higher value at a lower composition of ethanol and $Zn_4O(bdc)(bpz)_2$ is more preferable to extract a small amount of ethanol for the adsorption-based separation of ethanol/water mixtures. The maximum adsorption selectivities over the composition range covered in

this study are about 85 and 20 at PV and VP conditions, respectively, which are substantially higher than that in silicalite.[261]

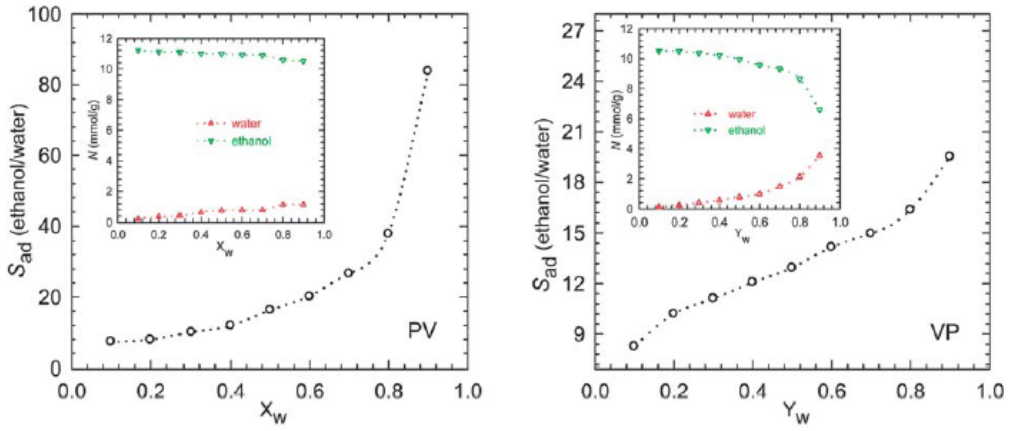

Figure 4.8. Adsorption selectivities for ethanol/water mixtures in $Zn_4O(bdc)(bpz)_2$ at PV and VP conditions. The insets are adsorption isotherms.

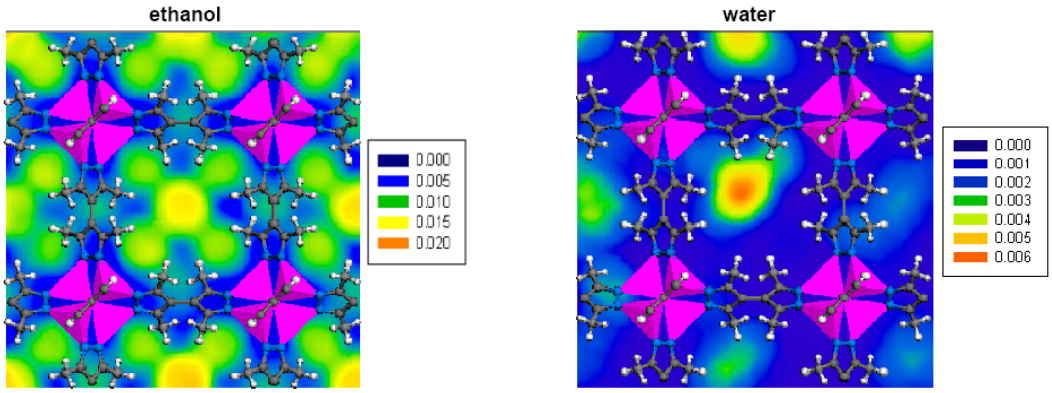

Figure 4.9. Density contours of ethanol and water for ethanol/water mixture (10:90) at PV condition in $Zn_4O(bdc)(bpz)_2$.

Figure 4.9 illustrates the density contours of ethanol and water for ethanol/water mixture (10:90) at PV condition in $Zn_4O(bdc)(bpz)_2$. We should note that the density scales for water and ethanol in Figures 4.4 and 4.9 are not the same and the colors do not have the same quantitative meaning. Consistent with the g(*r*) profiles discussed below,

Figure 4.9 shows ethanol is distributed near the Zn_4O clusters and organic linkers, in addition to the central cavities. Because of the hydrophobic nature of the framework, water is weakly adsorbed and largely located in the central cavities away from the framework surface.

The adsorption mechanism in $Zn_4O(bdc)(bpz)_2$ is further elaborated from the radial distribution functions $g(r)$ for ethanol/water mixture (10:90 in mole fraction) at PV condition. Figure 4.10a shows the $g(r)$ of adsorbates around the framework Zn atoms. While a pronounced shoulder is seen for ethanol at 3.8 ~ 5.5 Å near the framework, there exists a peak for water at 8.5 Å representing the presence of water in the central cavities of $Zn_4O(bdc)(bpz)_2$. Figure 4.10b shows the $g(r)$ around the carbon atoms (C_6) of the methyl groups in bpz linkers. Compared to water, ethanol has a stronger peak around the C_6 atoms as attributed to the hydrophobic nature of the methyl groups. Figure 4.10c shows the $g(r)$ around the carbon atoms (C_3) of the benzene rings in bdc linkers, which is largely similar to the profiles around the C_6 atoms, particularly for ethanol. Nevertheless, a peak is observed for water at a long distance due to the presence of water in the central cavities away from the framework surface.

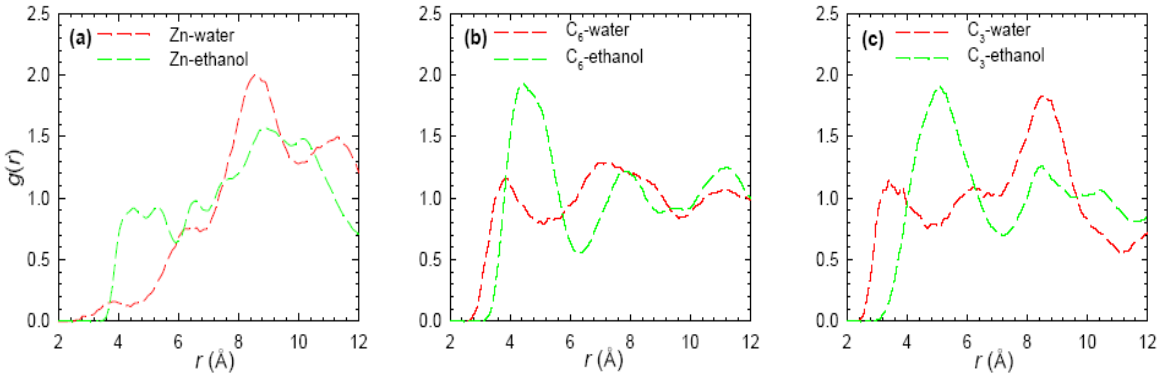

Figure 4.10. Radial distribution functions of (a) Zn-adsorbates, (b) C_6-adsorbates, and (c) C_3-adsorbates for ethanol/water mixture (10:90) at PV condition in $Zn_4O(bdc)(bpz)_2$.

As shown in Figure 4.11, hydrogen bonding is also observed between adsorbates upon adsorption in $Zn_4O(bdc)(bpz)_2$. Compared to Figure 4.7, the peak values of g(*r*) here are substantially larger, indicating that the adsorbate-adsorbate interactions are more favorable in hydrophobic $Zn_4O(bdc)(bpz)_2$ than in hydrophilic Na-*rho*-ZMOF. In other words, water and ethanol tend to form clusters in $Zn_4O(bdc)(bpz)_2$. It is also observed that the hydrogen bonding of water-ethanol is stronger than water-water and ethanol-ethanol. Furthermore, with increasing ethanol composition in the feed, the peak of g(*r*) between water and ethanol increases at both PV and VP conditions, which denotes the enhanced hydrogen bonding. A similar effect on hydrogen bonding was reported upon increasing ethanol concentration in ethanol-rich mixtures.[262]

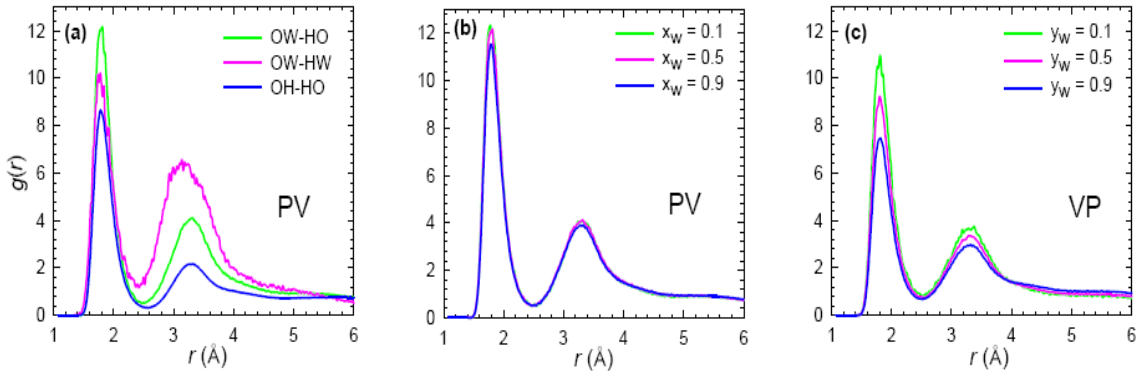

Figure 4.11. Radial distribution functions of (a) O_{water}-$H_{ethanol}$, O_{water}-H_{water} and $O_{ethanol}$-$H_{ethanol}$ for water/ethanol equimolar mixture at PV condition. (b) O_{water}-$H_{ethanol}$ at PV condition and (c) O_{water}-$H_{ethanol}$ at VP condition with various feed compositions in $Zn_4O(bdc)(bpz)_2$.

4.3.3 Diffusion in Na-*rho*-ZMOF

The diffusion properties of water and ethanol were analyzed by the mean-squared displacement (MSD) from MD simulation

$$\mathrm{MSD}(t) = \frac{1}{KN}\sum_{k}^{K}\sum_{i=1}^{N}\left|\mathbf{r}_i(t+t_k) - \mathbf{r}_i(t_k)\right|^2 \tag{4.5}$$

where t is time, N is the number of molecules, and $\mathbf{r}_i(t)$ is the position of i^{th} molecule at time t. The multiple time-origin method was used to evaluate MSD and K is the number of time origins.

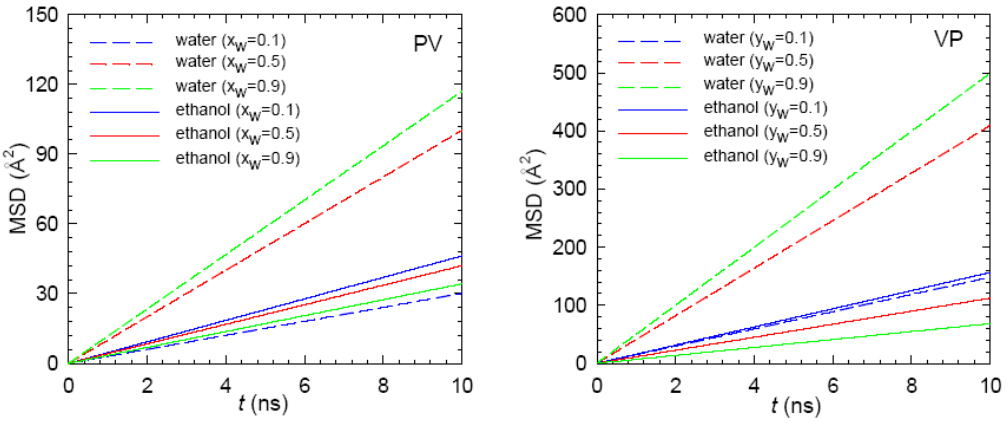

Figure 4.12. Mean-squared displacements for water/ethanol mixtures in Na-*rho*-ZMOF with various feed compositions.

Figure 4.12 shows the MSDs for water/ethanol mixtures in Na-*rho*-ZMOF with various feed compositions. At a low composition of water (x_w at PV condition or y_w = 0.1 at VP condition), water is strongly bound onto the ionic framework and nonframework Na^+ ions. As a consequence, water exhibits a very small mobility which is indeed smaller than ethanol. For water/ethanol mixtures in hydrophilic NaX and NaY zeolites, a small mobility of water was also observed at low water concentrations.[263] With increasing water composition in the feed, there is an increase in water motion but a decrease in ethanol motion. This is because water becomes less strongly bound when more water is adsorbed and starts to locate in the open α-cages. Simultaneously, further adsorbed water blocks the diffusion pathway for ethanol and thus the mobility of ethanol decreases. This trend is common at both PV and VP conditions. Nevertheless, the temperature at VP

condition (100 °C) is higher than that in PV condition (50 °C), the mobility of water and ethanol at VP is larger.

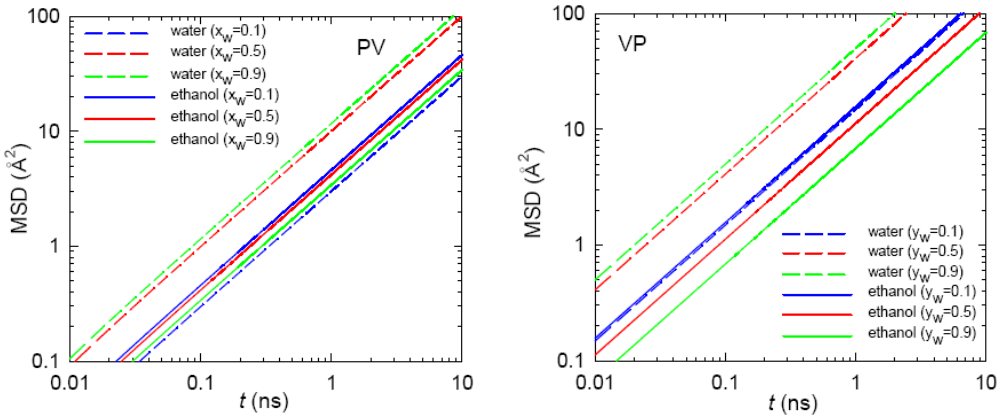

Figure 4.13. Mean-squared displacements on the log-scale for water/ethanol mixtures in Na-*rho*-ZMOF with various feed compositions.

The MSD curves were found to scale with t^{α} and $\alpha \approx 1$ as illustrated in Figure 4.13 based on log-log scale. This reveals that the MD simulations performed in our study were sufficiently long for water and ethanol to reach normal diffusion. Thus, the diffusivities of water and ethanol were estimated by the Einstein equation and plotted in Figures 4.14a and 4.14b. The diffusivity of water increases with increasing water composition and ethanol behaves oppositely. To quantify the diffusion selectivity, we define

$$S_{\mathrm{diff}(i/j)} = D_i / D_j \tag{4.6}$$

As shown in Figure 4.14c, the diffusion selectivity of water with respect to ethanol increases with increasing water composition at both PV and VP conditions. In addition, the diffusion selectivity is larger at VP than at PV condition because the higher temperature at VP facilitates the diffusion of water, the faster moving species, to a larger degree.

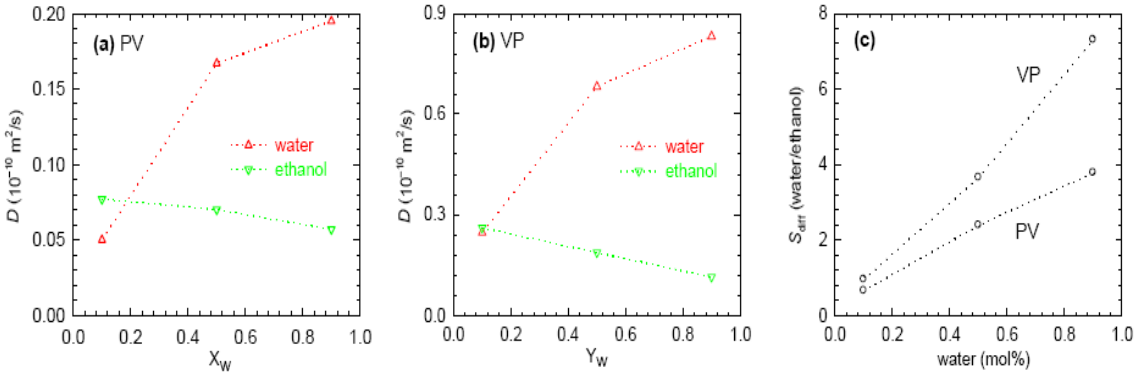

Figure 4.14. Diffusivities at (a) PV and (b) VP conditions. (c) Diffusion selectivities for water/ethanol mixtures in Na-*rho*-ZMOF.

4.3.4 Diffusion in $Zn_4O(bdc)(bpz)_2$

Figure 4.15 shows the MSDs for ethanol/water mixtures in $Zn_4O(bdc)(bpz)_2$ with various feed compositions.

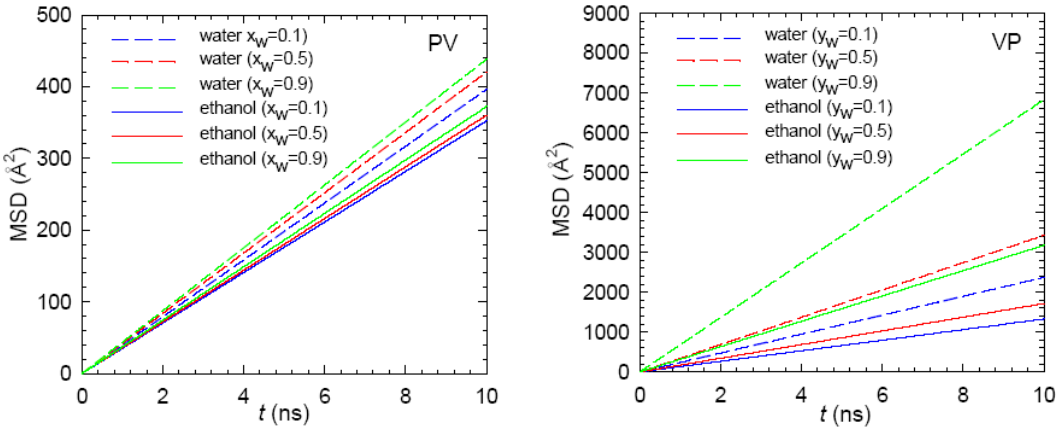

Figure 4.15. Mean-squared displacements for ethanol/water mixtures in $Zn_4O(bdc)(bpz)_2$ with various feed compositions.

At both PV and VP conditions, water exhibits a larger mobility compared to ethanol as a result of the smaller size of water and weaker interaction between water and the framework. With increasing composition of less adsorptive water, the free volume available in the framework become larger; therefore, the mobility of both components

particularly water increases. This behavior was also observed for water/ethanol mixtures in silicalite.[264] It should be noted that two major differences exist between the MSDs at PV and VP conditions. First, the MSD curves of water and ethanol at PV condition are close to each other, implying the similar mobility of two components. Second, the mobility of each component at VP condition is significantly larger due to the higher operating temperature.

Similar to Figure 4.13, Figure 4.16 also indicates that normal diffusion is reached for water and ethanol in $Zn_4O(bdc)(bpz)_2$ within the simulation time duration in this study.

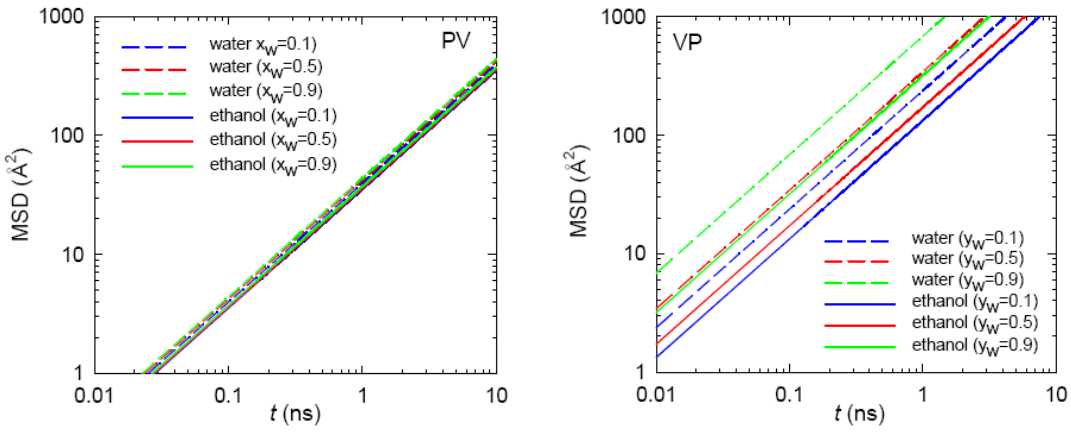

Figure 4.16. Mean-squared displacements on the log-scale for ethanol/water mixtures in $Zn_4O(bdc)(bpz)_2$ with various feed compositions.

Figures 4.17a and 4.17b show the diffusivities of water and ethanol in $Zn_4O(bdc)(bpz)_2$. As discussed in Figure 4.15, the mobility and diffusivity of each component increases with water composition. Figure 4.17c shows the diffusion selectivity of ethanol over water in $Zn_4O(bdc)(bpz)_2$. The diffusion selectivity ranges approximately from 0.5 to 0.9, implying small separation capability based on diffusion, unlike adsorption-based separation. With increasing water composition, the mobility of

water is enhanced to a larger degree compared to ethanol; consequently, the diffusion selectivity decreases.

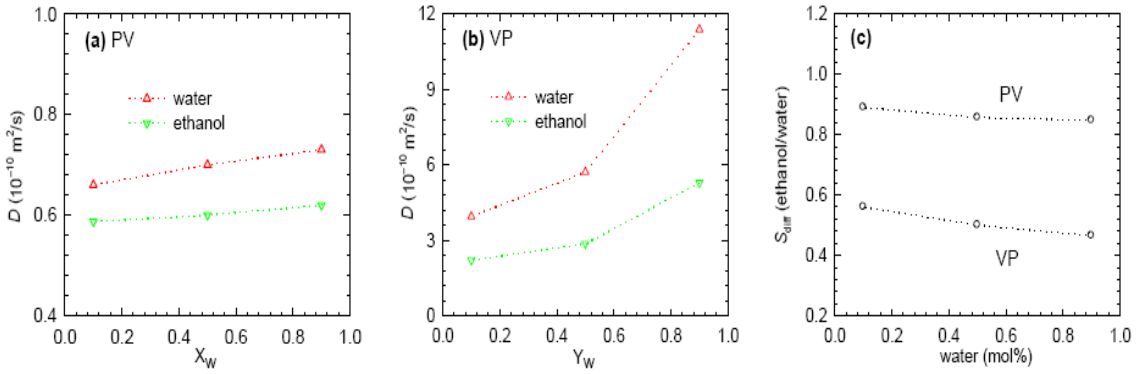

Figure 4.17. Diffusivities at (a) PV and (b) VP conditions. (c) Diffusion selectivities for ethanol/water mixtures in $Zn_4O(bdc)(bpz)_2$.

4.3.5 Permselectivity

The separation performance of a membrane is characterized by permselectivity, which depends on adsorption selectivity – an equilibrium property and diffusion selectivity – a dynamic property. If the permeate side is a vacuum, the permselectivity of a binary mixture can be approximated as[265-267]

$$S_{\text{perm}(i/j)} = S_{\text{ad}(i/j)} \cdot S_{\text{diff}(i/j)} \tag{4.7}$$

The adsorption selectivity $S_{\text{ad}(i/j)}$ and diffusion selectivity $S_{\text{diff}(i/j)}$ were calculated by Eq. (4.3) and (4.5), respectively.

As shown in Figure 4.18, the permselectivities of water/ethanol mixtures in Na-*rho*-ZMOF and $Zn_4O(bdc)(bpz)_2$ at both PV and VP conditions follow the same trend as the adsorption selectivities in Figures 4.3 and 4.8. Thus the adsorption plays a predominant role in the separation processes of this study. In Na-*rho*-ZMOF, the permselectivity decreases with water composition in the feed, particularly at PV condition. Consequently,

the hydrophilic MOF is more preferable to remove a small amount of water in water/ethanol mixtures and enrich ethanol in the feed side. In remarkable contrast, the permselectivity in $Zn_4O(bdc)(bpz)_2$ increases with water composition, which is more pronounced at PV condition and suited to extract a small amount of ethanol and enrich ethanol in the permeate side.

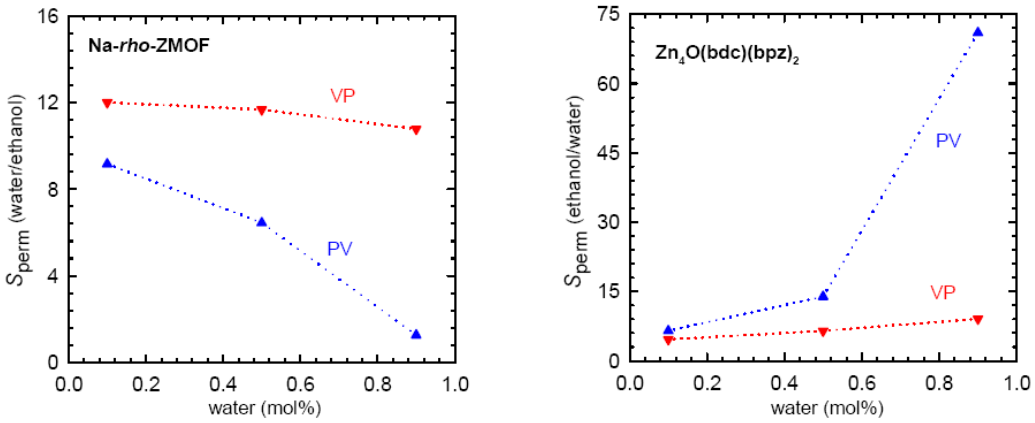

Figure 4.18. Permselectivities for water/ethanol mixtures in Na-*rho*-ZMOF and $Zn_4O(bdc)(bpz)_2$.

The maximum permselectivity predicted is approximately 12 in Na-*rho*-ZMOF at VP condition, and 75 in $Zn_4O(bdc)(bpz)_2$ at PV condition. The latter is higher than the selectivities experimentally measured for water/ethanol mixtures in several polymer and silicalite membranes. For example, the selectivity was determined to be 20 ~ 50 in poly(vinyl alcohol-g-acrylic acid) membrane at 30 °C,[268] 3 ~ 6 in CMG-OM-010 and 1060-SULZER membranes at temperature between 40 and 70 °C,[269] around 60 in silicalite at 30 °C.[261] The exceptionally high selectivity in $Zn_4O(bdc)(bpz)_2$ suggests that this MOF might be potentially interesting for biofuel purification.

4.4 Conclusions

The adsorption, diffusion, and permeation of water/ethanol mixtures in Na-*rho*-ZMOF and $Zn_4O(bdc)(bpz)_2$ have been simulated at both PV and VP conditions for biofuel purification. In hydrophilic Na-*rho*-ZMOF, water is more strongly adsorbed than ethanol; the adsorption selectivity of water over ethanol decreases with increasing water composition and is approximately the same at PV and VP conditions. In hydrophobic $Zn_4O(bdc)(bpz)_2$, ethanol is more favorably adsorbed against water; the adsorption selectivity of ethanol over water increases with increasing water composition and is higher at PV condition than at VP condition. The adsorption selectivities in $Zn_4O(bdc)(bpz)_2$ are higher than in zeolites. The diffusivity of water in Na-*rho*-ZMOF increases with increasing water composition but the opposite behavior is observed for ethanol, and the diffusion selectivity increases with water composition. In $Zn_4O(bdc)(bpz)_2$, the diffusivities of water and ethanol increase with water composition and the diffusion selectivity remains nearly a constant. The diffusion selectivities predicted in the two MOFs are smaller than in zeolites. Interestingly, the permselectivities follow the same trend as the adsorption selectivities. The maximum permselectivity in Na-*rho*-ZMOF is about 12 at VP condition in the composition range under study. Na-*rho*-ZMOF shows the potential for removing a small amount of water from water/ethanol mixtures and enriching ethanol at feed side. In contrast, $Zn_4O(bdc)(bpz)_2$ is better suited for the removal of a small amount of ethanol and enriches ethanol in permeate side. The maximum permselectivity in $Zn_4O(bdc)(bpz)_2$ is 75 at PV condition, higher than that in several polymeric and zeolite materials. Therefore, $Zn_4O(bdc)(bpz)_2$ is potentially useful for the separation of water/ethanol mixtures.

Chapter 5

Water Purification in *rho* Zeolite-like MOF

5.1 Introduction

Increasing world population and economic development have introduced a huge amount of contaminants such as metal ions Cu^{2+}, Cd^{2+} and Pb^{2+} into water.[270] These metal ions are environmentally toxic and carcinogenic to human being even at very low concentrations. They can accumulate in living organisms and cause dysfunction in central nervous system, circulatory and immune system.[271] Therefore, it is crucial to remove these metal ions from wastewater, thus minimizing health and environmental risks.

A handful of techniques have been proposed for the removal of metal ions, including ion exchange, adsorption and membrane filtration.[272] Among these, ion exchange is considered a cost-effective technique as it can treat very dilute solution and achieve selective separation. There are primarily two types of ion exchangers (inorganic and organic), and each type has naturally occurring and synthetic materials.[273] The common feature of these materials is that they contain ionic framework and nonframework cations, and the latter can exchange with metal ions in wastewater. Most inorganic ion exchangers possess small pore sizes and thus exchange kinetics is slow.[274] While organic exchangers such as polymer resins are rapid in exchange, they may not be chemical/mechanical stable in ionic solutions compared against inorganic counterparts.[275] Considerable interest is being focused on the development of high-performance ion exchangers for water treatment.

MOFs have emerged as a new family of hybrid porous materials, and a large number of experimental and simulation studies have been reported for gas adsorption and separation in MOFs.[249,276] With readily tunable organic linkers and metal oxides, MOFs have been also explored for the removal of metal ions toward water purification. However, only very few experimental studies were conducted. Custelcean et al. observed the selective encapsulation of SO_4^{2-} anion from a highly competitive aqueous environment into a Ni-coordination framework functionalized by urea.[277] In a porous bilayered open coordination polymer, Mi et al. investigated the removal of metal ions by exchange along with adsorption onto functional groups.[103] Fang et al. synthesized seven amine-templated MOFs and found the guest organic cations could be exchanged by K^+ ion.[278] Plabst et al. and Lu et al. demonstrated that cation exchange in anionic MOFs plays an important role in framework stabilization and tunable luminescent properties.[115,279] Two Ag(I)/Cu(I)-based MOFs reported by Fei et al. were designed to possess weak electrostatic interactions between cationic layers and interlamellar anions, and thus displaying reversible anion exchange for a variety of inorganic species.[280]

Currently, the fundamental understanding of ion exchange in MOFs remains largely elusive. For the development of new MOFs for water purification, however, molecular insight into ion exchange is indispensible. In this study, we report a molecular simulation study for the exchange of Pb^{2+} ions with Na^+ ions in *rho* MOF. Pb^{2+} is chosen here because it is toxic and a common contaminant after water transporting through lead-bearing household pipelines. The *rho*-ZMOF is a unique anionic MOF with a topology similar to *rho*-zeolite. Nevertheless, the substitution of oxygen in *rho*-zeolite with 4,5-imidazoledicarboxylic acid (H_3ImDC) generates a very open-framework with extra-large

cavity of 18.2 Å in diameter. Unlike *rho*-zeolite and other *rho*-aluminosilicate or aluminophosphate, *rho*-ZMOF contains twice as many positive charges (48 vs. 24) in a unit cell to neutralize the anionic framework. Therefore, ionic conductivity could be augmented by the elevated charged density in *rho*-ZMOF. The simulation models and methods are briefly described in Section 5.2. In Section 5.3, we present the density distributions of ions at different simulation stages to identify ion exchange process. To provide deep insight, the potentials of mean force for ions moving from solution into *rho*-ZMOF are examined. The structural and dynamic properties of ions in *rho*-ZMOF are also discussed. Finally, concluding remarks are summarized in Section 5.4.

5.2 Simulation Models and Methods

Figure 5.1 shows a unit cell of *rho*-ZMOF constructed from experimental X-ray crystallographic data.[218] The structure contains 8-membered ring (8MR), 6-membered ring (6MR) and 4-membered ring (4MR), respectively. The as-synthesized negatively charged *rho*-ZMOF contains charge-balancing doubly protonated 1,3,4,6,7,8-hexahydro-2H-pyrimido[1,2-a]pyrimidine (HPP). The HPP organic cations in parent framework are exchangeable with other organic and inorganic cations. For example, Na-exchanged *rho*-ZMOF (Na-*rho*-ZMOF) with a formula of $[In_{48}(C_5N_2O_4H_2)_{96}][Na^+_{48}(H_2O)_{282}]$ was obtained by replacing HPP cations with Na^+ ions.[218] From molecular simulation, we have recently characterized the locations of Na^+ ions and examined the separation of gas mixtures and water/alcohol mixtures in Na-*rho*-ZMOF.[227,254]

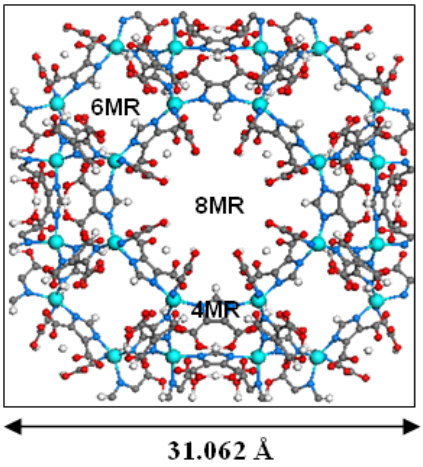

Figure 5.1. Unit cell of *rho*-ZMOF (nonframework ions are not shown). The 8-membered ring (8MR), 6-membered ring (6MR) and 4-membered ring (4MR) are indicated.Color code: In, cyan; N, blue; C, grey; O, red; and H, white.

To investigate the exchange of Pb^{2+} with Na^{+} in *rho*-ZMOF, a simulation system with dimension of 124.124 Å × 31.062 Å × 31.062 Å was constructed. As shown in Figure 5.2a, Na-*rho*-ZMOF with a thickness of 62.124 Å (2 × 1 × 1 unit cells) was located at the center of the simulation box and in contact with $PbCl_2$ solution on each side. Each solution compartment contained 24 Pb^{2+} and 48 Cl^{-} ions, corresponding to a concentration of 1.4 M. Water was treated as a continuum with dielectric constant $\varepsilon_r = 78$. In principle, molecular simulation with a large number of explicit water molecules represents a detailed approach to study ions in aqueous medium. However, a significant computational cost is associated with water molecules, which is indeed not of interest. Therefore, it is usually desirable to incorporate the influence of water implicitly, which is computationally inexpensive but also provides useful insight.

The ions in this study were mimicked by rigid model that incorporates Coulombic and Lennard-Jones (LJ) interactions

$$u_{ij}(r) = \frac{q_i q_j}{4\pi\varepsilon_0\varepsilon_r r} + 4\varepsilon_{ij}\left[\left(\frac{\sigma_{ij}}{r}\right)^{12} - \left(\frac{\sigma_{ij}}{r}\right)^{6}\right] \quad (5.1)$$

where r is the inter-atomic distance and $\varepsilon_0 = 8.8542\times10^{-12}\,\mathrm{C^2N^{-1}m^{-2}}$ is the permittivity of vacuum. The interactions between ions and *rho*-ZMOF framework atoms were also mimicked by Eq. (5.1). The atomic charges and force fields parameters for *rho*-ZMOF were were same as used in previous chapters. The LJ parameters listed in Table 5.1 were adopted from the Universal force field (UFF) and the Lorentz–Berthelot combining rules were used to calculate cross interaction parameters.

Table 5.1. Lennard-Jones parameters of framework atoms and heavy metal ions.

Atom	σ (Å)	ε/k_B (K)
In	3.976	301.157
N	3.260	34.690
O	3.118	30.166
C	3.431	52.790
H	2.571	22.122
Na^+	2.658	15.083
Pb^{2+}	3.829	333.65
Cl^-	3.517	114.24

The simulation system was subject to energy minimization using the steepest descent method and then MD simulation was performed for 10 ns in a canonical ensemble using the GROMACS package 4.5.[256] The periodic boundary conditions were used in all three dimensions. While *rho*-ZMOF framework atoms were fixed during simulation, nonframework Na^+ ions were free to move. The particle-mesh-Ewald (PME) technique was applied to calculate Coulombic interactions with a grid spacing of 0.12 Å and a fourth-order interpolation. Temperature was maintained at 298 K by Nosé-Hoover

method with a relaxation time of 0.1 ps and trajectory was saved every 1 ps. To calculate the velocity autocorrelation function of ions, a 100 ps trajectory was saved every 1 fs. Furthermore, the potentials of mean force (PMFs) for different types of ions (Pb^{2+}, Na^{+} and Cl^{-}) moving from solution to *rho*-ZMOF were calculated by

$$\mathrm{PMF}(x) = \int_{x_0}^{x} \langle F(x') \rangle \mathrm{d}x' \tag{5.2}$$

where $\langle F(x') \rangle$ is the ensemble averaged force acting on an ion at a position x'. PMF(x) gives the work needed for an ion moving from a reference position x_0 to x along the x-axis. PMF has been proved to be a useful quantity to elucidate ion selectivity[281] and ion exchange[282] in confined space. In this study, the solution compartment was considered the reference position. For each type of ion, the calculations of PMFs were performed by 30 independent umbrella sampling simulations.[283] In each 1-ns simulation, an ion was harmonically restrained in a sampling window with a spacing of 1.5 Å. The strength of the harmonic biasing force constant was 10 kJ mol^{-1} $Å^{-2}$. This value was found to be suitable to maintain an overlap between trajectories of adjacent sampling windows, which is crucial for obtaining accurate PMFs. Thereafter, the weighted histogram analysis method (WHAM) was used to estimate PMFs.[284]

5.3 Results and discussion

First, we identify ion exchange process by visualizing the simulation snapshots at different stages and examining the density profiles of ions. Then, we present the PMFs for ions at different positions to examine the driving force for ions to move from solution to *rho*-ZMOF. Finally, we discuss the structural and dynamic properties of ions in *rho*-ZMOF in order to quantify the selective interactions of ions with the framework.

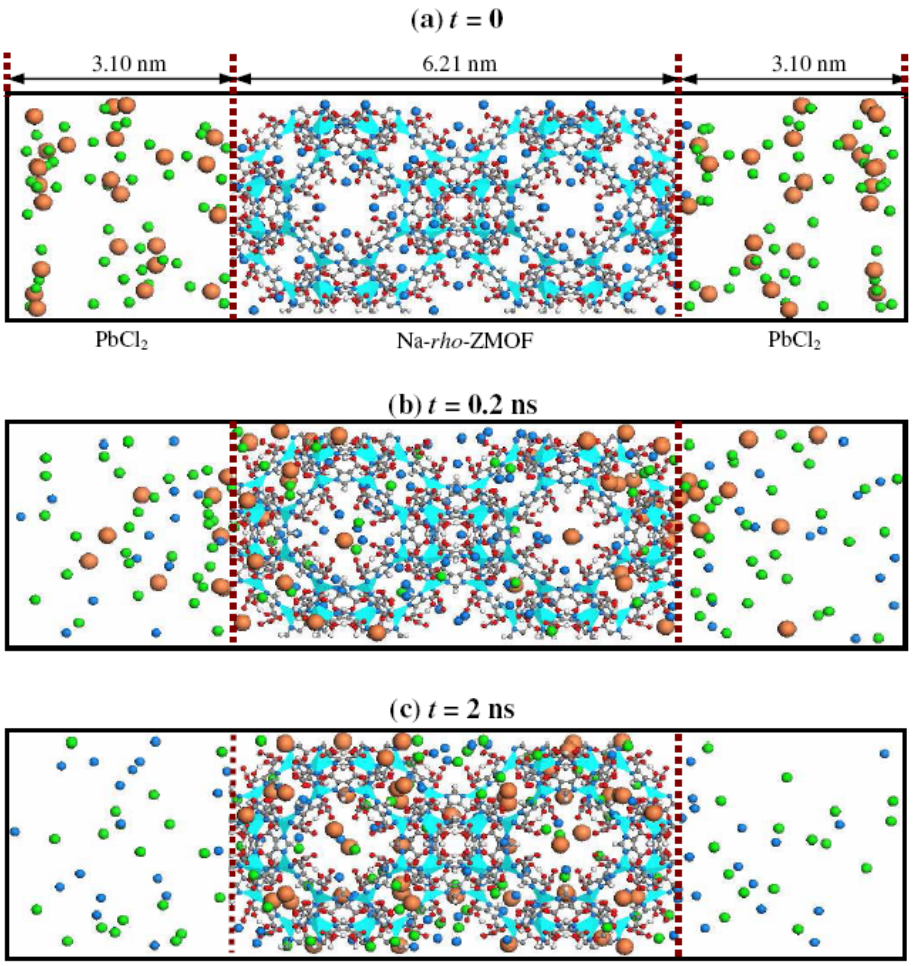

Figure 5.2. Snapshots of simulation system (a) t = 0 (b) t = 0.2 ns and (c) t = 2 ns. Color code: Pb^{2+}: orange; Cl^{-}: green; Na^{+}: blue.

5.3.1 Ion exchange process

Figure 5.2a shows the snapshots of simulation system at t = 0 (prior to simulation). Initially, Pb^{2+} and Cl^{-} ions are in solution and Na^{+} ions reside in *rho*-ZMOF framework. When simulation starts, Pb^{2+} ions rapidly move into the framework and Na^{+} ions move out, which indicates that ion exchange between Pb^{2+} and Na^{+} ions occurs within a few picoseconds. As shown in Figure 5.2b at t = 0.2 ns, a large number of Pb^{2+} ions have moved into *rho*-ZMOF, particularly near the solution/*rho*-ZMOF interface. Meanwhile, Na^{+} ions move out from *rho*-ZMOF and stay in solution. A portion of Cl^{-} ions also move

into *rho*-ZMOF during ion exchange. Entering of Cl^- ions into a negatively charged nanopore was also observed previously.[285] Once exchanged, Pb^{2+} ions prefer staying in the framework without moving back to solution. This induces a Donnan effect on the distributions of Na^+ and Cl^- ions between solution and framework. At t = 2 ns shown in Figure 5.2c, all Pb^{2+} ions are exchanged and reside in *rho*-ZMOF. In addition, Pb^{2+} ions located at the solution/*rho*-ZMOF interface move into the interior of *rho*-ZMOF. The snapshot at simulation time beyond 2 ns is similar to Figure 5.2c, implying an equilibrium state is reached in less than 2 ns. It is observed that the exchanged Pb^{2+} ions in *rho*-ZMOF are preferentially located at 8MR, 6MR and 4MR. Pb^{2+} ions at these different locations exhibit distinct dynamics, which will be discussed below.

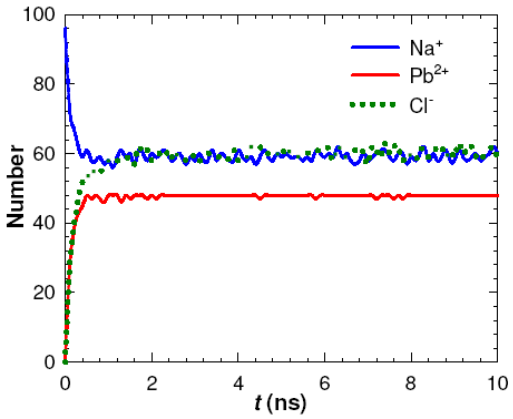

Figure 5.3. Numbers of Na^+, Pb^{2+} and Cl^- ions in Na-*rho*-ZMOF as a function of simulation duration.

The numbers of Pb^{2+}, Na^+ and Cl^- resident in *rho*-ZMOF as a function of simulation duration are shown in Figure 5.3. Consistent with Figure 5.2, the numbers of Pb^{2+} and Cl^- ions initially increase, while the number of Na^+ ions decreases. After approximately 2 ns, the numbers of all three types of ions in *rho*-ZMOF are nearly constant. While all

Pb^{2+} ions reside in *rho*-ZMOF, Na^{+} and Cl^{-} ions in *rho*-ZMOF are in a dynamic equilibrium with their counterparts in solution.

Figure 5.4 depicts quantitatively the density profiles of Pb^{2+}, Na^{+} and Cl^{-} ions at three different stages, corresponding to the snapshots in Figure 5.2. The density profiles were calculated by dividing the simulation box into small slices along the *x*-axis with $\Delta x = 0.2$ nm and the number densities per nm^3 in each slice were estimated. At $t = 0$, Na^{+} ions are in *rho*-ZMOF, whereas Pb^{2+} and Cl^{-} ions are in solution. Na^{+} ions in *rho*-ZMOF exhibit several distinct peaks due to preferential locations at different sites.

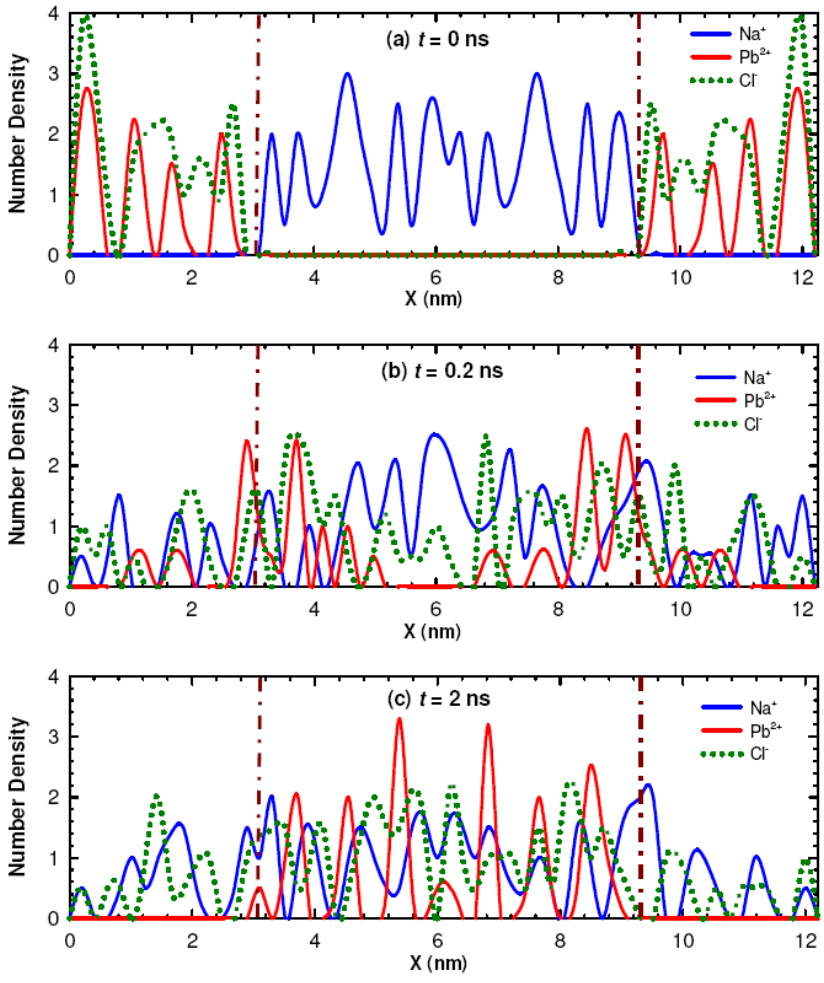

Figure 5.4. Density profiles of Na^{+}, Pb^{2+} and Cl^{-} ions at (a) $t = 0$ (b) $t = 0.2$ ns and (c) $t = 2$ ns. The dotted-dashed line indicates solution/*rho*-ZMOF interface.

In principle, Pb^{2+} and Cl^- ions in solution are distributed homogeneously; however, this is not observed in Figure 5.4a. The reason is that Pb^{2+} and Cl^- ions tend to form clusters (as demonstrated in Figure 5.2a) and the density profiles were calculated at a single time not ensemble averaged. At t = 0.2 ns after ion exchange occurs, Na^+ ions move out from *rho*-ZMOF into solution, thus the density decreases in *rho*-ZMOF but increases in solution. The situation for Pb^{2+} and Cl^- ions is opposite and their densities in *rho*-ZMOF increase from zero. These variations are observed until a dynamic equilibrium is reached at about 2 ns. As shown in Figure 5.4c, Pb^{2+} ions in *rho*-ZMOF after equilibrium exhibit pronounced peaks indicating preferential locations at 8MR, 6MR and 4MR.

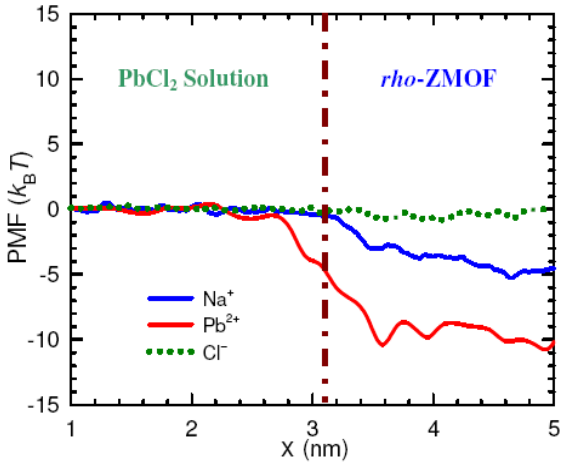

Figure 5.5. Potentials of mean force (PMFs) for Na^+, Pb^{2+} and Cl^- ions moving from solution to *rho*-ZMOF. The dotted-dashed line indicates the solution/*rho*-ZMOF interface.

Figure 5.5 illustrates the PMFs for ions moving from solution to *rho*-ZMOF. The reference position is in solution and thus the PMFs are equal to zero for all the three types of ions (Pb^{2+}, Na^+ and Cl^-) in solution compartment away from *rho*-ZMOF. Nevertheless, the PMFs for Pb^{2+} and Na^+ ions decrease upon moving towards *rho*-ZMOF due to

attractive interactions exerted by the negatively charged *rho*-ZMOF framework. In the interior of *rho*-ZMOF, Pb^{2+} possesses a larger PMF (–10 k_BT) than Na^+ (–5 k_BT), revealing Pb^{2+} interacts more strongly with the framework. This is the driving force for the exchange between these two types of ions. In addition, the PMF in *rho*-ZMOF can be considered the energy barrier for ions to move from *rho*-ZMOF to solution. With a large PMF and hence a large barrier, Pb^{2+} ions cannot move back to solution once exchanged. However, Na^+ ions in *rho*-ZMOF and solution have a dynamic equilibrium and can exchange due to a small PMF in *rho*-ZMOF. Cl^- ions have no free energy gain to move into *rho*-ZMOF, which was also observed in other negatively charged nanopores.[285]

5.3.2 Ions in *rho*-ZMOF

To elucidate the structures of ions in *rho*-ZMOF after equilibrium, radial distribution functions g(*r*) were calculated by

$$g_{ij}(r) = \frac{\Delta N_{ij}(r, r+\Delta r)\, V}{4\pi r^2 \Delta r\, N_i N_j} \tag{5.3}$$

where r is the distance between species i and j, $\Delta N_{ij}(r, r+\Delta r)$ is the number of species j around i within a shell from r to $r + \Delta r$, V is the system volume, N_i and N_j are the numbers of species i and j. Figure 5.6 shows the g(*r*) of Pb^{2+} and Na^+ ions around the framework atoms In, O_1 and O_2 respectively. In addition, the insets give the coordination numbers of ions around the framework atoms as calculated by

$$N(r) = \rho_{\text{ion}} \int_0^r g_{\text{atom-ion}}(r')\, 4\pi r'^2\, \mathrm{d}r' \tag{5.4}$$

where ρ_{ion} is the average density of a specific type of ions. Compared to Na^+, Pb^{2+} has a much sharper peak and a larger $N(r)$ around all the three framework atoms. This leads to

a higher coordination environment for Pb^{2+} in the framework and thus a larger PMF as discussed above.

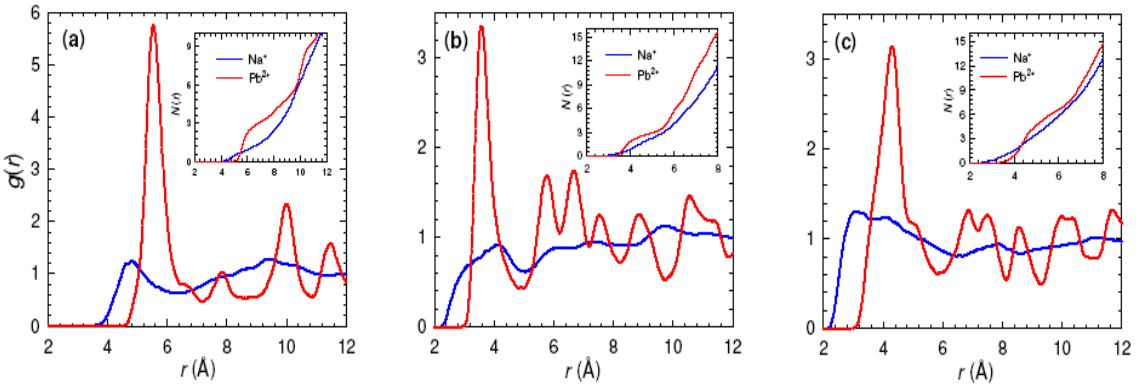

Figure 5.6. Radial distribution functions of Na^+ and Pb^{2+} ions around the framework atoms (a) In (b) O_1 and (c) O_2. The insets show the coordination numbers of ions around the framework atoms.

The ions are in dynamic equilibrium after ion exchange as observed in a movie provided in the Supporting information. The dynamics nature of Pb^{2+} and Na^+ ions in *rho*-ZMOF can be analyzed by residence-time distributions (RTDs) and mean-squared displacements (MSDs). Specifically, the RTDs were calculated by

$$\mathrm{RTD}(t) = \frac{\sum_{i=1}^{N_0(t_0)} \delta_i\left(t_0, t_0 + t\right)}{N_0\left(t_0\right)} \tag{5.5}$$

where δ_i(t) is a binary function equal to unity if i^{th} ion remains in *rho*-ZMOF from t_0 to $t_0 + t$ without escaping, and zero otherwise. Also called survival-time correlation function, the RTD provides the number of ions that stay in *rho*-ZMOF over a time span t without exchanging with counterparts outside *rho*-ZMOF. The RTD in Eq. (5.5) was normalized by the initial number of ions $N_0(t)$ at t_0 in *rho*-ZMOF. To improve statistical accuracy, the multiple time origin method was utilized to estimate the ensemble averaged RTD.

Figure 5.7a shows the RTDs of Pb^{2+} and Na^{+} ions in *rho*-ZMOF. A constant value of RTD is observed for Pb^{2+}, revealing all the exchanged Pb^{2+} ions stay continuously in *rho*-ZMOF. Nevertheless, the RTD of Na^{+} falls to zero within approximately 2 ns, which denotes Na^{+} ions reside in *rho*-ZMOF for a shorter time compared to Pb^{2+} ions and exchange with the counterpart in solution. Again, these results suggest that Pb^{2+} has a more favorable interaction with the framework.

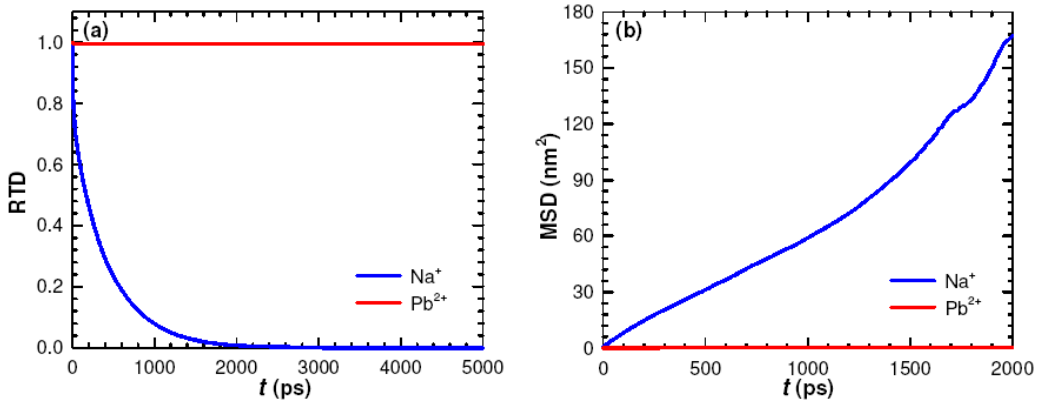

Figure 5.7. (a) Residence time distributions and (b) mean-squared displacements of Pb^{2+} and Na^{+} ions in *rho*-ZMOF.

The MSDs of ions in *rho*-ZMOF were calculated by

$$\mathrm{MSD}(t) = \frac{1}{N}\sum_{i=1}^{N}\left|\mathbf{r}_i(t+t_k) - \mathbf{r}_i(t_k)\right|^2 \tag{5.6}$$

where N is the number of ions and $\mathbf{r}_i(t)$ is the position of i^{th} ion at time t. The multiple time origin method was also used to evaluate MSDs. As shown in Figure 5.7b, the MSD of Pb^{2+} is vanishingly small which denotes the strong binding of Pb^{2+} in *rho*-ZMOF leads to a negligible mobility of Pb^{2+}. In contrast, Na^{+} exhibits a significantly larger MSD because of the relatively weak interactions between Na^{+} and *rho*-ZMOF.

As pointed out earlier, the exchanged Pb^{2+} ions in *rho*-ZMOF are preferentially located at 8MR, 6MR and 4MR. The Pb^{2+} ions at each site have distinct dynamic behavior due to the confinement effect of surrounding framework atoms. As shown in Figure 5.8a, the MSDs of Pb^{2+} ions at the three locations are different. The Pb^{2+} ions at 8MR have the largest MSD, followed by those at 6MR and 4MR. This is attributed to geometrical constraint, i.e., 8MR has the largest ring size and imposes the smallest constraint on Pb^{2+} ions. However, 4MR behaves the opposite way. Despite the difference in MSDs, the overall mobility of Pb^{2+} ions is small as seen in Figure 5.7b.

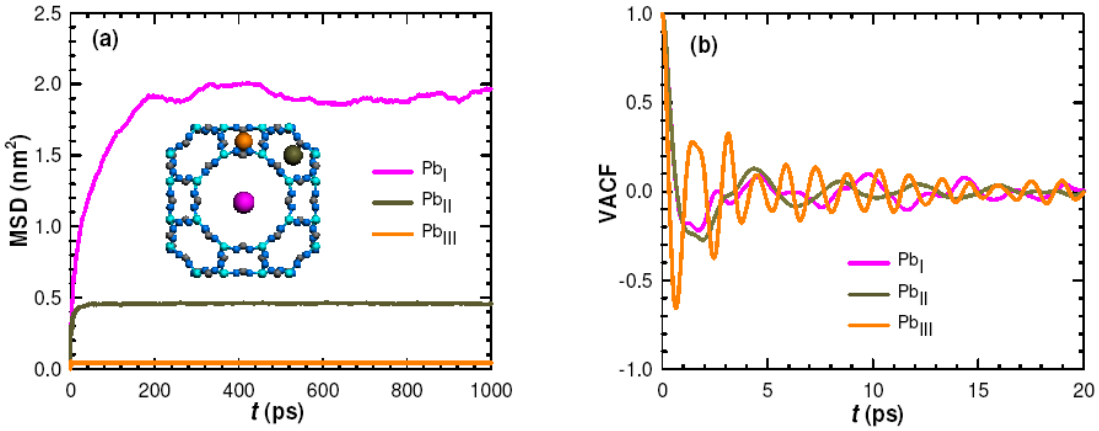

Figure 5.8. (a) Mean-squared displacements and (b) velocity autocorrelation functions of Pb^{2+} ions in *rho*-ZMOF framework. Pb^{2+} in 8MR: pink; Pb^{2+} in 6MR, brown; Pb^{2+} in 4MR, orange.

We further characterize the Pb^{2+} ions in 8MR, 6MR and 4MR by the normalized velocity autocorrelation functions (VACFs) calculated by

$$C_v(t) = \frac{\langle v(0) \cdot v(t) \rangle}{\langle v(0) \cdot v(0) \rangle} \tag{5.7}$$

where the ensemble averaged $\langle v(0) \cdot v(t) \rangle$ is

$$\langle v(0) \cdot v(t) \rangle = \frac{1}{N} \sum_{i=1}^{N} [v_i(t_k) \cdot v_i(t_k + t)] \tag{5.8}$$

with $v_i(t)$ as the velocity of i^{th} ion at time t. The general behavior of VACFs shown in Figure 5.8b is similar for Pb^{2+} at three different locations. That is, the VACFs oscillate and decay to zero indicating the random motion of Pb^{2+} ions around binding sites. Nevertheless, the VACF at 8MR exhibit the smallest oscillation, which denotes a diffusive motion for Pb^{2+} ions in 8MR. In contrast, drastic oscillation is observed in the VACF at 4MR implying frequent vibrational motion for Pb^{2+} ions in 4MR. Consistent with the MSDs in Figure 5.8a, the VACFs reveal that Pb^{2+} ions at 4MR interact with *rho*-ZMOF framework the most strongly among the three sites, and thus exhibit the smallest mobility. It is worthwhile to note that divalent ions (Mg^{2+}) were experimentally observed to locate at 4MR of *rho*-ZMOF.[193]

5.4 Conclusions

We have investigated the exchange of Pb^{2+} ions with nonframework Na^+ ions in *rho*-ZMOF using molecular dynamics simulation. As evidenced from the density profiles of ions at different simulation stages, ion exchange is observed to occur. After equilibrium, Pb^{2+} ions reside in *rho*-ZMOF without exchanging with other ions in solution; however, Na^+ and Cl^- ions are in a dynamic equilibrium with solution. The PMF for Pb^{2+} in *rho*-ZMOF is $-10\ k_BT$, larger than that for Na^+ ($-5\ k_BT$). This implies that Pb^{2+} interacts more favorably with the framework and promotes ion exchange. A sharp peak is observed in the radial distribution functions of Pb^{2+} around the framework atoms. The constant value of RTD for Pb^{2+} reveals all the exchanged Pb^{2+} ions stay continuously in *rho*-ZMOF and the mobility of Pb^{2+} is very small. In contrast, Na^+ exhibits a large MSD and the RTD of Na^+ drops to zero after approximately 2 ns. This suggests Na^+ ions reside in *rho*-ZMOF for a shorter time than Pb^{2+} and can exchange with the counterpart in solution.

Pb^{2+} ions in *rho*-ZMOF are preferentially located at 8MR, 6MR and 4MR. Because of confinement effect, the dynamic behavior of Pb^{2+} ions differs at the three sites as reflected by MSDs and VACFs. Pb^{2+} ions at 8MR have the largest MSD and smallest oscillation as attributed to the largest ring size of 8MR, which exerts the smallest constraint on Pb^{2+} ions. Nevertheless, the MSD for Pb^{2+} ions at 4MR is almost zero and the VACF oscillates drastically. The molecular insight provided by this simulation study is useful for the mechanistic understanding of ion exchange in *rho*-ZMOF and for the rational development of new MOFs for water purification.

Chapter 6

Conclusions and Future Work

6.1 Conclusions

In this thesis, molecular simulations have been carried out to unravel the microscopic properties of water and alcohols in MOFs. The applications of MOFs in liquid-phase separation, including biofuel and water purification, were also investigated. The major observations are summarized below.

In Chapter 2, the adsorption, mobility and vibration of water and the interplay between nonframework ions and water were examined in ion exchanged *rho*-ZMOF. The charge balancing Na^+ ions were identify to locate at two favorable positions in Na-*rho*-ZMOF. Site I is in the single 8-membered ring and site II is in the α-cage; the locations are closely resembled to those in *rho*-zeolite. The mobility of ions in *rho*-ZMOF is negligible. Water strongly adsorbs in *rho*-ZMOF with a three step adsorption mechanism. At low pressures, the adsorption is proximal to Na^+ ions, particularly at site II; with increasing pressure, adsorption occurs near the framework and finally in the α-cage. Upon water adsorption, Na^+ ions are redistributed from site I to site II. From Li-*rho*-ZMOF, Na-*rho*-ZMOF to Cs-*rho*-ZMOF, the extent of water adsorption and isosteric heat decrease due to the reduced interaction between ions and water. At low pressures, the mobility of water is negligible but increases with increasing pressure and finally decreases at saturation. The mobility of ions is increased upon reaching sufficient hydration level. The vibrational spectra of water in *rho*-ZMOF exhibit three distinct bands corresponding to librational motion, bending and stretching. Due to the

confinement, a blue shift from bulk water is observed in the librational peak. With increasing pressure, bending frequency has a blue shift and stretching frequency approaches the band of bulk water.

In Chapter 3, adsorption of water, methanol and ethanol was investigated in hydrophilic and hydrophobic zeolitic MOFs with *rho* topology. Due to strong interactions with the nonframework ions and ionic framework in hydrophilic Na-*rho*-ZMOF, all three adsorbates exhibit type I adsorption isotherms. With a smaller size, water has a larger adsorption capacity than methanol and ethanol. Water prefers to locate near the narrow windows in Na-*rho*-ZMOF, while methanol and ethanol stay in the α-cage. In water/methanol and water/ethanol mixtures, water is selectively adsorbed over alcohols at all pressures. In hydrophobic ZIF-71, adsorption isotherms are type V attributed to the weak framework-adsorbate affinity. Water adsorption is negligible at low pressures and increases sharply at 22 kPa because of capillary condensation. The adsorption of methanol and ethanol shows a cluster-growth mechanism at low pressures and continuous pore filling at high pressures. The adsorption order is water < methanol < ethanol at low pressures, but the opposite is true at high pressures due to entropy effect. In mixtures, alcohols are selectively adsorbed at low pressures but reversed with increasing pressure. In contrast to ZIF-71, the framework charges of Na-*rho*-ZMOF have a substantial effect on adsorption.

In Chapter 4, biofuel purification (water/ethanol mixtures) at pervaporation and vapor permeation conditions was investigated in hydrophilic and hydrophobic MOFs. In hydrophilic Na-*rho*-ZMOF, water is more strongly adsorbed than ethanol and the adsorption selectivity of water/ethanol is higher at a low composition of water. With

increasing water composition, the diffusivity of water in Na-*rho*-ZMOF increases but the diffusivity of ethanol decreases; consequently, the diffusion selectivity of water/ethanol increases. In hydrophobic $Zn_4O(bdc)(bpz)_2$, ethanol is preferentially adsorbed and the adsorption selectivity of ethanol/water is higher at a low composition of ethanol. With increasing water composition, the diffusivities of water and ethanol increase and the diffusion selectivity ethanol/water decreases slightly. In Na-*rho*-ZMOF, the maximum permselectivity is about 12 at VP condition and suitable for removing small amounts of water to enrich ethanol at the feed side. The maximum permselectivity in $Zn_4O(bdc)(bpz)_2$ is about 75 at PV condition and better suited to remove a small amount of ethanol to enrich at the permeate side.

In Chapter 5, exchange of Pb^{2+} ions with nonframework Na^+ ions in *rho*-MOF was investigated for water purification. From the density profiles of ions at different simulation stages, ion exchange was observed. At equilibrium, all Pb^{2+} ions are exchanged and stay in *rho*-ZMOF, while Na^+ and Cl^- ions are in dynamic equilibrium with ions in solution. The potential of mean force for Pb^{2+} in *rho*-ZMOF is 10 k_BT, larger than that for Na^+ and this implies that interaction of Pb^{2+} with framework is favorable to promote ion exchange. Pb^{2+} ions exhibit a pronounced peak in the radial distribution function around framework atoms. From the residence-time distributions and mean-squared displacements, all exchanged Pb^{2+} ions are found to stay continuously in *rho*-ZMOF without exchanging with other ions in solution due to strong interaction with *rho*-ZMOF; however, Na^+ ions display a shorter residence time and a larger mobility. The exchanged Pb^{2+} ions in *rho*-ZMOF are located at eight-, six, and four-member rings and

show distinct dynamic behavior at different locations. Pb^{2+} ions have the largest mobility at 8MR due to the largest ring size, but a negligible mobility at 4MR.

6.2 Future Work

The initial interest in MOFs was primarily on gas storage because of the high surface area and pore volume achievable in MOFs. Thereafter, the applications were extended to separation of gases and liquid mixtures, catalysis, ion exchange, etc. Recently, MOFs have attracted much attention in membrane and chromatography separation, drug delivery, sensing and imaging. Due to the infinite number of tunable MOFs, experimental synthesis and testing alone are tedious and time-consuming. In this regard, molecular simulation can be a robust tool to unravel the underlying mechanism at a microscopic level and assist in the rational design of novel MOFs for applications. Molecular simulation has been successful in modeling gas adsorption and storage; however, studies in other areas are currently very limited and recommended for future work.

- Separation of gas mixtures is one of the most studied areas. Majority of these studies were on equilibrium separation, however, there are few studies on kinetic separation pertaining to small gases. The kinetic separation of other mixtures is an interesting direction and needs further investigation. In addition, steric separation in MOFs and could be another mechanism and should be explored computationally.
- Compared with the applications of MOFs in gas phase, simulations dealing with liquid phase are scarce. This is largely due to the significant amount of simulation time required for dense liquid phase. Consequently, microscopic

understanding of liquid phase is less complete. With increasing computational power, however, we expect more simulation studies will be reported in this area.

- All reported simulation studies on MOFs to date have been carried out on the basis of infinite crystals using periodic boundary conditions. Studies with more realistic description to represent systems with continuous flow such as membranes and chromatographic systems are needed; and sometimes it is necessary to include surface effects.
- Framework flexibility can substantially influence diffusion in MOFs. However, most simulations considered rigid frameworks, except a few in which framework flexibility was accounted for using empirical force fields. To accurately describe the flexibility of MOFs, suitable force fields need to be developed.
- A number of MOFs show structural change upon adsorption at different pressures and temperatures. Only few modeling studies attempted to elucidate this phenomenon; however, the underlying mechanism remains elusive. More sophisticated modeling is desired to provide atomic-resolution and time-resolved insights.
- A sub-class of MOFs are chiral and can be used for enantioselective separation. The advantage of using chiral MOFs is their extraordinary surface area, which may enhance separation rates. To better elucidate the interactions of enantiomers with chiral MOFs and improve separation efficiency, detailed modeling studies are necessary.
- A large number of MOFs are moisture sensitive. To understand the stability of MOFs in water or many other organic solvents is imperative for practical

applications. While first-principles quantum chemical calculations can be used to examine small clusters, it might be more appropriate to apply reactive force fields such as ReaxFF for this purpose.

- With metal-oxides as building block in the frameworks, MOFs have been experimentally demonstrated being useful for catalytic reactions. Molecular modeling for MOFs in this area is rare and at the early stage. Quantum chemical calculations are required to provide the fundamental mechanisms for MOFs in catalysis.

References

(1) Schuth, F.; Sing, K. S. W.; Weitkamp, J. *Handbook of Porous Solids*; Wiley-VCH Verlag GmbH, Weinheim, **2008**.

(2) Kulprathipanja, S. *Zeolites in Industrial Separation and Catalysis*; Wiley-VCH Verlag GmbH , Weinheim, **2010**.

(3) Davis, M. E. *Ind. Eng. Chem. Res.* **1991**, *30*, 1675.

(4) Davis, M. E. *Chem. Eur. J.* **1997**, *3*, 1745.

(5) Jones, C. W.; Tsuji, K.; Davis, M. E. *Nature* **1998**, *393*, 52.

(6) Ferey, G. *Chem. Mater.* **2001**, *13*, 3084.

(7) Jones, C. W. *Science* **2003**, *300*, 439.

(8) Desiraju, G. R. *Angew. Chem., Int. Ed.* **1995**, *34*, 2311.

(9) Venkataraman, D.; Lee, S.; Zhang, J. S.; Moore, J. S. *Nature* **1994**, *371*, 591.

(10) Hoskins, B. F.; Robson, R. *J. Am. Chem. Soc.* **1990**, *112*, 1546.

(11) Janiak, C. *Angew. Chem., Int. Ed.* **1997**, *36*, 1431.

(12) Rowsell, J. L. C.; Yaghi, O. M. *Microporous Mesoporous Mater.* **2004**, *73*, 3.

(13) Li, H.; Eddaoudi, M.; O'Keeffe, M.; Yaghi, O. M. *Nature* **1999**, *402*, 276.

(14) Chui, S. S. Y.; Lo, S. M. F.; Charmant, J. P. H.; Orpen, A. G.; Williams, I. D. *Science* **1999**, *283*, 1148.

(15) Zou, R. Q.; Abdel-Fattah, A. I.; Xu, H. W.; Zhao, Y. S.; Hickmott, D. D. *CrystEngComm* **2010**, *12*, 1337.

(16) Kitagawa, S.; Kitaura, R.; Noro, S. *Angew. Chem. Int. Ed.* **2004**, *43*, 2334.

(17) Kitaura, R.; Fujimoto, K.; Noro, S.; Kondo, M.; Kitagawa, S. *Angew. Chem. Int. Ed.* **2002**, *41*, 133.

(18) Serre, C.; Millange, F.; Thouvenot, C.; Nogues, M.; Marsolier, G.; Louer, D.; Ferey, G. *J. Am. Chem. Soc.* **2002**, *124*, 13519.

(19) Davis, M. E. *Nature* **2002**, *417*, 813.

(20) Seo, J. S.; Whang, D.; Lee, H.; Jun, S. I.; Oh, J.; Jeon, Y. J.; Kim, K. *Nature* **2000**, *404*, 982.

(21) Janiak, C. *Dalton Trans.* **2003**, 2781.

(22) Robson, R. *Dalton Trans.* **2000**, 3735.

(23) Eddaoudi, M.; Moler, D. B.; Li, H. L.; Chen, B. L.; Reineke, T. M.; O'Keeffe, M.; Yaghi, O. M. *Acc. Chem. Res.* **2001**, *34*, 319.

(24) James, S. L. *Chem. Soc. Rev.* **2003**, *32*, 276.

(25) Ferey, G. *Chem. Soc. Rev.* **2008**, *37*, 191.

(26) Papaefstathiou, G. S.; MacGillivray, L. R. *Coord. Chem. Rev.* **2003**, *246*, 169.

(27) Zaworotko, M. J. *Nature* **2008**, *451*, 410.

(28) Eddaoudi, M.; Kim, J.; Rosi, N.; Vodak, D.; Wachter, J.; O'Keeffe, M.; Yaghi, O. M. *Science* **2002**, *295*, 469.

(29) Furukawa, H.; Ko, N.; Go, Y. B.; Aratani, N.; Choi, S. B.; Choi, E.; Yazaydin, A. O.; Snurr, R. Q.; O'Keeffe, M.; Kim, J.; Yaghi, O. M. *Science* **2010**, *329*, 424.

(30) Fletcher, A. J.; Thomas, K. M.; Rosseinsky, M. J. *J. Solid State Chem.* **2005**, *178*, 2491.

(31) Long, J. R.; Yaghi, O. M. *Chem. Soc. Rev.* **2009**, *38*, 1213.

(32) Qiu, S. L.; Zhu, G. S. *Coord. Chem. Rev.* **2009**, *253*, 2891.

(33) Robson, R. *Dalton Trans.* **2008**, 5113.

(34) O'Keeffe, M.; Peskov, M. A.; Ramsden, S. J.; Yaghi, O. M. *Acc. Chem. Res.* **2008**, *41*, 1782.

(35) Qiu, S. L.; Zhu, G. S.; Fang, Q. R. *From Zeolites to Porous MOF Materials: Proceedings of the 15th International Zeolite Conference*, **2007**.

(36) Eddaoudi, M.; Eubank, J. F.; Liu, Y. L.; Kravtsov, V. C.; Larsen, R. W.; Brant, J. A. *From Zeolites to Porous Mof Materials: Proceedings of the 15th International Zeolite Conference*, **2007**.

(37) Natarajan, S.; Mahata, P. *Chem. Soc. Rev.* **2009**, *38*, 2304.

(38) Tian, Y. Q.; Cai, C. X.; Ji, Y.; You, X. Z.; Peng, S. M.; Lee, G. H. *Angew. Chem. Int. Ed.* **2002**, *41*, 1384.

(39) Tian, Y. Q.; Zhao, Y. M.; Chen, Z. X.; Zhang, G. N.; Weng, L. H.; Zhao, D.-Y. *Chem. Eur. J.* **2007**, *13*, 4146.

(40) Huang, X. C.; Lin, Y. Y.; Zhang, J. P.; Chen, X. M. *Angew. Chem. Int. Ed.* **2006**, *45*, 1557.

(41) Park, K. S.; Ni, Z.; Cote, A. P.; Choi, J. Y.; Huang, R.; Uribe-Romo, F. J.; Chae, H. K.; O'Keeffe, M.; Yaghi, O. M. *Proceedings of the National Academy of Sciences of the United States of America* **2006**, *103*, 10186.

(42) Wu, T.; Bu, X.; Zhang, J.; Feng, P. *Chem. Mater.* **2008**, *20*, 7377.

(43) Liu, Y.; Kravtsov, V. C.; Larsen, R.; Eddaoudi, M. *Chemical Commun.* **2006**, 1488.

(44) Ferey, G.; Serre, C.; Mellot-Draznieks, C.; Millange, F.; Surble, S.; Dutour, J.; Margiolaki, I. *Angew. Chem. Int. Ed.* **2004**, *43*, 6296.

(45) Fang, Q. R.; Zhu, G. S.; Xue, M.; Sun, J. Y.; Wei, Y.; Qiu, S. L.; Xu, R. R. *Angew. Chem. Int. Ed.* **2005**, *44*, 3845.

(46) Rao, C. N. R.; Cheetham, A. K.; Thirumurugan, A. *J. Phys.: Condens. Matter* **2008**, *20*.

(47) Janiak, C.; Vieth, J. K. *New J. Chem.* **2010**, *34*, 2366.

(48) Kurmoo, M. *Chem. Soc. Rev.* **2009**, *38*, 1353.

(49) Kepert, C. J. *Chem. Commun.* **2006**, 695.

(50) Allendorf, M. D.; Bauer, C. A.; Bhakta, R. K.; Houk, R. J. T. *Chem. Soc. Rev.* **2009**, *38*, 1330.

(51) Kondo, M.; Yoshitomi, T.; Seki, K.; Matsuzaka, H.; Kitagawa, S. *Angew. Chem. Int. Ed.* **1997**, *36*, 1725.

(52) Li, H.; Eddaoudi, M.; Groy, T. L.; Yaghi, O. M. *J. Am. Chem. Soc.* **1998**, *120*, 8571.

(53) Eddaoudi, M.; Li, H. L.; Yaghi, O. M. *J. Am. Chem. Soc.* **2000**, *122*, 1391.

(54) Fletcher, A. J.; Cussen, E. J.; Prior, T. J.; Rosseinsky, M. J.; Kepert, C. J.; Thomas, K. M. *J. Am. Chem. Soc.* **2001**, *123*, 10001.

(55) Rosi, N. L.; Eckert, J.; Eddaoudi, M.; Vodak, D. T.; Kim, J.; O'Keeffe, M.; Yaghi, O. M. *Science* **2003**, *300*, 1127.

(56) Wang, X. S.; Ma, S. Q.; Forster, P. M.; Yuan, D. Q.; Eckert, J.; Lopez, J. J.; Murphy, B. J.; Parise, J. B.; Zhou, H. C. *Angew. Chem. Int. Ed.* **2008**, *47*, 7263.

(57) Ma, S. Q.; Sun, D. F.; Simmons, J. M.; Collier, C. D.; Yuan, D. Q.; Zhou, H. C. *J. Am. Chem. Soc.* **2008**, *130*, 1012.

(58) Millward, A. R.; Yaghi, O. M. *J. Am. Chem. Soc.* **2005**, *127*, 17998.

(59) Llewellyn, P. L.; Bourrelly, S.; Serre, C.; Vimont, A.; Daturi, M.; Hamon, L.; De Weireld, G.; Chang, J. S.; Hong, D. Y.; Hwang, Y. K.; Jhung, S. H.; Ferey, G. *Langmuir* **2008**, *24*, 7245.

(60) Wang, Q. M.; Shen, D. M.; Bulow, M.; Lau, M. L.; Deng, S. G.; Fitch, F. R.; Lemcoff, N. O.; Semanscin, J. *Microporous Mesoporous Mater.* **2002**, *55*, 217.

(61) Pan, L.; Adams, K. M.; Hernandez, H. E.; Wang, X. T.; Zheng, C.; Hattori, Y.; Kaneko, K. *J. Am. Chem. Soc.* **2003**, *125*, 3062.

(62) Dybtsev, D. N.; Chun, H.; Yoon, S. H.; Kim, D.; Kim, K. *J. Am. Chem. Soc.* **2004**, *126*, 32.

(63) Chen, B. L.; Ma, S. Q.; Zapata, F.; Fronczek, F. R.; Lobkovsky, E. B.; Zhou, H. C. *Inorg. Chem.* **2007**, *46*, 1233.

(64) Yoon, J. W.; Jhung, S. H.; Hwang, Y. K.; Humphrey, S. M.; Wood, P. T.; Chang, J. S. *Adv. Mater.* **2007**, *19*, 1830.

(65) Zou, Y.; Hong, S.; Park, M.; Chun, H.; Lah, M. S. *Chem. Commun.* **2007**, 5182.

(66) Huang, L. M.; Wang, H. T.; Chen, J. X.; Wang, Z. B.; Sun, J. Y.; Zhao, D. Y.; Yan, Y. S. *Microporous Mesoporous Mater.* **2003**, *58*, 105.

(67) Maji, T. K.; Uemura, K.; Chang, H. C.; Matsuda, R.; Kitagawa, S. *Angew. Chem. Int. Ed.* **2004**, *43*, 3269.

(68) Fletcher, A. J.; Cussen, E. J.; Bradshaw, D.; Rosseinsky, M. J.; Thomas, K. M. *J. Am. Chem. Soc.* **2004**, *126*, 9750.

(69) Takamizawa, S.; Saito, T.; Akatsuka, T.; Nakata, E. *Inorg. Chem.* **2005**, *44*, 1421.

(70) Maji, T. K.; Mostafa, G.; Chang, H. C.; Kitagawa, S. *Chem. Commun.* **2005**, 2436.

(71) Pan, L.; Parker, B.; Huang, X. Y.; Olson, D. H.; Lee, J.; Li, J. *J. Am. Chem. Soc.* **2006**, *128*, 4180.

(72) Lee, J. Y.; Olson, D. H.; Pan, L.; Emge, T. J.; Li, J. *Adv. Funct. Mater.* **2007**, *17*, 1255.

(73) Comotti, A.; Bracco, S.; Sozzani, P.; Horike, S.; Matsuda, R.; Chen, J.; Takata, M.; Kubota, Y.; Kitagawa, S. *J. Am. Chem. Soc.* **2008**, *130*, 13664.

(74) Horike, S.; Tanaka, D.; Nakagawa, K.; Kitagawa, S. *Chem. Commun.* **2007**, 3395.

(75) Zhang, J. P.; Chen, X. M. *J. Am. Chem. Soc.* **2008**, *130*, 6010.

(76) Bourrelly, S.; Moulin, B.; Rivera, A.; Maurin, G.; Devautour-Vino, S.; Serre, C.; Devic, T.; Horcajada, P.; Vimont, A.; Clet, G.; Daturi, M.; Lavalley, J. C.; Loera-Serna, S.; Denoyel, R.; Llewellyn, P. L.; Ferey, G. *J. Am. Chem. Soc.* **2010**, *132*, 9488.

(77) Lin, X.; Blake, A. J.; Wilson, C.; Sun, X. Z.; Champness, N. R.; George, M. W.; Hubberstey, P.; Mokaya, R.; Schroder, M. *J. Am. Chem. Soc.* **2006**, *128*, 10745.

(78) Hou, L.; Lin, Y. Y.; Chen, X. M. *Inorg. Chem.* **2008**, *47*, 1346.

(79) Achmann, S.; Hagen, G.; Kita, J.; Malkowsky, I. M.; Kiener, C.; Moos, R. *Sensors* **2009**, *9*, 1574.

(80) Britt, D.; Tranchemontagne, D.; Yaghi, O. M. *Proc. Natl. Acad. Sci. U. S. A.* **2008**, *105*, 11623.

(81) Luebbers, M. T.; Wu, T. J.; Shen, L. J.; Masel, R. I. *Langmuir* **2010**, *26*, 11319.

(82) Pan, L.; Olson, D. H.; Ciemnolonski, L. R.; Heddy, R.; Li, J. *Angew. Chem. Int. Ed.* **2006**, *45*, 616.

(83) Chen, B. L.; Liang, C. D.; Yang, J.; Contreras, D. S.; Clancy, Y. L.; Lobkovsky, E. B.; Yaghi, O. M.; Dai, S. *Angew. Chem. Int. Ed.* **2006**, *45*, 1390.

(84) Hartmann, M.; Kunz, S.; Himsl, D.; Tangermann, O.; Ernst, S.; Wagener, A. *Langmuir* **2008**, *24*, 8634.

(85) Finsy, V.; Kirschhock, C. E. A.; Vedts, G.; Maes, M.; Alaerts, L.; De Vos, D. E.; Baron, G. V.; Denayer, J. F. M. *Chem. Eur. J.* **2009**, *15*, 7724.

(86) Alaerts, L.; Maes, M.; Giebeler, L.; Jacobs, P. A.; Martens, J. A.; Denayer, J. F. M.; Kirschhock, C. E. A.; De Vos, D. E. *J. Am. Chem. Soc.* **2008**, *130*, 14170.

(87) Cychosz, K. A.; Ahmad, R.; Matzger, A. J. *Chem. Sci.* **2010**, *1*, 293.

(88) Yaghi, O. M.; Li, G. M.; Li, H. L. *Nature* **1995**, *378*, 703.

(89) Yaghi, O. M.; Davis, C. E.; Li, G. M.; Li, H. L. *J. Am. Chem. Soc.* **1997**, *119*, 2861.

(90) Xiong, R. G.; You, X. Z.; Abrahams, B. F.; Xue, Z. L.; Che, C. M. *Angew. Chem. Int. Ed.* **2001**, *40*, 4422.

(91) Suh, M. P.; Min, K. S.; Ko, J. W.; Choi, H. J. *Eur. J. Inorg. Chem.* **2003**, 1373.

(92) Suh, M. P.; Ko, J. W.; Choi, H. J. *J. Am. Chem. Soc.* **2002**, *124*, 10976.

(93) Takamizawa, S.; Kachi-Terajima, C.; Kohbara, M. A.; Akatsuka, T.; Jin, T. *Chem. Asian J.* **2007**, *2*, 837.

(94) Kosal, M. E.; Chou, J. H.; Wilson, S. R.; Suslick, K. S. *Nat. Mater.* **2002**, *1*, 118.

(95) Rather, B.; Zaworotko, M. J. *Chem. Commun.* **2003**, 830.

(96) Gu, J. Z.; Lu, W. G.; Jiang, L.; Zhou, H. C.; Lu, T. B. *Inorg. Chem.* **2007**, *46*, 5835.

(97) Chen, B. L.; Ji, Y. Y.; Xue, M.; Fronczek, F. R.; Hurtado, E. J.; Mondal, J. U.; Liang, C. D.; Dai, S. *Inorg. Chem.* **2008**, *47*, 5543.

(98) Finsy, V.; De Bruyne, S.; Alaerts, L.; De Vos, D.; Jacobs, P. A.; Baron, G. V.; Denayer, J. F. M. *From Zeolites to Porous MOF Materials: Proceedings of the 15th International Zeolite Conference*, **2007**.

(99) Alaerts, L.; Kirschhock, C. E. A.; Maes, M.; van der Veen, M. A.; Finsy, V.; Depla, A.; Martens, J. A.; Baron, G. V.; Jacobs, P. A.; Denayer, J. E. M.; De Vos, D. E. *Angew. Chem. Int. Ed.* **2007**, *46*, 4293.

(100) Chae, H. K.; Siberio-Perez, D. Y.; Kim, J.; Go, Y.; Eddaoudi, M.; Matzger, A. J.; O'Keeffe, M.; Yaghi, O. M. *Nature* **2004**, *427*, 523.

(101) Bai, Y.; He, G. J.; Zhao, Y. G.; Duan, C. Y.; Dang, D. B.; Meng, Q. J. *Chem. Commun.* **2006**, 1530.

(102) Jhung, S. H.; Lee, J. H.; Yoon, J. W.; Serre, C.; Ferey, G.; Chang, J. S. *Adv. Mater.* **2007**, *19*, 121.

(103) Mi, L. W.; Hou, H. W.; Song, Z. Y.; Han, H. Y.; Fan, Y. T. *Chem. Eur. J.* **2008**, *14*, 1814.

(104) Mi, L. W.; Hou, H. W.; Song, Z. Y.; Han, H. Y.; Xu, H.; Fan, Y. T.; Ng, S. W. *Cryst. Growth Des.* **2007**, *7*, 2553.

(105) Wong, K. L.; Law, G. L.; Yang, Y. Y.; Wong, W. T. *Adv. Mater.* **2006**, *18*, 1051.

(106) Horcajada, P.; Serre, C.; Vallet-Regi, M.; Sebban, M.; Taulelle, F.; Ferey, G. *Angew. Chem. Int. Ed.* **2006**, *45*, 5974.

(107) Yaghi, O. M.; Li, H. L. *J. Am. Chem. Soc.* **1995**, *117*, 10401.

(108) Shu, M. H.; Tu, C. L.; Xu, W. D.; Jin, H. B.; Sun, J. *Cryst. Growth Des.* **2006**, *6*, 1890.

(109) Wang, D. X.; He, H. Y.; Chen, X. H.; Feng, S. Y.; Niu, Y. Z.; Sun, D. F. *CrystEngComm* **2010**, *12*, 1041.

(110) Alkordi, M. H.; Liu, Y. L.; Larsen, R. W.; Eubank, J. F.; Eddaoudi, M. *J. Am. Chem. Soc.* **2008**, *130*, 12639.

(111) Dinca, M.; Long, J. R. *J. Am. Chem. Soc.* **2007**, *129*, 11172.

(112) Wang, P.; Ma, J. P.; Dong, Y. B.; Huang, R. Q. *J. Am. Chem. Soc.* **2007**, *129*, 10620.

(113) Chen, S. M.; Zhang, J.; Wu, T.; Feng, P. Y.; Bu, X. H. *J. Am. Chem. Soc.* **2009**, *131*, 16027.

(114) An, J. Y.; Geib, S. J.; Rosi, N. L. *J. Am. Chem. Soc.* **2009**, *131*, 8376.

(115) Plabst, M.; McCusker, L. B.; Bein, T. *J. Am. Chem. Soc.* **2009**, *131*, 18112.

(116) Fujita, M.; Kwon, Y. J.; Washizu, S.; Ogura, K. *J. Am. Chem. Soc.* **1994**, *116*, 1151.

(117) Hwang, Y. K.; Hong, D. Y.; Chang, J. S.; Jhung, S. H.; Seo, Y. K.; Kim, J.; Vimont, A.; Daturi, M.; Serre, C.; Ferey, G. *Angew. Chem. Int. Ed.* **2008**, *47*, 4144.

(118) Schlichte, K.; Kratzke, T.; Kaskel, S. *Microporous Mesoporous Mater.* **2004**, *73*, 81.

(119) Horcajada, P.; Surble, S.; Serre, C.; Hong, D. Y.; Seo, Y. K.; Chang, J. S.; Greneche, J. M.; Margiolaki, I.; Ferey, G. *Chem. Commun.* **2007**, 2820.

(120) Shultz, A. M.; Farha, O. K.; Hupp, J. T.; Nguyen, S. T. *J. Am. Chem. Soc.* **2009**, *131*, 4204.

(121) Suslick, K. S.; Bhyrappa, P.; Chou, J. H.; Kosal, M. E.; Nakagaki, S.; Smithenry, D. W.; Wilson, S. R. *Acc. Chem. Res.* **2005**, *38*, 283.

(122) Ingleson, M. J.; Barrio, J. P.; Guilbaud, J. B.; Khimyak, Y. Z.; Rosseinsky, M. J. *Chem. Commun.* **2008**, 2680.

(123) Ranocchiari, M.; van Bokhoven, J. A. *Phys. Chem. Chem. Phys.* **2011**, *13*, 6388.

(124) Panella, B.; Hirscher, M. *Adv. Mater.* **2005**, *17*, 538.

(125) Burrows, A. D.; Cassar, K.; Friend, R. M. W.; Mahon, M. F.; Rigby, S. P.; Warren, J. E. *CrystEngComm* **2005**, *7*, 548.

(126) Sabo, M.; Henschel, A.; Froede, H.; Klemm, E.; Kaskel, S. *J. Mater. Chem.* **2007**, *17*, 3827.

(127) Kaye, S. S.; Dailly, A.; Yaghi, O. M.; Long, J. R. *J. Am. Chem. Soc.* **2007**, *129*, 14176.

(128) Kusgens, P.; Rose, M.; Senkovska, I.; Frode, H.; Henschel, A.; Siegle, S.; Kaskel, S. *Microporous Mesoporous Mater.* **2009**, *120*, 325.

(129) Low, J. J.; Benin, A. I.; Jakubczak, P.; Abrahamian, J. F.; Faheem, S. A.; Willis, R. R. *J. Am. Chem. Soc.* **2009**, *131*, 15834.

(130) Wu, T. J.; Shen, L. J.; Luebbers, M.; Hu, C. H.; Chen, Q. M.; Ni, Z.; Masel, R. I. *Chem. Commun.* **2010**, *46*, 6120.

(131) Henninger, S. K.; Habib, H. A.; Janiak, C. *J. Am. Chem. Soc.* **2009**, *131*, 2776.

(132) Choi, H. J.; Dinca, M.; Dailly, A.; Long, J. R. *Energy Environ. Sci.* **2010**, *3*, 117.

(133) Demessence, A.; D'Alessandro, D. M.; Foo, M. L.; Long, J. R. *J. Am. Chem. Soc.* **2009**, *131*, 8784.

(134) Tonigold, M.; Lu, Y.; Bredenkotter, B.; Rieger, B.; Bahnmuller, S.; Hitzbleck, J.; Langstein, G.; Volkmer, D. *Angew. Chem. Int. Ed.* **2009**, *48*, 7546.

(135) Cychosz, K. A.; Matzger, A. J. *Langmuir* **2011**, *26*, 17198.

(136) Llewellyn, P. L.; Bourrelly, S.; Serre, C.; Filinchuk, Y.; Ferey, G. *Angew. Chem. Int. Ed.* **2006**, *45*, 7751.

(137) Liu, J.; Wang, Y.; Benin, A. I.; Jakubczak, P.; Willis, R. R.; LeVan, M. D. *Langmuir* **2010**, *26*, 14301.

(138) Loiseau, T.; Serre, C.; Huguenard, C.; Fink, G.; Taulelle, F.; Henry, M.; Bataille, T.; Ferey, G. *Chem.-Eur. J.* **2004**, *10*, 1373.

(139) Kondo, A.; Daimaru, T.; Noguchi, H.; Ohba, T.; Kaneko, K.; Kanoh, H. *J. Colloid Interface Sci.* **2007**, *314*, 422.

(140) Duren, T.; Snurr, R. Q. *J. Phys. Chem. B* **2004**, *108*, 15703.

(141) Jiang, J. W.; Sandler, S. I. *Langmuir* **2006**, *22*, 5702.

(142) Jorge, M.; Lamia, N.; Rodrigues, A. E. *Colloids Surf., A* **2010**, *357*, 27.

(143) Castillo, J. M.; Vlugt, T. J. H.; Calero, S. *J. Phys. Chem. C* **2009**, *113*, 20869.

(144) Greathouse, J. A.; Ockwig, N. W.; Criscenti, L. J.; Guilinger, T. R.; Pohl, P.; Allendorf, M. D. *Phys. Chem. Chem. Phys.* **2010**, *12*, 12621.

(145) Babarao, R.; Jiang, J. W. *J. Phys. Chem. C* **2009**, *113*, 18287.

(146) Bao, X. Y.; Broadbelt, L. J.; Snurr, R. Q. *Mol. Simul.* **2009**, *35*, 50.

(147) Greathouse, J. A.; Allendorf, M. D. *J. Am. Chem. Soc.* **2006**, *128*, 10678.

(148) Schrock, K.; Schroder, F.; Heyden, M.; Fischer, R. A.; Havenith, M. *Phys. Chem. Chem. Phys.* **2008**, *10*, 4732.

(149) Han, S. S.; Choi, S. H.; van Duin, A. C. T. *Chem. Commun.* **2010**, *46*, 5713.

(150) Chen, Y. F.; Babarao, R.; Sandler, S. I.; Jiang, J. W. *Langmuir* **2010**, *26*, 8743.

(151) Yazaydin, A. O.; Benin, A. I.; Faheem, S. A.; Jakubczak, P.; Low, J. J.; Willis, R. R.; Snurr, R. Q. *Chem. Mater.* **2009**, *21*, 1425.

(152) Castillo, J. M.; Vlugt, T. J. H.; Calero, S. *J. Phys. Chem. C* **2008**, *112*, 15934.

(153) Paranthaman, S.; Coudert, F. X.; Fuchs, A. H. *Phys. Chem. Chem. Phys.* **2010**, *12*, 8123.

(154) Krishna, R.; van Baten, J. M. *Langmuir* **2010**, *26*, 10854.

(155) Babarao, R.; Jiang, J. W. *Energy Environ. Sci.* **2009**, *2*, 1088.

(156) Jiang, J. W. *AIChE J.* **2009**, *55*, 2422.

(157) Chen, Y. F.; Lee, J. Y.; Babarao, R.; Li, J.; Jiang, J. W. *J. Phys. Chem. C* **2010**, *114*, 6602.

(158) Xiong, R. C.; Fern, J. T.; Keffer, D. J.; Fuentes-Cabrera, M.; Nicholson, D. M. *Mol. Simul.* **2009**, *35*, 910.

(159) Hu, Z. Q. H. Z. Q.; Chen, Y. F.; Jiang, J. W. *J. Chem. Phys.* **2011**, *134*.

(160) Frenkel, D.; Smit, B. *Understanding Molecular Simulations: From algorithms to applications*; Academic Press,San Diego, **2002**.

(161) Allen, M. P.; Tildesley, D. J. *Computer Simulation of Liquids*; Oxford University Press, Oxford, **1987**.

(162) Cornell, W. D.; Cieplak, P.; Bayly, C. I.; Gould, I. R.; Merz, K. M.; Ferguson, D. M.; Spellmeyer, D. C.; Fox, T.; Caldwell, J. W.; Kollman, P. A. *J. Am. Chem. Soc.* **1995**, *117*, 5179.

(163) MacKerell, A. D.; Bashford, D.; Bellott, M.; Dunbrack, R. L.; Evanseck, J. D.; Field, M. J.; Fischer, S.; Gao, J.; Guo, H.; Ha, S.; Joseph-McCarthy, D.; Kuchnir, L.; Kuczera, K.; Lau, F. T. K.; Mattos, C.; Michnick, S.; Ngo, T.; Nguyen, D. T.; Prodhom, B.; Reiher, W. E.; Roux, B.; Schlenkrich, M.; Smith, J. C.; Stote, R.; Straub, J.; Watanabe, M.; Wiorkiewicz-Kuczera, J.; Yin, D.; Karplus, M. *J. Phys. Chem. B* **1998**, *102*, 3586.

(164) Schuler, L. D.; Daura, X.; Van Gunsteren, W. F. *J. Comput. Chem.* **2001**, *22*, 1205.

(165) Dauberosguthorpe, P.; Roberts, V. A.; Osguthorpe, D. J.; Wolff, J.; Genest, M.; Hagler, A. T. *Proteins: Struct. Funct. Genet.* **1988**, *4*, 31.

(166) Allinger, N. L.; Yuh, Y. H.; Lii, J. H. *J. Am. Chem. Soc.* **1989**, *111*, 8551.

(167) Rappe, A. K.; Casewit, C. J.; Colwell, K. S.; Goddard III, W. A.; Skiff, W. M. *J. Am. Chem. Soc.* **1992**, *114*, 10024.

(168) Vlugt, T. J. H.; van der Eerden, J. P. J. M.; Dijkstra, M.; Smit, B.; Frenkel, D. *Introduction to Molecular Simulation and Statistical Thermodynamics*; http;//www.phys.uu.nl/~vlugt/imsst, **2008**.

(169) Metropolis, N.; Rosenbluth, A. W.; Rosenbluth, M. N.; Teller, A. H.; Teller, E. *J. Chem. Phys.* **1953**, *21*, 1087.

(170) Bagchi, B. *Chem. Rev.* **2005**, *105*, 3197.

(171) Ball, P. *ChemPhysChem* **2008**, *9*, 2677.

(172) Janiak, C.; Scharmann, T. G.; Mason, S. A. *J. Am. Chem. Soc.* **2002**, *124*, 14010.

(173) Liu, Q.-Y.; Xu, L. *CrystEngComm* **2005**, *7*, 87.

(174) Naskar, J. P.; Drew, M. G. B.; Hulme, A.; Tocher, D. A.; Datta, D. *CrystEngComm* **2005**, *7*, 67.

(175) Mir, M. H.; Wang, L.; Wong, M. W.; Vittal, J. J. *Chem. Commun.* **2009**, 4539.

(176) Radhakrishnan, R.; Gubbins, K. E.; Sliwinska-Bartkowiak, M. *J. Chem. Phys.* **2002**, *116*, 1147.

(177) Sliwinska-Bartkowiak, M.; Jazdzewska, M.; Huang, L. L.; Gubbins, K. E. *Phys. Chem. Chem. Phys.* **2008**, *10*, 4909.

(178) Liu, H.; Murad, S.; Jameson, C. J. *J. Chem. Phys.* **2006**, *125*.

(179) Banerjee, S.; Murad, S.; Puri, I. K. *Chem. Phys. Lett.* **2007**, *434*, 292.

(180) Do, D. D.; Junpirom, S.; Do, H. D. *Carbon* **2009**, *47*, 1466.

(181) Wongkoblap, A.; Do, D. D. *J. Phys. Chem. B* **2007**, *111*, 13949.

(182) Zang, J.; Konduri, S.; Nair, S.; Sholl, D. S. *ACS Nano* **2009**, *3*, 1548.

(183) Beauvais, C.; Boutin, A.; Fuchs, A. H. *ChemPhysChem* **2004**, *5*, 1791.

(184) Di Lella, A.; Desbiens, N.; Boutin, A.; Demachy, I.; Ungerer, P.; Bellat, J.-P.; Fuchs, A. H. *Phys. Chem. Chem. Phys.* **2006**, *8*, 5396.

(185) Demontis, P.; Gulin-Gonzalez, J.; Jobic, H.; Masia, M.; Sale, R.; Suffritti, G. B. *ACS Nano* **2008**, *2*, 1603.

(186) Nalaparaju, A.; Zhao, X. S.; Jiang, J. *J. Phys. Chem. C* **2008**, *112*, 12861.

(187) Hu, Z.; Jiang, J. *Langmuir* **2008**, *24*, 4215.

(188) Hu, Z.; Jiang, J. *Biophys. J.* **2008**, *95*, 4148.

(189) Mueller, U.; Schubert, M.; Teich, F.; Puetter, H.; Schierle-Arndt, K.; Pastre, J. *J. Mater. Chem.* **2006**, *16*, 626.

(190) Kitagawa, S.; Matsuda, R. *Coord. Chem. Rev.* **2007**, *251*, 2490.

(191) Castillo, J. M.; Vlugt, T. J. H.; Calero, S. *J. Phys. Chem. C* **2008**, *112*, 15934.

(192) Sava, D. F.; Kravtsov, V. C.; Nouar, F.; Wojtas, L.; Eubank, J. F.; Eddaoudi, M. *J. Am. Chem. Soc.* **2008**, *130*, 3768.

(193) Nouar, F.; Eckert, J.; Eubank, J. F.; Forster, P.; Eddaoudi, M. *J. Am. Chem. Soc.* **2009**, *131*, 2864.

(194) Wu, Y.; Tepper, H. L.; Voth, G. A. *J. Chem. Phys.* **2006**, *124*, 1.

(195) Frisch, M. J. *Gaussian 03* **2003**.

(196) Smith, W.; Forester, T. R. *J. Mol. Graph.* **1996**, *14*, 136.

(197) Babarao, R.; Jiang, J. *J. Am. Chem. Soc.* **2009**, *131*, 11417.

(198) Lee, Y.; Reisner, B. A.; Hanson, J. C.; Jones, G. A.; Parise, J. B.; Corbin, D. R.; Toby, B. H.; Freitag, A.; Larese, J. Z. *J. Phys. Chem. B* **2001**, *105*, 7188.

(199) Shirono, K.; Endo, A.; Daiguji, H. *J. Phys. Chem. B* **2005**, *109*, 3446.

(200) Koneshan, S.; Rasaiah, J. C. *J. Chem. Phys.* **2000**, *113*, 8125.

(201) Dzhigit, O. M.; Kiselev, A. V.; Mikos, K. N.; Muttik, G. G.; Rahmanova, T. A. *Transactions of the Faraday Society* **1971**, *67*, 458.

(202) Bolis, V.; Busco, C.; Ugliengo, P. *J. Phys. Chem. B* **2006**, *110*, 14849.

(203) Plant, D. F.; Maurin, G.; Deroche, I.; Gaberova, L.; Llewellyn, P. L. *Chem. Phys. Lett.* **2006**, *426*, 387.

(204) Dang, L. X.; Pettitt, B. M. *J. Phys. Chem.* **1987**, *91*, 3349.

(205) Leherte, L.; Andre, J.-M.; Derouane, E. G.; Vercauteren, D. P. *Int. J. Quantum Chem.* **1992**, *42*, 1291.

(206) Praprotnik, M.; Janezic, D.; Mavri, J. *J. Phys. Chem. A* **2004**, *108*, 11056.

(207) Sonoda, M. T.; Moreira, N. H.; Martinez, L.; Favero, F. W.; Vechi, S. M.; Martins, L. R.; Skaf, M. S. *Braz. J. Phys.* **2004**, *34*, 3.

(208) Crupi, V.; Longo, F.; Majolino, D.; Venuti, V. *J. Phys.: Condens. Matter* **2006**, *18*, 3563.

(209) Garberoglio, G.; Skoulidas, A. I.; Johnson, J. K. *J. Phys. Chem. B* **2005**, *109*, 13094.

(210) Skoulidas, A. I.; Sholl, D. S. *J. Phys. Chem. B* **2005**, *109*, 15760.

(211) Frost, H.; Duren, T.; Snurr, R. Q. *J. Phys. Chem. B* **2006**, *110*, 9565.

(212) Yang, Q.; Zhong, C. *J. Phys. Chem. B* **2006**, *110*, 17776.

(213) Martin-Calvo, A.; Garcia-Perez, E.; Manuel Castillo, J.; Calero, S. *Phys. Chem. Chem. Phys.* **2008**, *10*, 7085.

(214) Keskin, S.; Sholl, D. S. *Ind. Eng. Chem. Res.* **2009**, *48*, 914.

(215) Keskin, S.; Liu, J.; Johnson, J. K.; Sholl, D. S. *Microporous Mesoporous Mater.* **2009**, *125*, 101.

(216) Bae, Y.-S.; Farha, O. K.; Spokoyny, A. M.; Mirkin, C. A.; Hupp, J. T.; Snurr, R. Q. *Chem. Commun.* **2008**, 4135.

(217) Chen, B.; Ji, Y.; Xue, M.; Fronczek, F. R.; Hurtado, E. J.; Mondal, J. U.; Liang, C.; Dai, S. *Inorg. Chem.* **2008**, *47*, 5543.

(218) Liu, Y. L.; Kravtsov, V. C.; Larsen, R.; Eddaoudi, M. *Chem. Commun.* **2006**, *14*, 1488.

(219) Park, K. S.; Ni, Z.; Cote, A. P.; Choi, J. Y.; Huang, R. D.; Uribe-Romo, F. J.; Chae, H. K.; O'Keeffe, M.; Yaghi, O. M. *Proc. Natl. Acad. Sci. U. S. A.* **2006**, *103*, 10186.

(220) Banerjee, R.; Phan, A.; Wang, B.; Knobler, C.; Furukawa, H.; O'Keeffe, M.; Yaghi, O. M. *Science* **2008**, *319*, 939.

(221) Wang, B.; Cote, A. P.; Furukawa, H.; O'Keeffe, M.; Yaghi, O. M. *Nature* **2008**, *453*, 207.

(222) Liu, D.; Zheng, C.; Yang, Q.; Zhong, C. *J. Phys. Chem. C* **2009**, *113*, 5004.

(223) Liu, Y.; Liu, H.; Hu, Y.; Jiang, J. *J. Phys. Chem. B* **2009**, *113*, 12326.

(224) Rankin, R. B.; Liu, J.; Kulkarni, A. D.; Johnson, J. K. *J. Phys. Chem. C* **2009**, *113*, 16906.

(225) Li, K.; Olson, D. H.; Seidel, J.; Emge, T. J.; Gong, H.; Zeng, H.; Li, J. *J. Am. Chem. Soc.* **2009**, *131*, 10368.

(226) Smart, O. S.; Neduvelil, J. G.; Wang, X.; Wallace, B. A.; Sansom, M. S. P. *J. Mol. Graph.* **1996**, *14*, 354.

(227) Nalaparaju, A.; Babarao, R.; Zhao, X. S.; Jiang, J. W. *ACS Nano* **2009**, *3*, 2563.

(228) Singh, U. C.; Kollman, P. A. *J. Comput. Chem.* **1984**, *5*, 129.

(229) Besler, B. H.; Merz K.M., J.; Kollman, P. A. *J. Comput. Chem.* **1990**, *11*, 431.

(230) Babarao, R.; Hu, Z.; Jiang, J.; Chempath, S.; Sandler, S. I. *Langmuir* **2007**, *23*, 659.

(231) Babarao, R.; Jiang, J. *Langmuir* **2008**, *24*, 6270.

(232) Chen, B.; Potoff, J. J.; Siepmann, J. I. *J. Phys. Chem. B* **2001**, *105*, 3093.

(233) Linstrom, P. J.; Mallard, W. G. *NIST Chemistry WebBook* **2001**.

(234) Abrams, L.; Corbin, D. R. *J. Catal.* **1991**, *127*, 9.

(235) Kristof, T.; Csanyi, E.; Rutkai, G.; Merenyi, L. *Mol. Simul.* **2006**, *32*, 869.

(236) Okamoto, K.-I.; Kita, H.; Horii, K.; Tanaka, K.; Kondo, M. *Ind. Eng. Chem. Res.* **2001**, *40*, 163.

(237) Csanyi, E.; Kristof, T.; Lendvay, G. *J. Phys. Chem. C* **2009**, *113*, 12225.

(238) Furukawa, S.-I.; Goda, K.; Zhang, Y.; Nitta, T. *J. Chem. Eng. Jpn.* **2004**, *37*, 67.

(239) Wu, H.; Zhou, W.; Yildirim, T. *J. Am. Chem. Soc.* **2007**, *129*, 5314.

(240) Fleys, M.; Thompson, R. W. *J. Chem. Theory Comput.* **2005**, *1*, 453.

(241) Cailliez, F.; Stirnemann, G.; Boutin, A.; Demachy, I.; Fuchs, A. H. *J. Phys. Chem. C* **2008**, *112*, 10435.

(242) Shevade, A. V.; Jiang, S.; Gubbins, K. E. *Mol. Phys.* **1999**, *97*, 1139.

(243) Shevade, A. V.; Jiang, S.; Gubbins, K. E. *J. Chem. Phys.* **2000**, *113*, 6933.

(244) Hill, J.; Nelson, E.; Tilman, D.; Polasky, S.; Tiffany, D. *Proc. Natl. Acad. Sci. U. S. A.* **2006**, *103*, 11206.

(245) Luque, R.; Herrero-Davila, L.; Campelo, J. M.; Clark, J. H.; Hidalgo, J. M.; Luna, D.; Marinas, J. M.; Romero, A. A. *Energy Environ. Sci.* **2008**, *1*, 542.

(246) Frolkova, A. K.; Raeva, V. M. *Theor. Found. Chem. Eng.* **2010**, *44*, 545.

(247) Lipnizki, F. *Desalination* **2010**, *250*, 1067.

(248) Qu, X. Y.; Dong, H.; Zhou, Z. J.; Zhang, L.; Chen, H. L. *Ind. Eng. Chem. Res.* **2010**, *49*, 7504.

(249) Li, J. R.; Kuppler, R. J.; Zhou, H. C. *Chem. Soc. Rev.* **2009**, *38*, 1477.

(250) Duren, T.; Bae, Y.-S.; Snurr, R. Q. *Chem. Soc. Rev.* **2009**, *38*, 1237.

(251) Keskin, S.; Liu, J.; Rankin, R. B.; Johnson, J. K.; Sholl, D. S. *Ind. Eng. Chem. Res.* **2009**, *48*, 2355.

(252) Ahmad, R.; Wong-Foy, A. G.; Matzger, A. J. *Langmuir* **2009**, *25*, 11977.

(253) Alaerts, L.; Kirschhock, C. E. A.; Maes, M.; Van Der Veen, M. A.; Finsy, V.; Depla, A.; Martens, J. A.; Baron, G. V.; Jacobs, P. A.; Denayer, J. F. M.; De Vos, D. E. *Angew. Chem. Int. Ed.* **2007**, *46*, 4293.

(254) Nalaparaju, A.; Zhao, X. S.; Jiang, J. W. *J. Phys. Chem. C* **2010**, *114*, 11542.

(255) Kurihara, K.; Nakamichi, M.; Kojima, K. *J. Chem. Eng. Data* **1993**, *38*, 446.

(256) Van Der Spoel, D.; Lindahl, E.; Hess, B.; Groenhof, G.; Mark, A. E.; Berendsen, H. J. C. *J. Comput. Chem.* **2005**, *26*, 1701.

(257) Hess, B.; Bekker, H.; Berendsen, H. J. C.; Fraaije, J. G. E. M. *J. Comput. Chem.* **1997**, *18*, 1463.

(258) Lu, L.; Shao, Q.; Huang, L.; Lu, X. *Fluid Phase Equilib.* **2007**, *261*, 191.

(259) Krishna, R.; Van Baten, J. M. *J. Phys. Chem. C* **2010**, *114*, 13154.

(260) Wu, J. Y.; Liu, Q. L.; Xiong, Y.; Zhu, A. M.; Chen, Y. *J. Phys. Chem. B* **2009**, *113*, 4267.

(261) Sano, T.; Yanagishita, H.; Kiyozumi, Y.; Mizukami, F.; Haraya, K. *J. Membr. Sci.* **1994**, *95*, 221.

(262) Zhang, C.; Yang, X. *Fluid Phase Equilib.* **2005**, *231*, 1.

(263) Ahn, H.; Lee, H.; Lee, S.-B.; Lee, Y. *Desalination* **2006**, *193*, 244.

(264) Yang, J. Z.; Liu, Q. L.; Wang, H. T. *Fluid Phase Equilib.* **2007**, *291*, 1.

(265) Keskin, S.; Sholl, D. S. *Langmuir* **2009**, *25*, 11786.

(266) Krishna, R.; van Baten, J. M. *Chem. Eng. J.* **2007**, *133*, 121.

(267) Babarao, R.; Jiang, J. *Langmuir* **2008**, *24*, 5474.

(268) Sun, Y.-M.; Huang, T.-L. *J. Polym. Res.* **1995**, *2*, 47.

(269) Molina, J. M.; Vatai, G.; Bekassy-Molnar, E. *Desalination* **2002**, *149*, 89.

(270) Shannon, M. A.; Bohn, P. W.; Elimelech, M.; Georgiadis, J. G.; Marinas, B. J.; Mayes, A. M. *Nature* **2008**, *452*, 301.

(271) Patrick, L. *Alternat. Med. Rev.* **2006**, *11*, 2.

(272) Fu, F. L.; Wang, Q. *J. Environ. Manag.* **2011**, *92*, 407.

(273) Zagorodni, A. A. *Ion Exchange Materials Properties and Applications*; Elsevier, Netherlands, **2007**.

(274) Clearfield, A. *Nature Chem.* **2010**, *2*, 161.

(275) Colella, C. *Miner. Deposita* **1996**, *31*, 554.

(276) Liu, D. H.; Zhong, C. L. *J. Mater. Chem.* **2010**, *20*, 10308.

(277) Custelcean, R.; Sellin, V.; Moyer, B. A. *Chem. Commun.* **2007**, 1541.

(278) Fang, Q. R.; Zhu, G. S.; Xue, M.; Wang, Z. P.; Sun, J. Y.; Qiu, S. L. *Cryst. Growth Des.* **2008**, *8*, 319.

(279) Lu, W. G.; Jiang, L.; Feng, X. L.; Lu, T. B. *Inorg. Chem.* **2009**, *48*, 6997.

(280) Fei, H. H.; Rogow, D. L.; Oliver, S. R. J. *J. Am. Chem. Soc.* **2010**, *132*, 7202.

(281) Allen, T. W.; Andersen, O. S.; Roux, B. *Biophys. Chem.* **2006**, *124*, 251.

(282) Rotenberg, B.; Marry, V.; Vuilleumier, R.; Malikova, N.; Simon, C.; Turq, P. *Geochim. Cosmochim. Acta* **2007**, *71*, 5089.

(283) Torrie, G. M.; Valleau, J. P. *J. Comput. Phys.* **1977**, *23*, 187.

(284) Kumar, S.; Bouzida, D.; Swendsen, R. H.; Kollman, P. A.; Rosenberg, J. M. *J. Comput. Chem.* **1992**, *13*, 1011.

(285) Jardat, M.; Dufreche, J. F.; Marry, V.; Rotenberg, B.; Turq, P. *Phys. Chem. Chem. Phys.* **2009**, *11*, 2023.

Publications

Nalaparaju, A., Jiang, JW. Ion Exchange in *rho* Zeolite-like Metal-Organic Framework for Water Purification: A Molecular Dynamics Simulation Study, *Journal of Physical Chemistry C*, **2012**, 116, 6925-6931.

Nalaparaju, A., Zhao, XS., Jiang, JW. Biofuel Purification by Pervaporation and Vapor Permeation in Metal-Organic Frameworks: A Computational Study, *Energy and Environmental Science*, **2011**, 4, 2107-2116.

Nalaparaju, A., Zhao, XS., Jiang, JW. Molecular Understanding for the Adsorption of Water and Alcohols in Hydrophilic and Hydrophobic Zeolitic Metal-Organic Frameworks, *Journal of Physical Chemistry C*, **2010**, 114, 11542-11550.

Nalaparaju, A., Babarao, R., Zhao, XS., Jiang, JW. Atomistic Insight into Adsorption, Mobility, and Vibration of Water in Ion-Exchanged Zeolite-like Metal-Organic Frameworks, *ACS Nano*, **2009**, 9, 263-2572.

Nalaparaju, A., Hu, ZQ., Zhao, XS., Jiang, JW. Exchange of Heavy Metal Ions in Titanosilicate Na-ETS-10 Membrane from Molecular Dynamics Simulations, *Journal of Membrane Science*, **2009**, 335, 89-95.

Nalaparaju, A., Zhao, XS., Jiang, JW. Molecular Interplay of Cations and Nonpolar/Polar Sorbates in Titanosilicate ETS-10, *Journal of Physical Chemistry C*, **2008**, 112, 12861-12868.

Presentations

Zeolite-like Metal-Organic Framework for Water Purification through Ion Exchange: A Molecular Dynamics Simulation Study, Nalaparaju, A., Jiang, JW. *14th Asia Pacific Confederation of Chemical Engineering (APCCHE)*, February 21-24, **2012**, Singapore.

Molecular Insight into Adsorption and Dynamics of Water in Zeolite-like Metal-Organic Frameworks, Nalaparaju, A., Jiang, JW. *International Conference on Materials for Advanced Technologies (ICMAT)*, June 26-1 July, **2011**, Singapore.

Biofuel Purification in Hydrophilic and Hydrophobic Metal-Organic Framework Membranes: A Computational Study, Nalaparaju, A., Jiang, JW. *International Conference on Materials for Advanced Technologies (ICMAT)*, June 26-1 July, **2011**, Singapore.

Exploring the Adsorption and Dynamics of Water in Zeolite-like Metal-Organic Frameworks Using Atomistic Simulations, Nalaparaju, A., Babarao, R., Zhao, XS., Jiang, JW. *AICHE Annual Meeting*, November 8-13, **2009**, Nashville, USA.

Mechanistic Understanding of Selective Interaction of Divalent Ions with Titanosilicate ETS-10, Nalaparaju, A., Zhao, XS., Jiang, JW. *AICHE Annual Meeting*, November 8-13, **2009**, Nashville, USA.

Characterization of Extraframework Ions and Interplay with Nonpolar/Polar Sorbates in Titanosilicate ETS-10: A Molecular Simulation Study, Nalaparaju, A., Zhao, XS., Jiang, JW. *5th Pacific Basin Conference on Adsorption Science and Technology (PBAST)*, May 25-27, **2009**, Singapore.

Cation Redistribution Upon Water Adsorption in Titanosilicate ETS-10, Nalaparaju, A., Zhao, XS., Jiang, JW. *7th WSEAS Int. Conf. on Applied Computer and Applied Computational Science*, April 6-8, **2008**, Hangzhou, China.

Appendix

From: CONTRACTS-COPYRIGHT (shared) [Contracts-Copyright@rsc.org]
Sent: Friday, April 27, 2012 8:55 PM
To: Anjaiah Nalaparaju
Subject: RE: Permission Request Form: Nalaparaju Anjaiah

Dear Nalaparaju

The Royal Society of Chemistry hereby grants permission for the use of the material specified below in the work described and in all subsequent editions of the work for distribution throughout the world, in all media including electronic and microfilm. You may use the material in conjunction with computer-based electronic and information retrieval systems, grant permissions for photocopying, reproductions and reprints, translate the material and to publish the translation, and authorize document delivery and abstracting and indexing services. The Royal Society of Chemistry is a signatory to the STM Guidelines on Permissions (available on request).

Please note that if the material specified below or any part of it appears with credit or acknowledgement to a third party then you must also secure permission from that third party before reproducing that material.

For the figure from *CrystEngComm*, please ensure that the published article carries a credit to The Royal Society of Chemistry in the following format:

[Original citation] – Reproduced by permission of The Royal Society of Chemistry

For the figure from NJC, please ensure that the published article carries a credit to The Royal Society of Chemistry in the following format:

[Original citation] – Reproduced by permission of The Royal Society of Chemistry (RSC) for the Centre National de la Recherche Scientifique (CNRS) and the RSC

Please also ensure that any electronic version of the work includes a hyperlink to the article on the Royal Society of Chemistry website. The recommended form for the hyperlink is http://dx.doi.org/10.1039/*DOI suffix*, for example in the link http://dx.doi.org/10.1039/b110420a the DOI suffix is 'b110420a'. To find the relevant DOI suffix for the RSC paper in question, go to the Journals section of the website and locate your paper in the list of papers for the volume and issue of your specific journal. You will find the DOI suffix quoted there.

The RSC is now using RightsLink to process its permission requests from journal articles and RightsLink should be used for all future requests to reproduce material from RSC journals (except *Chemistry World* and *Education in Chemistry*). Please visit http://www.rsc.org/AboutUs/Copyright/Permissionrequests.asp for more detail. If you are reproducing the material in a publication published by an STM Publisher please specify STM Publisher after "I am a…".

Regards

Gill Cockhead
Publishing Contracts & Copyright Executive

Gill Cockhead (Mrs), Publishing Contracts & Copyright Executive
Royal Society of Chemistry, Thomas Graham House
Science Park, Milton Road, Cambridge CB4 0WF, UK
Tel +44 (0) 1223 432134, Fax +44 (0) 1223 423623
http://www.rsc.org

-----Original Message-----
From: g0600030@nus.edu.sg [mailto:g0600030@nus.edu.sg]
Sent: 27 April 2012 12:50
To: CONTRACTS-COPYRIGHT (shared)
Subject: Permission Request Form: Nalaparaju Anjaiah

Name : Nalaparaju Anjaiah
Address :

National University of Singapore
Department of Chemical & Biomolecular Engineering
4 Engineering Drive 4, Blk E5 #02-09
Singapore 117576

Tel : 65-61561946
Fax :
Email : g0600030@nus.edu.sg

I am preparing the following work for publication:

Article/Chapter Title : Molecular Simulations of Biofuel and Water Purification in Metal-Organic Frameworks
Journal/Book Title :
Editor/Author(s) : Anjaiah Nalaparaju
Publisher : National University of Songapore

I would very much appreciate your permission to use the following material:

Journal/Book Title : CrystEngComm
Editor/Author(s) : Ruqiang Zou et al.
Volume Number : 12
Year of Publication : 2010
Description of Material : Figure 4
Page(s) : 1340
Journal/Book Title : New Journal of Chemistry
Editor/Author(s) : Christoph Janiak
Volume Number : 34
Year of Publication : 2010
Description of Material : Figure 1
Page(s) : 2366

Any Additional Comments :

Dear Publishing officer,

I would like to request for the permissions to use the above specified material in my thesis. I will be thankful to your consideration.